



TECHNISCHE
UNIVERSITÄT
WIEN

DISSERTATION

Fracture toughness of hard coatings

carried out for the purpose of obtaining the degree of Doctor technicae (Dr. techn.),
submitted at TU Wien, Faculty of Mechanical and Industrial Engineering,

by

Dipl.-Ing. Rainer Hahn



under the supervision of

Univ. Prof. Dipl.-Ing. Dr. mont. Paul Heinz Mayrhofer

Univ. Ass. Dipl.-Ing. Dr. mont. Matthias Bartosik

Institute of Materials Science and Technology, E308

Materials Science Division

Vienna, June 2019

Reviewed by

.....
Daniel Kiener
Department Werkstoffwissenschaft
Montanuniversität Leoben
Jahnstraße 12, 8700 Leoben

.....
Christoph Eisenmenger-Sittner
Institut für Festkörperphysik
TU Wien
Wiedner Hauptstraße 8-10, 1040 Wien

This work was supported by Plansee Composite Materials GmbH and Oerlikon Balzers, Oerlikon Surface Solutions AG in the framework of the Christian Doppler Laboratory for Application Oriented Coating Development.

I confirm, that going to press of this thesis needs the confirmation of the examination committee.

Affidavit:

I declare in lieu of oath, that I wrote this thesis and performed the associated research myself, using only literature cited in this volume. If text passages from sources are used literally, they are marked as such.

I confirm that this work is original and has not been submitted elsewhere for any examination, nor is it currently under consideration for a thesis elsewhere.

Date

Signature

”[...] der unermesslich reichen, stets sich erneuernden Natur gegenüber wird der Mensch, so weit er auch in der wissenschaftlichen Erkenntnis fortgeschritten sein mag, immer das sich wundernde Kind bleiben und muss sich stets auf neue Überraschungen gefasst machen.”

– Max Planck (1858-1947)

Acknowledgements

First of all, I want to thank **Prof. Paul Heinz Mayrhofer** for providing the opportunity to work on my thesis within the framework of the Christian Doppler Laboratory for Application Oriented Coating Development and the Institute of Materials Science and Technology. As my supervisor he provided me support, taught me to critically evaluate derived results, and to present them in the best possible way. He not only guided me through the last three years as PhD student, but since I started to work in his group as research assistant in May 2012.

Furthermore, I am very grateful to my thesis advisor **Dr. Matthias Bartosik**. Thank you for the great support during the thesis, and fruitful, detailed discussions on superlattice coatings and their characteristics. Also, for teaching and introducing me to conventional x-ray diffraction, and nanodiffraction methods at Deutsches Elektronen-Synchrotron (DESY). Thank you Matthias.

I also want to give a special thank you to **Dr. Helmut Riedl**, who provided support and assistance during my thesis, guiding me through the field of physical vapor deposition and helping me to gain a deeper insight.

I am grateful to the **whole TU Wien thin film group and its former members** for such a great time during the past 3 years. I really enjoy working here. In particular, I would like to mention my former bachelor and now master student **Arnold Tymoszuk**, my former bachelor student **Oruç Süleyman Fıçıcı**, **Lukas Zauner** for assistance with LaTeX, and my colleague **Alexander Kirnbauer** with whom I shared the office.

A special thank you is dedicated to **my family**, for your support not only during my studies in Leoben and Vienna, but also during my whole life. For listening to my problems and providing a place of recreation. I would like to dedicate my biggest gratitude to my wife **Sabine** for encouraging and supporting me to work towards this thesis, and our son **Elias**, your smile brightens my day.

Contents

Contents	v
Abstract	1
Kurzfassung	3
1 Introduction	5
1.1 Fracture Toughness	6
1.2 Ti-B-N Model System	8
2 Thin Film Deposition	10
2.1 Physical Vapor Deposition	10
2.1.1 Cathodic Arc Evaporation	10
2.1.2 Magnetron Sputtering	12
2.2 Film Nucleation and Growth	16
2.2.1 Nucleation	16
2.2.2 Film Growth	16
2.3 Experimental	20
2.3.1 Fracture Toughness Testing	21
2.3.2 Single Cantilever Bending Test	23
3 Mechanical Properties	25
3.1 Strengthening Mechanisms	25

3.1.1	Solid Solution Strengthening	25
3.1.2	Grain Refinement Strengthening	27
3.1.3	Cold Work Strengthening	29
3.1.4	Precipitation Strengthening	30
3.2	Fracture Toughness Enhancement	30
3.2.1	Fracture Properties of the Ti-B-N System	32
3.2.2	Other Mechanisms Increasing the Fracture Toughness	35
Bibliography		36
4	Contributions to the field	41
4.1	First Author Publications	41
4.2	Thesis-Related Co-Author Publications	44
4.3	Further Publications	45
4.4	Supervision	46
4.5	International Conference Contributions	46
4.6	PhD Related Awards	47
5	Publications	48
Publication I		49
Publication II		54
Publication III		60
Publication IV		64
Publication V		73
Publication VI		90
Publication VII		100

Publication VIII	106
Publication IX	113
6 Concluding remarks	131

Abstract

Ceramic hard coatings deposited by physical vapor deposition (PVD), *i.e.* transition metal nitrides, carbides, and borides, are successfully used as protective coatings in the cutting industry and on forming tools. Thereby they prolong the lifetime of tools and cutting inserts by up to some 100%. Their advantageous properties like high hardness, chemical stability, thermal stability, and oxidation resistance provide the basis for operating in harsh environments. However, major drawbacks of these materials are their inherent brittleness stemming from their lack of ductility, and their low fracture toughness K_{IC} . This material property is technologically relevant, a failure of the coating leads to immediate oxidation and mechanical load of the substrate and thus to premature failure, especially in applications where wear is dominated by mechanical loads. Due to the constant endeavor in industrial processes for increased throughput without compromising restrictions in reliability, the search for new material systems as well as the effort to understand basic mechanisms leading to enhanced properties is consistently high.

In this PhD thesis, mechanisms overcoming this unfavorable behavior are investigated and characterized. *In-situ* micromechanical cantilever bending tests, used to obtain fracture toughness values, provide the basis for these studies. Thereby cantilevers, typically in the size of some μm , are machined using a focused ion beam (FIB) work station. Here, special attention is given to the creation of the pre-notch, which should be as sharp as possible to imitate conditions present during application. The tests are carried out using an *in-situ* scanning electron microscope (SEM) indenter in order to control the point of loading, assure mode I load conditions, and monitor possible violations. Conventional nanoindentation is used to determine the hardness as well as the indentation modulus. Additional studies based on X-ray diffraction, scanning and high-resolution transmission electron microscopy are conducted to characterize the microstructure of the coatings and to assess structure-property relations. Since the behavior at elevated temperatures is relevant for many applications, annealing treatments in vacuum and following characterization of these annealed samples are carried out.

The results clearly show strategies for enhancing the fracture toughness. We observe a fracture toughness peak, depending on the bilayer period (modulation period), similar to the well-known hardness peak for TiN/CrN superlattice systems on various substrates, produced with different PVD techniques. With the addition of boron to TiN we observe a significant improvement in hardness while the fracture toughness is not affected. Moreover, if hexagonal BN phases are avoided, an increase in fracture toughness can be realized. The influence of temperature on these properties (hardness and fracture toughness of nanolayered and B-alloyed coatings) is strongly depending on the involved phases. However, we identified proper approaches for retaining them under thermal loading.

Kurzfassung

Keramische Hartstoffschichten, die mittels physikalischer Dampfphasenabscheidung (engl. *physical vapor deposition* – PVD) hergestellt werden, können erfolgreich die Standzeiten von Werkzeugen der Zerspanungs- und Bearbeitungsindustrie um mehrere 100% verbessern. Dabei kommen ihnen ihre hohe Härte, die chemische und thermische Beständigkeit und ihre gute Oxidationsbeständigkeit zu Gute. Diese Eigenschaften bilden die Basis für die Anwendung in schwierigen Umgebungsbedingungen. Allerdings besitzen derartige Schichten nur eine relativ geringe Duktilität und niedrige Bruchzähigkeit, wodurch es bei starken Beanspruchungen durchaus zur Rissbildung und einem vorzeitigen Versagen kommen kann. Um den steigenden Anforderungen an derartige Schutzschichten gerecht zu werden und höhere Bearbeitungs- und Schnittgeschwindigkeiten zu ermöglichen, wird permanent nach neuen Materialien und Möglichkeiten geforscht.

Das Ziel dieser Doktorarbeit war es somit, einzelne Mechanismen zur Erhöhung der Zähigkeit von derartigen keramischen Hartstoffschichten im Detail zu untersuchen. Besonderes Augenmerk wurde dabei auf jene Mechanismen gelegt, die die anderen mechanischen Eigenschaften, wie Härte, nicht nachträglich beeinflussen. Mithilfe eines fokussierten Ionenstrahls wurden kleine Biegebalken aus den Hartstoffschichten gefertigt, die in einem Rasterelektronenmikroskop (REM) mittels mikromechanischer Versuche bis hin zum Bruch belastet wurden. Die simultan aufgenommenen Kraft-Durchbiegungskurven wurden unter Berücksichtigung des tatsächlichen Probenquerschnitts analysiert und zur Berechnung der Bruchzähigkeit herangezogen. Die Härte der Schichten wurde mittels konventioneller Nanoindentierung bestimmt. Mittels Röntgendiffraktometrie, Rasterelektronenmikroskopie und Transmissionselektronenmikroskop wurde die Mikrostruktur und der Schichtaufbau charakterisiert. Die thermische Stabilität der einzelnen Schichten und Mikrostrukturen wurde mit Vakuumglühversuchen und Differentialkalorimetrie geprüft.

Die Kombination dieser Untersuchungen erlaubte es, Mechanismen zu finden, die die Bruchzähigkeit zu erhöhen, ohne dass dabei die Härte oder auch die thermische Stabilität verringert wird. Die Entwicklung von sogenannten Superlatticeschichten (hier im System TiN/CrN erforscht) erlaubt die gleichzeitige Steigerung der Bruchzähigkeit und Härte. Auch

durch Zulegieren von Bor zu TiN kann dessen Härte deutlich gesteigert werden, ohne dass dabei die Bruchzähigkeit beeinflusst wird. Im Gegenteil, wenn vor allem die Bildung von hexagonalen BN Phasen verhindert werden kann, lässt sich dadurch auch die Bruchzähigkeit verbessern. Die thermische Stabilität derartiger Schichtkonzepte hängt sehr stark von den beteiligten Phasen ab, aber auch hier lassen sich optimale Konzepte identifizieren.

Introduction

Coatings are used to protect components from harsh environments and thereby enable to combine beneficial properties of both, the substrate and the coating. Ceramic coating materials (*i.e.* nitrides, carbides, borides, and oxides) are commonly known for their inherent hardness, their chemical stability, their thermal stability, and their oxidation resistance. The beginning of industrial application of hard coatings was in the 1980s where first tools were protected with TiN using chemical vapor deposition (CVD). From there on, the coating industry grew, leading to a share of coated to uncoated tools of $\sim 80\%$. Besides the tooling industry, the component industry becomes more and more important. This segment of the industry has a great potential, as of today only $\sim 10\%$ of suitable parts are coated [1–3].

Widely used techniques to deposit such thin films (usually in the range of $1\ \mu\text{m}$ up to $\sim 30\ \mu\text{m}$) are CVD, and its variations such as plasma assisted CVD, low pressure CVD; and physical vapor deposition (PVD). Especially PVD enables – due to the relatively low process temperatures, high cooling rates during film growth, and a wide variation in deposition parameters – a huge potential for further improvements of advanced hard coatings. These coating processes consist of three main steps: vaporization, transportation, and condensation. A further classification of different PVD processes is done by distinction of vaporization types (*i.e.* magnetron sputtering, cathodic arc evaporation, and laser or electron-beam vaporization) or types of condensation (reactive or non-reactive) [2, 4].

New requirements driven by industry in the search for improved efficiency, lead to the development of new coating systems with enhanced mechanical and chemical properties by academic and industrial research groups. In particular focus of recent developments are advances in mechanical and thermal properties (oxidation resistance as well as enhanced mechanical properties at increased temperatures [5–8]) for cutting tools in high speed cutting applications as well as enhanced component coatings leading to longer service life or higher service temperatures [9]. However, besides these properties, a premature failure due to spalling, cracking, and other mechanisms – leading to interaction of substrate and the

environment – has to be prevented. To avoid such unfavorable events, a coating needs a sufficient resistance against crack formation and crack growth, as well as an resistance to abrasive wear. The associated material properties for improvements are here the fracture toughness K_{IC} , the hardness H , and the Young’s modulus E . The present work focuses on the determination and improvement of K_{IC} , an inherent material property that became quantifiable for thin films very recently with advances in micromechanical testing methods [10–13].

The successful development of state-of-the-art protective coatings is often realized by applying concepts also used for bulk materials such as alloying, work hardening effects, and strengthening by reduction of the grain size. The mentioned mechanisms exist in thin films as: forming solid solutions of solvable and of even unsolvable constituents (*e.g.* the solution of AlN in TiN due to very high cooling rates in PVD processes), introduction of lattice defects such as point defects (vacancies, interstitial atoms) and line defects (dislocations), and the growth of nanocrystalline thin films respectively. All of these mechanisms successfully impede the dislocation movement, and hence lead to higher hardness values. In addition to those strengthening mechanisms, compressive stresses – arising from differences in thermal expansion coefficients (TEC) of thin film and substrate, as well as intrinsic growth-related stresses – further advance the hardness of a coating, peaking to hardness values well over 40 GPa (a threshold value for the definition as superhard material) [14, 15].

Increases in oxidation resistance are here accessible by alloying with oxygen-favoring elements such as Al, Si, or Zr. These additions often lead to a dense oxide scale in use, preventing further oxidation of the remaining thin film along with hindered outward diffusion of its constituent elements [16, 17].

Typical representatives and widely applied hard coatings in focus of these research efforts are TiN, TiB₂, TiAlN, CrN, TiC, and Al₂O₃ [2, 3].

1.1 Fracture Toughness

Though, as mentioned earlier, in industrial relevant applications the fracture toughness is of great importance because of dynamic loading profiles in use, including peak loads due to impact of small particles, cavitation, and interrupted cutting conditions. The fracture toughness of an intrinsic brittle material can be described as the resistance of a material to crack propagation and is therefore increasing with increasing energy needed for fracture. This was first described by Griffith [18] by finding that:

$$\sigma_f \cdot \sqrt{a} \approx C \quad (1.1)$$

and

$$C = \sqrt{\frac{2 \cdot E \cdot \gamma}{\pi}} \quad (1.2)$$

Where C is a constant, σ_f is the fracture strength, a is the flaw size, E denotes the Young's modulus, and γ the specific surface energy. Thus, mechanisms increasing the fracture toughness of a material are – according to Griffith – related to an increase in Young's modulus. The Griffith criterion however is only valid in the framework of linear elastic fracture mechanics, neglecting any plasticity at the crack tip and therefore the stress and the strain at the crack tip are infinite per definition. As this might be fulfilled for ideal brittle materials, it does not hold true for materials showing plastic deformation at the crack tip.

A modification established by Irwin [19] considers this effect, he therefore modified the Griffith criterion to:

$$\sigma_f \cdot \sqrt{a} = \sqrt{\frac{E \cdot G}{\pi}} \quad (1.3)$$

with:

$$G = 2 \cdot \gamma + G_p \quad (1.4)$$

where G is the total dissipated energy, and G_p is the energy dissipated mostly due to plastic deformation but also including other origins of energy dissipation. Here, the dissipation of energy because of plastic deformation can be understood as thermal energy due to frictional forces occurring during dislocation movements. Whereas G for brittle materials is in the order of $\sim 2 \text{ J} \cdot \text{m}^{-2}$ and dominated by the surface energy, for materials showing plastic deformation (thus G_p dominates the term) it is in the order of up to $1000 \text{ J} \cdot \text{m}^{-2}$. When G overcomes the threshold value G_c (the critical energy release rate) fracture occurs. This gives a first understanding how important the formation of a plastic zone can be in order to optimize the fracture properties of materials (even though this mechanism lowers the strength).

Another important parameter introduced by Irwin is the stress intensity factor K : for a small plastic zone size compared to the crack length, the energy required for growth of the crack is not decisively affected by stress state, therefore a purely elastic approach can be used [19, 20]:

$$K = \sqrt{G \cdot E} \quad (1.5)$$

for plane stress conditions. Transforming equation 1.5 using equation 1.3 gives the common

known equation for the stress intensity factor K :

$$K = \sigma_f \cdot \sqrt{\pi \cdot a} \quad (1.6)$$

In fracture mechanics exist three main modes of loading on a crack tip (figure 1.1):

- Mode I: load applied perpendicular to the crack plane (tensile, opening)
- Mode II: in plane shear loading (sliding)
- Mode III: out of plane shear loading (tearing)

hereby mode I present the most severe loading condition. Hence, together with a subscript c for “critical”, the formula symbol K_{IC} is defined as the critical stress intensity factor in mode I loading conditions and widely accepted as the defining parameter for fracture toughness [21, 22].

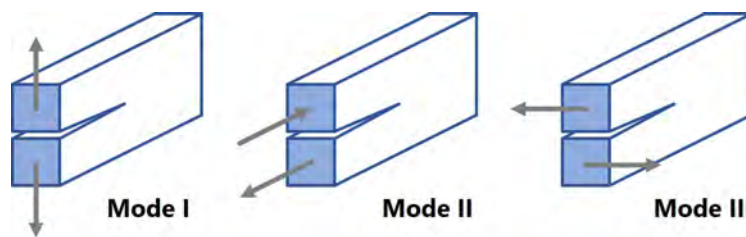


Fig. 1.1: The three main loading modes at crack tips.

However, as under testing conditions neither the notch radius is infinite small nor are the strain and stress tensor at the crack tip infinite large. Thus, a correction factor Y is introduced accounting for the stress distribution in a round notch tip. The validity of this correction factor was later verified by finite element simulations, the factor itself depends on the specimen geometry. Equation 1.6 then reads [20, 23]:

$$K_{IC} = \sigma_f \cdot Y \cdot \sqrt{\pi \cdot a} \quad (1.7)$$

a definition which will further be used in this thesis for calculation of the fracture toughness.

1.2 Ti-B-N Model System

Within the theoretical part of this thesis, TiN and Ti-B-N hard coatings are used as simple model systems to explain and illustrate various already known mechanisms. These coatings

were deposited and characterized within the framework of the thesis, however have yet to be published.

Thin Film Deposition

2.1 Physical Vapor Deposition

The main advantage of physical vapor deposition over other techniques for the preparation of thin films is its variety in adjustment options. Different deposition parameters enable to deposit metallic, ceramic, and even organic thin films in a broad property range. Typical varied parameters are the substrate temperature, the bias voltage accelerating process gas ions and other ionized species to the substrate, the applied power on the targets, the deposition pressure, the process gas mixture, and the target- and process gas elements. Furthermore, the selection of the PVD method significantly influences the coating properties. During any PVD process a target material is evaporated, transported through the vacuum deposition chamber and condensed on the substrate material leading to grain nucleation and subsequent film growth. Depending on whether process gas species (*e.g.* nitrogen or oxygen) react with the sputtered species or not a process is called reactive or nonreactive, respectively.

Further advantages of this technique are a low deposition temperature which enables to apply thin films on temperature sensitive substrates like high speed steel, high cooling rates (up to $10^{13} \text{ K}\cdot\text{s}^{-1}$) for the deposition of metastable materials, and the variety of different target materials and reactive gases.

There are two main deposition techniques widely applied in industrial processes: magnetron sputtering (including its derivatives) and cathodic arc evaporation which will be described in further detail [2, 4].

2.1.1 Cathodic Arc Evaporation

During cathodic arc evaporation (CAE) an arc is ignited on the target material (using currents in the order of 80 to 170 A, and voltages typically between 20 and 30 V) leading to a localized temperature peak followed by immediate evaporation of the target material [24]. The affected

area of this arc impact – the so-called cathode spot – is thereby in the order of 2 to 50 μm and exists for a few nanoseconds, after which immediately a next cathode spot occurs in the vicinity of the preexisting one. The limited area coupled with high currents, leads to current densities in the order of 10^{11} - 10^{12} $\text{A}\cdot\text{m}^{-2}$, resulting in an almost 100% ionization of the evaporated material. Further it shall be mentioned that a magnetic field behind the cathode can influence the arc flow, a technique described as steered arc. Besides the ions the process product consists of neutrals and macroparticles, which will be described later. An illustration of a cathodic arc process is depicted in figure 2.1:

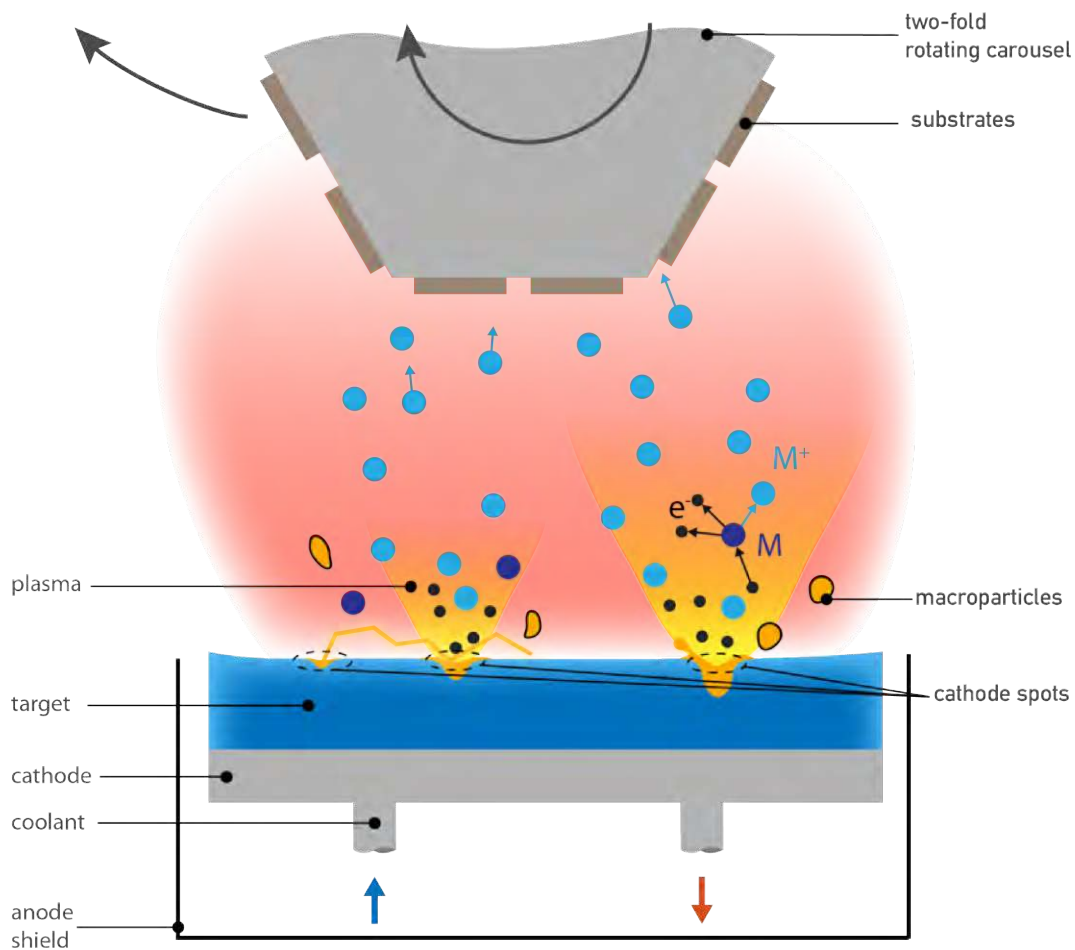


Fig. 2.1: Schematic cathodic arc evaporation process, after Koller [25].

The main advantage of this high ionization rate is a highly dense coating in the sense of compact column boundaries. Furthermore, ions are attractable by a negative bias voltage which guarantees a more uniform coating thickness even in shielded areas of the substrate.

The target erosion in a CAE process is characterized by a uniform erosion, maximizing the target usage rate. A further advantage compared to magnetron sputtering is the high deposition rate, both effects are causing economic benefits. Based on the presented advantages

cathodic arc evaporation has been established as preferred method for depositing hard coatings on cutting tools [2, 26–29].

Macroparticles

However, the before described high energy impacts also bring some disadvantages. The usually metallic targets conduct heat very well which leads, besides direct evaporation of the material, to melting pools in the vicinity of the cathode spot. The plasma pressure then causes the ejection of so-called droplets out of this melting pool. A schematic illustration of the droplet formation is shown in figure 2.2:

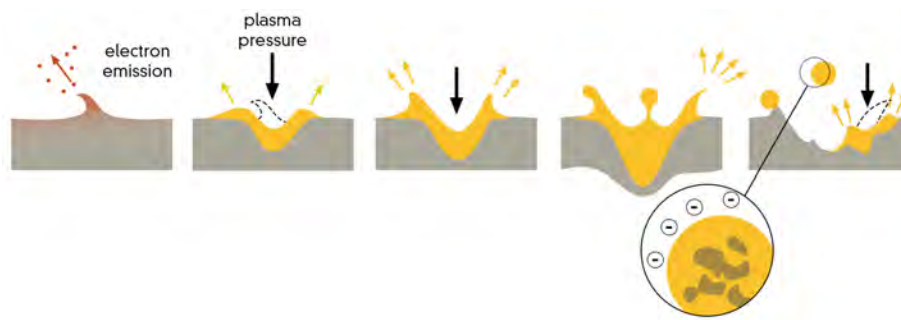


Fig. 2.2: Step-by-step formation of a droplet during cathodic arc evaporation [25].

When arriving at the substrate these metallic macroparticles are integrated in the growing thin film where they act as preferred areas for beginning failure of the coating (the soft metallic droplets have lower mechanical properties and often establish preferred diffusion pathways for oxygen). The macroparticles further suffer from a lowered coating adhesion [2, 30, 31].

2.1.2 Magnetron Sputtering

Impact Processes

During the magnetron sputtering (MS) process gas ions are accelerated to a target surface. As a result of the impact, momentum transfer takes place. Consequently, collision cascades are induced in the target, when those reach the target surface again and the energy is larger than the binding energy of the target atoms they are knocked out of the target. An important factor describing the effectiveness of this process is the sputter yield, a ratio describing the ejected atoms per impinging ion. This parameter depends on the atom mass, the impinging ion energy (which depends on the ion species and the acceleration voltage) as well as the bonding strength of the metallic bonding between the atoms. An overview of different sputter yields for Ar as the process gas using a typical acceleration voltage of 500 V as a function of atom mass is demonstrated in figure 2.3. A trend can be derived by recognizing that elements

with similar atomic masses can possess very different sputter yields, which reveals that the bonding strength of the target species (thus the sublimation energy) is the more influential factor on the sputter yield [32].

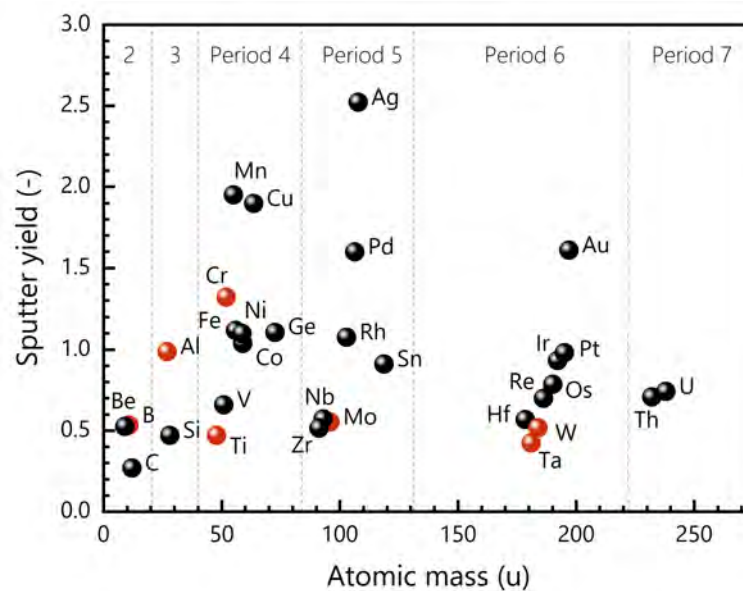


Fig. 2.3: Calculated sputter yields of different metals (+B, C, and Si) using Ar^+ ion with an acceleration voltage of 500 V (therefore the ion energy is 500 eV as Ar is single charged). The elements sputtered within this thesis are marked red (the values were calculated using [33]).

The previous considerations are only valid for targets consisting of one element only. Very recently Asanuma *et al.* showed that large atoms, such as Ta, Ce, or La, can have a ram effect leading to increased sputter yields and deposition rates for Ti-Al-N coatings [5, 6, 17].

Plasma Discharge

A basic requirement for this reaction is of course ionized species present that actually can be accelerated. Therefore, electrons are necessary which can be created using a variety of methods, however the most common one is plasma, which is defined as mixture of neutrals (atoms and molecules) and charged particles (electrons, positive and negative ions). The ignition and maintenance of plasma takes place as anomalous glow discharge between the cathode on the one side and the substrate on the other side. In DC magnetron sputtering plants this is done by applying a DC signal – other variants of sputtering use different signal types, *e.g.* a radio frequency, pulsed DC or a high-power impulse (HiPIMS) signal – in an Argon atmosphere with a total pressure between 0.1 and 1.0 Pa. During this process available electrons are accelerated and eventually inelastically collide with neutral Ar atoms leading to an ejection of further electrons leaving the Argon single positively charged. This is followed by an attraction of the Ar^+ ion to the cathode initiating the previously discussed impact

processes on the target surface. The plasma discharge, impact processes, and transportation of sputtered atoms are shown in figure 2.4 in an unbalanced magnetron configuration.

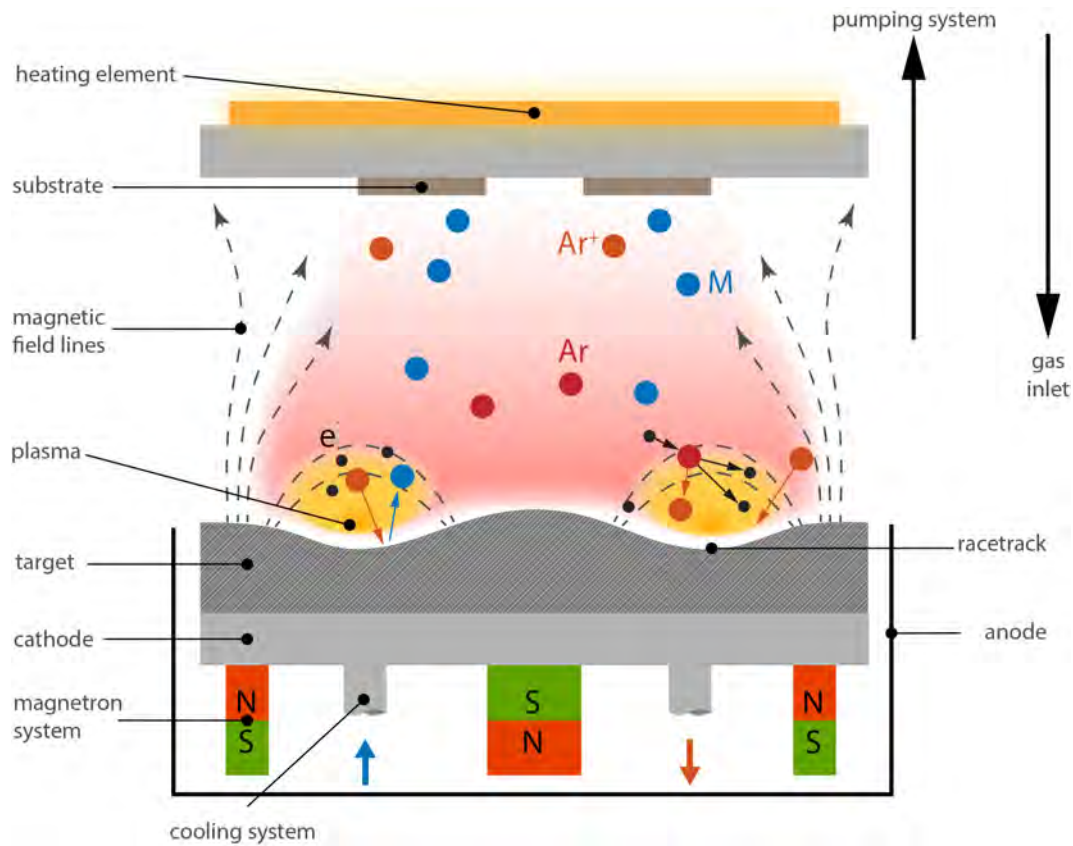


Fig. 2.4: Schematic magnetron sputtering process [25].

Magnetron

The role of a magnetron in this process is to concentrate electrons near the cathode surface and hence increase the sputtering efficiency. This is realized by the (unbalanced) magnetic field, stemming from either permanent magnets or electromagnets directly behind the target, which forces free electrons in a cyclonic movement in the vicinity of the cathode surface. Here, the magnetic field lines form a (closed) toroidal barrier for electrons as those experience a force orthogonal to the magnetic field lines. This is described by Lorentz-force [34]:

$$\vec{F} = q \cdot \vec{E} + q \cdot \vec{v} \times \vec{B} \quad (2.1)$$

where \vec{F} denotes the Lorentz force, q the electric charge, \vec{E} the electric field strength, \vec{v} the velocity, and \vec{B} the magnetic flux density.

The toroidal shape of the “electron-barrier” leads to the formation of a so-called race track, a preferred place of sputtering due to the electron concentration, leading to uneven target erosion.

In industrial processes the magnetic field lines are often not fully closed, thus the magnetron is an unbalanced magnetron. The non-closed field leads to a lower electron density as e^- can escape from their supposed environment. As a consequence, these electrons ionize Ar atoms between cathode and anode (substrate), which then are accelerated by a bias voltage. The implications of this process will be discussed in later chapters. The process using such configurations is then called unbalanced magnetron sputtering (UBMS), and is used for thin film deposition within this thesis [2, 35, 36].

Transportation

After being ejected, the sputtered atoms are moving towards the substrate and the chamber walls. The angular distribution of the sputtered species is thereby largely following a cosine distribution, whereas the energy distribution shows a Maxwell-Boltzmann distribution [37, 38].

Reactive and Non-Reactive Processes

Reactive gases (such as nitrogen, oxygen, and acetylene) are widely used to deposit transition metal nitrides, oxides, and carbides, respectively. The reaction of (sputtered) atoms with the reactive gas takes primarily place at the target surface and at the substrate or chamber wall. The formation of these ceramic layers on the target surface is called poisoning. This is an unwanted phenomenon as *e.g.* Al_2O_3 is a poor conducting compound which leads to voltage punctures (arcs) during the process. To avoid such poisoning the reactive gas content (partial pressure) has to be reduced until a transition regime in so-called poisoning curves is reached. In this transition regime (between pure metallic and pure ceramic sputtering) the target surface is, in the region of the race track, in metallic sputtering mode which increases the total sputtering rate. This increase is due to higher bonding strength and thus higher sublimation energy. To avoid poisoning also a deliberate positioning of the Ar gas inlet is helpful. In industrial available sputtering plants, these inlets are commonly placed near the cathodes, whereas the gas inlets for the reactive gases are located in the vicinity of the substrate.

The reaction on the substrate surface is dominated by diffusion processes and adatom mobility. Thereby the reactive species – target atom and reactive gas – and the substrate surface determine the speed of reaction. To further enhance the formation kinetics of the compound, Ar^+ ion bombardment can be applied by using bias voltage on the substrate.

Non-reactive processes on the other hand do not include any reactive species in the process, commonly Ar is used as the working gas (other noble gases like Helium, Krypton, and

Xenon are not widely used because of their lower atomic mass in case of helium, or because of economic reasons for the other noble gases). During non-reactive sputtering the target elements determine the film components. Hence, compound targets are used for the deposition of ceramic thin films, *e.g.* TiN on a copper backplate. For a new class of thin films systems – transition metal diborides – these compound targets are conditional. However, the chemical composition is not only determined by the target composition: light elements such as boron are subject to collision during transportation to the substrate, and because of their low mass, they are more influenced (deflected) by other atoms. This leads to an inverse relation between the deposition pressure and the boron content in the thin film (as measured for example in paper IV) [2, 4, 39].

2.2 Film Nucleation and Growth

2.2.1 Nucleation

Usually substrate materials differ from the thin film material in structure and elemental composition. Therefore, before a film can grow, nucleation has to take place. In a first step the impinging atoms are adsorbed on the substrate. When several atoms combine themselves to a cluster, a first nucleus occurs. However, in this phase the atoms still have enough mobility to separate from the cluster, this means a certain nucleus size has to be overcome to be stable. Although being stable, when two of these cluster touch each other, coalescence takes place due to minimization of the total energy (saving of free surface energy). These bigger islands then grow together until the whole substrate is covered and the nucleation phase is complete [40, 41].

2.2.2 Film Growth

Depending on the binding energies between film and film atoms, and film and substrate atoms, three types of film growth can be observed [35]:

- Volmer-Weber (three-dimensional island formation)
- Frank van-der-Merwe (two-dimensional layer-by-layer growth)
- Stranski-Krastanov (combined growth)

Whereas a preferred film-film atom interaction results in island growth a favored substrate-film will lead to a layer-by-layer growth. Volmer-Weber growth is for example observed during sputtering of Silver on SiO₂ substrates, whereas pure Frank van-der-Merwe growth can be



Fig. 2.5: Illustration of the three main growth modes observed during magnetron sputtering [35].

observed during heteroepitaxy of TiN on MgO. Figure 2.5 shows the growth modes usually observed during magnetron sputtering.

During sputter deposition of polycrystalline thin films of transition metal nitrides and borides (TMN and TMB) usually a Stranski-Krastanov growth is observable. Hereby both, layered and island growth are in competition to each other, however it is often observed that initially a layered growth starts that merges into three-dimensional island growth.

Structure Zone Models (SZM)

The growth morphology, which determines – besides the chemical composition – primarily the mechanical properties of the coating, can be described by so-called structure zone models (SZM). These models were developed to derive information on the influence of varying parameters on a given or unknown morphology. The first such model was published by Movchan and Demchishin [42] in 1969 for evaporated coatings. They illustrated 3 different growth morphologies depending on the homologous temperature T/T_m where T_m is melting temperature in K and T is the substrate temperature in K. At low temperatures (zone 1) they found a porous coating due to low mobility of the adatoms. Zone 2 describes a dense columnar film morphology with smooth surface, and zone 3 shows a recrystallized structure with non-oriented grains.

Based on this study, Thornton (1974) [43] and Messier (1984) [44] developed models for magnetron sputtered coatings including the deposition pressure and bias voltage (energy) as additional variable respectively. Thereby a new structure-zone was described: zone T.

Zone T

In this field, competitive growth between different crystallographic oriented grains takes place. In the case of TiN, the (111) orientation grows faster than the (100) because the (111) plane has equal amounts of Ti and N atoms, hence a lower potential energy. However, the lateral growth is faster for the (100) orientation, as a result the coating has large (111) crystallites in

growth direction and a large area covered with (100) oriented crystal [40]. Such a morphology is shown in figure 2.6:

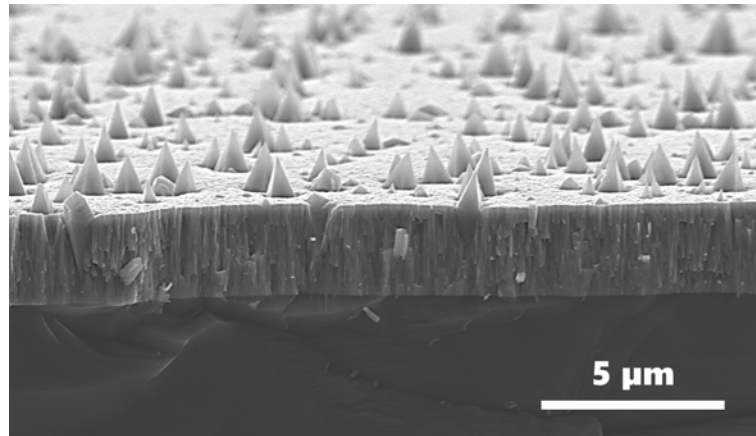


Fig. 2.6: Scanning electron microscopy (SEM) fracture cross section of a non-reactively magnetron sputtered TiN coating on silicon (100) showing large (111) crystallites whereas the remaining surface is covered by (100) oriented columns.

Influence of Deposition Pressure

The influence of the deposition pressure was described by Thornton. He observed a widening of zone T and similarly a shift to lower temperatures of zone T and zone 2 with decreasing Ar pressure. The explanation of this behavior is a reduced interaction of sputtered species with gas atoms during transportation from the target surface to the substrate, thus the energy and the adatom mobility increases with decreasing sputtering pressure [43]. Figure 2.7 shows two non-reactive sputtered TiN thin films with differing Ar pressures:

One can see on this fracture cross sections dense column boundaries and competitive growth in (a), and underdense columns (b).

Influence of the Bias Voltage

The influence of the bias voltage on the microstructure of a sputtered coating was described by Messier *et al.* in 1984 [44]. They found a widening of zone T and a shift to lower substrate temperatures with increasing bias voltage. Again, similar to the observations of Thornton, an increasing energy yielding an increased adatom mobility. Figure 2.8 shows two non-reactively sputtered TiN coatings with different applied bias voltages:

A smoother surface as well as a smaller column size is apparent in figure 2.8b compared to figure 2.8a. The surface roughness was not quantified, however an x-ray diffraction (XRD)

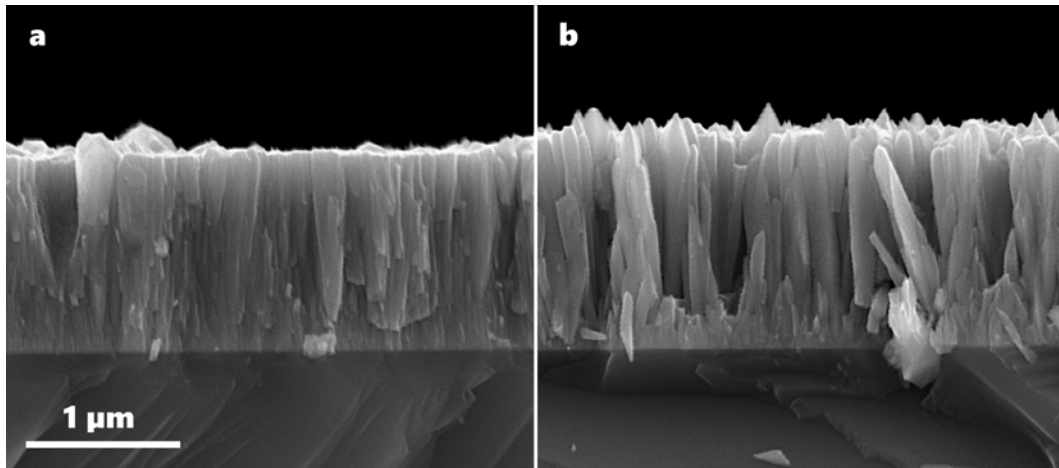


Fig. 2.7: SEM fracture cross sections of two non-reactively magnetron sputtered TiN coatings on silicon (100). The thin films were deposited at the same substrate temperature (400 °C), using the same bias voltage (-40 V), applying the same target current (0.75 A), but at different deposition pressures: (a) 0.4 Pa and (b) 0.7 Pa. Both micrographs were taken using the same magnification.

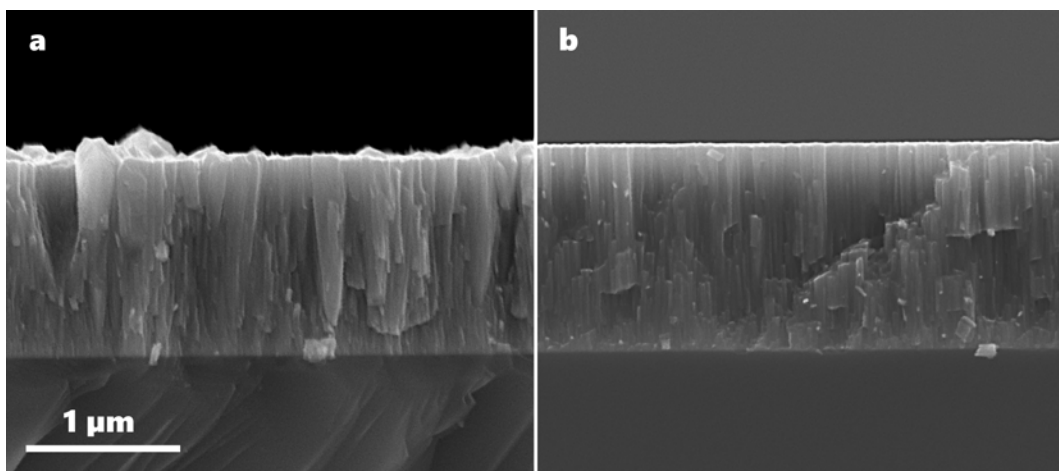


Fig. 2.8: SEM fracture cross sections of two non-reactively magnetron sputtered TiN coatings on silicon (100). Picture (a) is the same coating as in figure 2.7a, but (b) is deposited using -80 V bias instead of -40 V. The magnification is identical for both micrographs.

analysis of the (111) peak derived a crystallite size of ~ 60 nm and ~ 24 nm for -40 V and -80 V bias voltage respectively.

Normalized Structure Zone Model

In 2010 Anders [45] presented an extended structure zone model also suitable for high ion fluxes, usually present in cathodic arc evaporation and HiPIMS processes. In this model the temperature axis, as well as the energy flux axis are normalized. This is especially useful for the latter, as energy can be delivered to the system in different ways, as shown before.

Additionally, the resulting film thickness as well as the ion etching region are featured in this model, shown in figure 2.9:

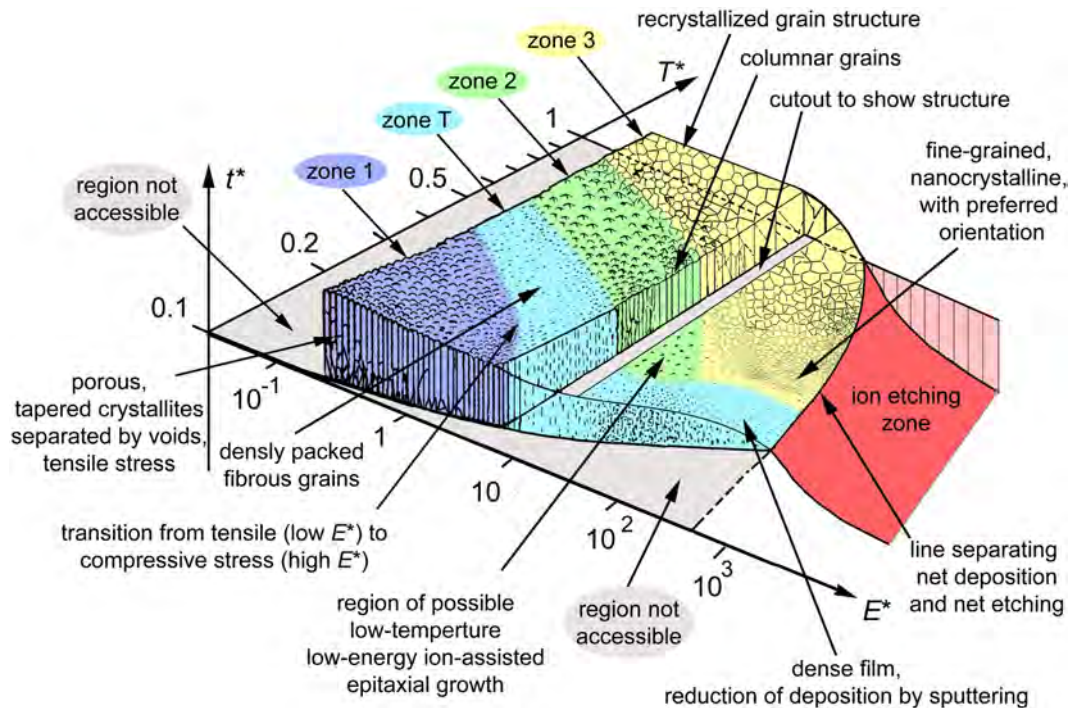


Fig. 2.9: Structure zone model after Anders [45].

2.3 Experimental

Within the thesis several methods were applied to examine the microstructure, the elemental composition, as well as the mechanical and thermal properties of thin films. However, most of these methods are widely applied over several fields of materials science, physics and chemistry, therefore in the following section only the most important property for this work is described in detail: the determination of fracture toughness K_{IC} .

The experimental setup in this thesis was following:

- AJA International Orion 5 for deposition of Ti-B-N coatings using a total Ar-pressure of 0.4 Pa (the Ar flow was set to 10 sccm, the process was pressure controlled), a substrate heater temperature of 600 °C, -60 V bias, varying target (TiN, TiB₂, and Ti, all from Plansee composite materials GmbH, at least 99.6% purity) currents from 0.05 to 0.75 A to obtain different chemical compositions, and a standard substrate (Si (100) and Al₂O₃ (1̄102)) cleaning procedure before deposition (acetone, ethanol, and Ar⁺

plasma-etching). Details on the deposition parameter for other coatings are specified in the respective publication.

- FEI Quanta 200 3D Dual Beam FIB operated at 30 kV and different milling currents
- FEI Quanta 250 FEGSEM operated at 10 kV
- XPERT II: PANalytical XPert Pro MPD (θ - θ diffractometer) equipped with a CuK_α radiation source ($\lambda = 0.154 \text{ nm}$), operating in Bragg-Brentano geometry
- UMIS Nanoindentation equipped with a diamond Berkovich tip
- Centorr VI LF series vacuum furnace
- Hysitron PI-85 SEM PicoIndenter for *in-situ* micromechanical testing

2.3.1 Fracture Toughness Testing

There are several methods available for testing the fracture toughness of bulk materials such as compact tension (CT, DIN EN ISO 12737) for ductile materials, and the single edge v-notched beam (SEVNB) method for brittle materials such as ceramics. For both tests, the load is applied in a way to create tensile stresses at the pre-crack tip.

The assessment of the fracture toughness of thin films is – due to the small film thicknesses – not easily accessible. However, there are several methods available [46–50]:

- Indentation fracture:
 - Evaluation by measuring radial crack length
 - Fracture energy-based method
- *In-situ* micromechanical testing
 - Pillar splitting
 - Micro-cantilever testing

Indentation Fracture Methods

Indentation fracture methods base upon crack formation as a consequence of stress intensities at the indenter edge or – in case of the energy-based method – on cracking due to delamination, subsequent buckling and following chipping of the thin film. In both cases the system (coating and substrate) is tested, which leads to influences of the substrate on the measured fracture toughness. Hence, the term fracture toughness is inaccurate, the preferred term for these values is “apparent fracture toughness” seems to be more appropriate, already suggesting an

external influence. The benefit of this methods however is the relatively straightforward and fast testing procedure: A series of indents using a cube corner diamond tip with different loads leads to desired cracking events. Thereby load-deflections curves are recorded and analyzed. In case of the classical indentation fracture – a method also available for bulk ceramics using a Vickers diamond – the crack length is afterwards measured using the SEM. Thereof, the fracture toughness is calculated using following equation [46]:

$$K_{IC} = \alpha \cdot \left(\frac{E}{H} \right)^{1/2} \cdot \frac{P_{max}}{c_f^{3/2}} \quad (2.2)$$

where E is the Young's modulus of the coating, H the hardness, P_{max} the maximum indenter load, c_f the measured fracture length, and α the indenter geometry coefficient.

Using the energy-based method the apparent fracture toughness of the coating is calculated as follows [51]:

$$K_{IC} = \sqrt{\frac{E \cdot U_f}{(1 - \nu^2) \cdot 2\pi \cdot C_r \cdot t}} \quad (2.3)$$

where U_f is the dissipated energy during fracture, ν the Poisson ratio, C_r the delamination radius measured in the SEM, and t the film thickness.

Pillar Splitting

Pillar spitting is an *in-situ* micromechanical method to determine the fracture toughness without the influence of residual stresses. In a first step a pillar is produced using a focused ion beam microscope (FIB). The dimensions of this pillar are a height similar to the film thickness and a height to diameter ratio larger than one. The pillars are then indented until fracture using a cube corner diamond tip. This procedure is usually conducted *in-situ* in a SEM as the positioning of the indenter tip is crucial for the validity of the calculated fracture toughness. The measured parameter during the test is the indenter force as the pillar split, P_c . The fracture toughness is then derived by following cohesive zone finite element method (CZ-FEM) proven computed formula:

$$K_c = \gamma_p \cdot \frac{P_c}{R^{3/2}} \quad (2.4)$$

with R being the pillar radius, and γ the CZ-FEM based calibration coefficient. Details on the calculation of γ_p can be found in [52, 53].

2.3.2 Single Cantilever Bending Test

Single cantilever bending tests are a widely used technique to measure the fracture toughness of hard coatings, additionally they are also capable to determine K_{IC} of micrometer-sized features in of bulk materials. This method allows, like pillar splitting, the determination of the fracture toughness K_{IC} without the influence of the substrate [11, 13, 54–56].

Thereby microcantilever with defined dimensions are FIB-milled and subsequently loaded until fracture. Within this thesis tested cantilever had target dimensions depending on the film thickness t :

- The length l of the cantilever was $7 \cdot t$
- The width b had the same dimension as t
- The height w was also in the dimension range of t

The initial notch had a depth a of ~ 0.2 to 0.3 of the height w , and was milled in a sufficient large distance to the root of the cantilever to avoid complex stress states, deviating from mode I loading conditions. The milling conditions were chosen to minimize FIB damage in sensitive areas of the cantilever: 5.0 nA for coarse cuts when etching of the substrate was not possible (Si was usually etched away by $\sim 10 \mu\text{m}$ from the edge using a $40 \text{ wt.}\%$ aqueous solution of KOH at a temperature of $70 \text{ }^\circ\text{C}$ to obtain free standing thin film material), 1.0 nA for FIB-milling in the vicinity of the cantilever, and 0.5 nA for the final milling step defining the shape. The initial notch was milled using a current of 50 pA . The actual notch depth was measured after testing, however to predict the depth, a series of notches with differing milling times was made, Pt coated and the cross section was investigated using a SEM equipped with a field emission gun (FEGSEM).

The testing was carried out with a Hysitron PI-85 SEM PicoIndenter equipped with a spherical diamond tip (the tip radius was $\sim 1 \mu\text{m}$) in displacement-controlled mode ($5 \text{ nm}\cdot\text{s}^{-1}$). Before loading the indenter was carefully placed in the middle of the width of the cantilever, $\sim 500 \text{ nm}$ away from its free end and approached to a distance of $\sim 200 \text{ nm}$ away from the surface. The indenter axis is perpendicular to the cantilever surface to assure a pure bending load in the cantilever cross section and hence have mode I load condition in the pre-notch front.

The fracture toughness was then calculated according to Matoy *et al.* [11]:

$$K_{IC} = \frac{P_{max} \cdot l}{b \cdot w^{3/2}} \cdot f\left(\frac{a}{w}\right) \quad (2.5)$$

with

$$f\left(\frac{a}{w}\right) = 1.46 + 24.36 \cdot \left(\frac{a}{w}\right) - 47.21 \cdot \left(\frac{a}{w}\right)^2 + 75.18 \cdot \left(\frac{a}{w}\right)^3 \quad (2.6)$$

with P_{max} the load before fracture and f a geometry function. The maximum force was determined using a Wolfram[®] Mathematica[®] script analyzing the load-deflection curve. The dimensions of the cantilever were determined after fracture (except the point of load incidence) in fracture cross section micrographs recorded with the SEM.

To ensure the validity of these tests and get an idea of the robustness of the method under uncertainties of the cantilever and initial notch dimensions, Brinckmann *et al.* performed several FEM calculations. They found major deviations in stress intensities at the crack tip for smaller cantilever length as well as for too small initial notch depth [57, 58].

The presented method is valid for linear elastic behaving (brittle) materials, however recent research also provides methods for semi-brittle materials such as bcc-metals and even ductile materials using and J-integral approach [10].

Mechanical Properties

The mechanical properties of materials are determined by their intrinsic bonding properties and extrinsic mechanisms weakening or strengthening the material. Extrinsic mechanisms are either based on a modification of the microstructure or rest on hindered dislocation motion because of local stress fields (solid solution strengthening). In materials science there are four basic strengthening mechanisms known, which will be introduced in the following subchapter [14].

3.1 Strengthening Mechanisms

3.1.1 Solid Solution Strengthening

Solid solution strengthening is based on the introduction of local stress fields as solvent atoms and solute atoms may differ in size. This size difference results in local stress fields around the solute atom that interact with dislocations and hence impede the motion of it. The strengthening thereby scales with:

$$\Delta\tau \propto \sqrt{c} \quad (3.1)$$

where τ is the stress to move dislocation, and c is the solute concentration.

In hard coatings this mechanism is successfully applied in the Ti-Al-N system where AlN can be solved in the TiN – due to high cooling rates – and increases the hardness by several GPa. Also, on the non-metal sublattice alloying can be implemented, exemplified by the Ti-B-N system: Here boron atoms replace nitrogen on the non-metal sublattice leading to a hardness increase, see figure 3.1.

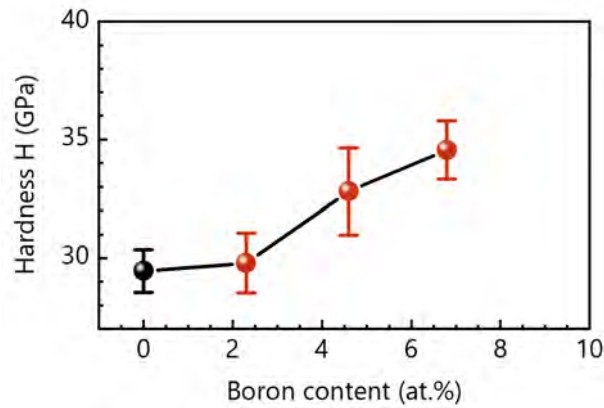


Fig. 3.1: Nanoindentation hardness of B alloyed TiN. An x-ray diffraction (XRD) analysis of these coatings revealed similar column sizes for all tested thin films.

XRD patterns of these coatings are presented in figure 3.2. No formation of TiB_2 was observed in our coating, as the elemental composition was varied along the TiN-TiB tie line in the ternary Ti-B-N phase diagram. This was realized by sputtering an additional Ti target. The peak shift in the patterns with increasing B content can therefore be attributed to the formation of a solid solution (the stresses necessary for such a peak shift would be in the order of ~ 8 GPa).

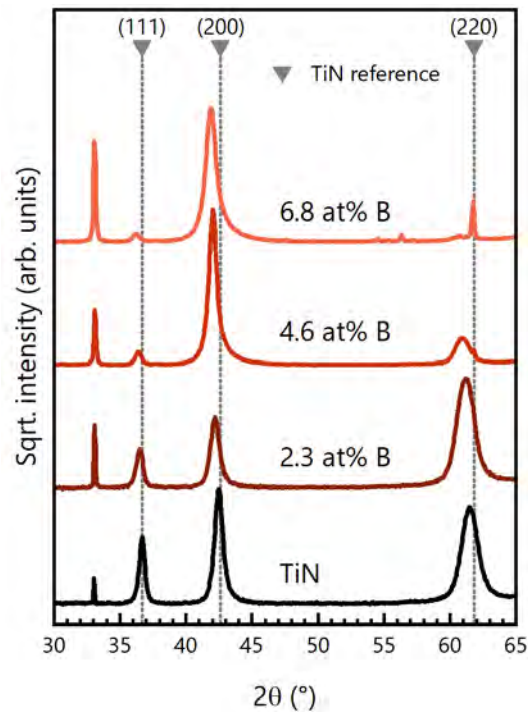


Fig. 3.2: XRD patterns of Ti-B-N coatings along the TiN-TiB tie line.

The overall stresses in the Ti-B-N coatings in figure 3.1 vary between -0.9 ± 0.1 GPa (compres-

sive stress) for ~ 2.3 at% B and -2.6 ± 0.2 GPa for the TiN and ~ 6.8 at% B. The coating with ~ 4.6 at% B has a residual stress of -1.8 ± 0.2 GPa. Therefore, the hardness improvement of ~ 5 GPa from TiN to Ti-B-N with ~ 6.8 at% B can be attributed to solid solution strengthening due to non-metal alloying with boron.

3.1.2 Grain Refinement Strengthening

This hardening mechanism is based on hindered dislocation motion over a grain boundary. This results in a dislocation pile at the grain boundary and a consequential increase in strength. With an increasing grain boundary density, the strengthening increases following the Hall-Petch relation [59, 60]:

$$\Delta\tau \propto \frac{1}{\sqrt{d}} \quad (3.2)$$

where d is the grain size of the material. The mechanism however does not work for very small grain sizes (the limit is materials depending and in the order of some nm), as grain boundary sliding events take place, what is called inverse Hall-Petch relation.

Grain refinement strengthening is also applied in thin film technologies, the column size (diameter) can for example specifically adjusted by varying the bias voltage. Also annealing and the occurring recovery and recrystallization lead to a change in column size, however they cause an increase the grain size (figure 3.3).

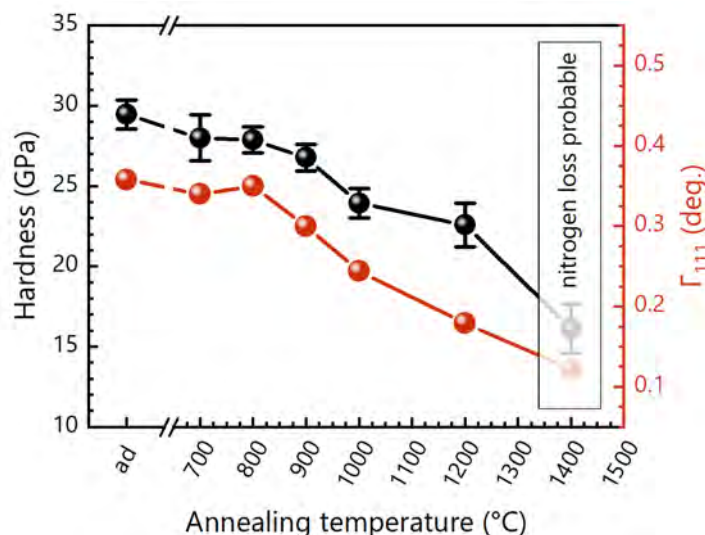


Fig. 3.3: The hardness of TiN as a function of the annealing temperature (30 min holding time and a heating rate of $20 \text{ K} \cdot \text{min}^{-1}$). The red dots belong to the right axis, the full width at half maximum (FWHM), derived from XRD measurements [61].

A decrease of the full width at half maximum (FWHM) is observed for TiN with increasing annealing temperature, the corresponding XRD patterns are shown in figure 3.4:

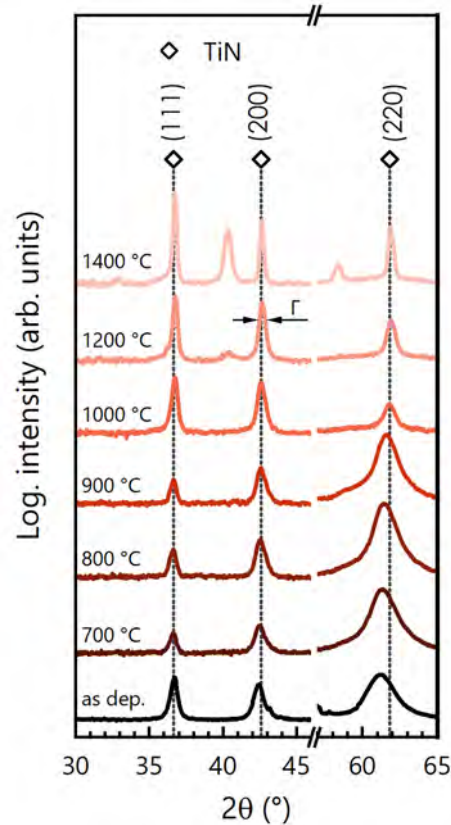


Fig. 3.4: XRD patterns of TiN coatings deposited on sapphire with different annealing temperatures T_a [61].

The FWHM is the width of an XRD-peak at the half intensity of this peak. Assuming the validity for thin films of the relation given by Scherrer [62]:

$$L = \frac{K_S \cdot \lambda}{\Gamma \cdot \cos(\theta_0)} \quad (3.3)$$

with L being the crystal size, K_S a dimensionless shape factor, λ the x-ray wavelength, Γ the FWHM, and θ_0 the Bragg angle. Presuming a constant shape factor with increasing annealing temperature T_a , and only minor changes in the Bragg peak position (due to reduction of residual stresses) measured with the same instrumental setup one can identify an inverse relation of crystallite size and FWHM:

$$L \propto \frac{1}{\Gamma} \quad (3.4)$$

Therefore, an increase in grain size is observed with increasing annealing temperature, while the hardness of TiN is decreasing with increasing temperature. Figure 3.5 shows the hardness vs. the FWHM.

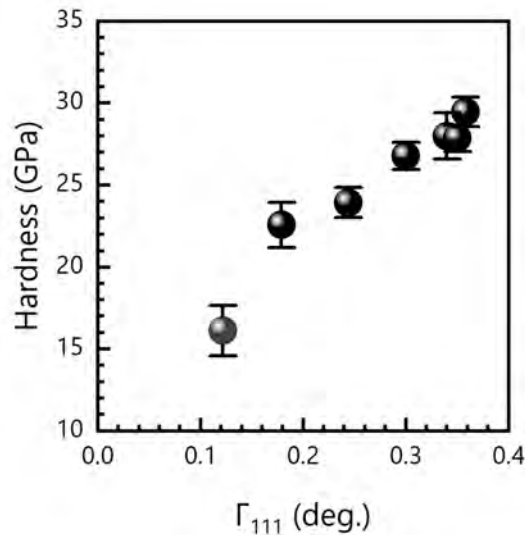


Fig. 3.5: Hardness vs. FWHM of non-reactively sputtered TiN in different annealing states [61].

Also, for the TiN thin films shown in figure 2.8, a hardness increase from 19.5 ± 3.4 (a) GPa to 25.0 ± 0.8 (b) GPa was observed. Here the large error bar for (a) is due to the rough surface influencing the projected indentation area. A similar effect can be observed in multilayered [63] coatings where a reduction in apparent column size is reached by the interfaces between the constituents. Although these can grow in a coherent manner, the difference in mechanical properties leads to strengthening of the thin film.

3.1.3 Cold Work Strengthening

Cold work hardening draws upon hindered dislocation motion due to mutual obstruction of dislocations. Also point defects interact with dislocations leading to increased strength and hardness. The hardness increase can be quantified using [14]:

$$\Delta\tau \propto \sqrt{\rho_{\perp}} \quad (3.5)$$

with ρ_{\perp} being the dislocation density. Thin films demonstrate a comparatively high dislocation (defect) density due to the very fast cooling rates. Hence, the potential for further increase is less pronounced compared to the other mechanisms. Though this effect could be observed

when thin films are annealed at temperatures well below any possible recrystallization (and hence grain growth), but recovery takes place.

3.1.4 Precipitation Strengthening

When a dislocation moves through a crystal lattice and comes upon a precipitation, Kelly and Fine found for coherent precipitations following strengthening rate (up to a critical particle radius r_c where cutting of the precipitate takes place):

$$\Delta\tau \propto \sqrt{r_p \cdot f_p} \quad (3.6)$$

where r_p is the particle radius and f_p is the particle fraction. If the radius of the precipitation exceeds r_c , the dislocation will bypass the precipitation, the strengthening thereby scales with (after Orowan):

$$\Delta\tau \propto \sqrt{f_p} \cdot \frac{1}{r_p} \quad (3.7)$$

Incoherent particles are not subject to cutting mechanisms they are instead always bypassed by a dislocation. Precipitation strengthening is preferentially applied in metallic materials for example in age hardened Al-alloys or oxide dispersion strengthened steels. In thin films materials this hardening mechanism can be deployed for instance by co-sputtering a metal that does not form any compound with the reactive gas or the non-metal constituent. This is for example realized in nc-TiN/Ni coatings. It has to be noted however, that these additions also lead to nanograin structures, hence the hardening is also covered by grain refinement [64].

3.2 Fracture Toughness Enhancement

Electronic Properties of Materials

As discussed in the introduction of this work, the fracture toughness of brittle materials can be influenced by the bonding conditions of a material. These in turn are characterized by the electron structure and the resulting electronic properties of its atoms. Two separated atoms attract each other due to a dipole moment, with decreasing atomic distance, these interactions become stronger. However, when they get too close their electron shells are interacting, leading to a repellent force. The sum of these interactions results in so-called binding potential curves. The progression of these curves is defined by potential functions, the most common are the Morse-potential (exponential approximation) [65]:

$$V = D \cdot (e^{[-2\alpha \cdot (r-r_0)]} - 2 \cdot e^{[-\alpha \cdot (r-r_0)]}) \quad (3.8)$$

and the Lennard-Jones-Potential (power-law approximation) [66]:

$$V = \frac{A}{r^{12}} - \frac{B}{r^6} \quad (3.9)$$

where V is the potential, A , B , D , and α are constants, r is the atomic distance, and thus r_0 the equilibrium distance.

The progression of such a Lennard-Jones-potential is demonstrated in figure 3.6 (black line).

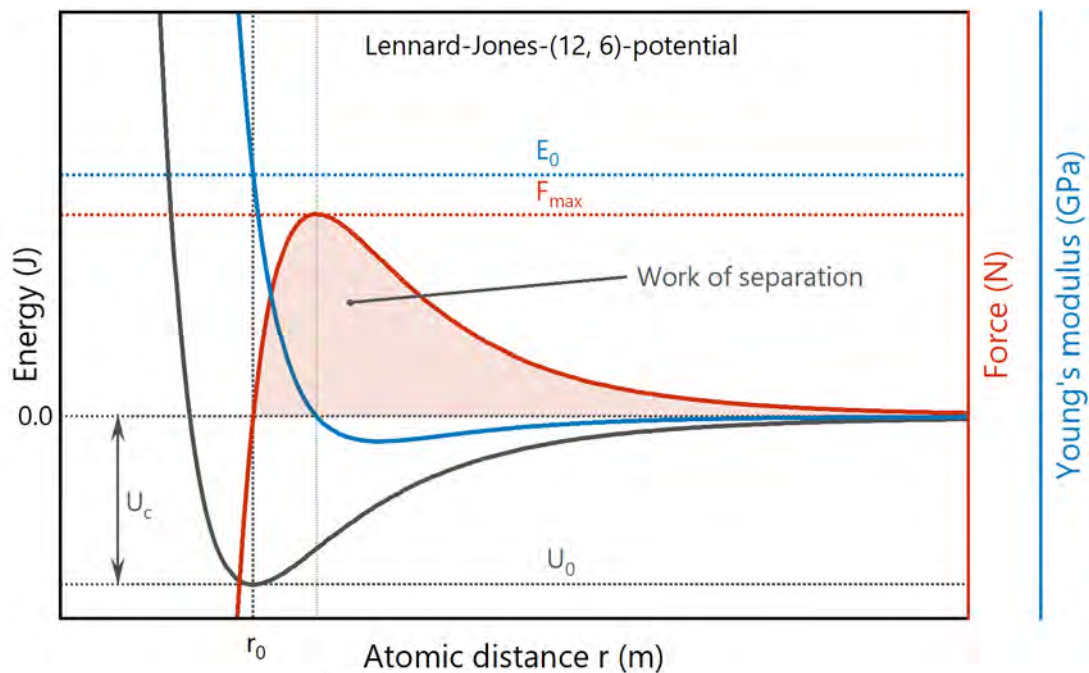


Fig. 3.6: Lennard-Jones-(12, 6)-potential with the first and the second derivate (a measure for the binding force and the Young's modulus respectively).

If a material is cleaved – separated from r_0 to r_∞ – the energy which has to be overcome is then the difference in U_0 and the energy at r_∞ ($\stackrel{\text{def}}{=} 0$), referred to as cleavage energy U_c .

The first derivation (red line in figure 3.6) of the energy gives the force that is necessary to change the atomic distance (with regard to the proportional area of one atomic bonding in the crystal lattice, the first derivation gives the mechanical stress). The area under this curve can then be defined as work of separation.

The change of the first derivation with the distance – the slope of the curve, or the second derivation (blue line in figure 3.6) – is then defined as the Young's modulus of the material. This can be explained straightforward by remembering Hooke's law for linear elastic behavior

(here given for isotropic materials):

$$\sigma = E \cdot \epsilon \quad (3.10)$$

With σ being the stress, and ϵ the strain:

$$\epsilon = \frac{\Delta r}{r_0} \quad (3.11)$$

hence the stress divided by the strain (change of bonding length) is the Young's modulus. Importantly the Young's modulus is an experimental available parameter and proportional to the cleavage energy. According to Griffith (equations 1.1 and 1.2), the square root of γ and E (the surface energy γ is by definition related to the cleavage energy as during cleavage two new surfaces are generated) is proportional to the fracture strength and thus the fracture toughness:

$$K_{IC} \propto \sqrt{E \cdot U_c} \quad (3.12)$$

Yet, these considerations do not account for any possible plasticity in the vicinity of the crack tip and are therefore valid for brittle materials.

The Role of Plasticity

Further contribution to fracture toughness enhancement can be realized by increasing the plastic deformability of a material. The underlying mechanism is a raise in the energy needed for cleavage U_c : ductile materials show – according to Sangiovanni *et al.* – the ability to recover atomic bonding during cleavage. The reason for this behavior is attributed to highly populated d-d metallic bonding states in such ceramic materials [67–69].

To assess the population density of states as well as gain information on the specific curvature of the binding potential, density functional theory calculations can be utilized. This quantomechanical approach is widely used in materials science, however as it is not a focus of this thesis, the reader is referred to reference [70] for basic information and further details.

3.2.1 Fracture Properties of the Ti-B-N System

In the Ti-B-N model system besides the coating series along the TiN-TiB tie line, a second series along the TiN-TiB₂ tie line was deposited. The hardness of this coatings is slightly higher compared to coatings on the TiN-TiB tie line, as presented in figure 3.7:

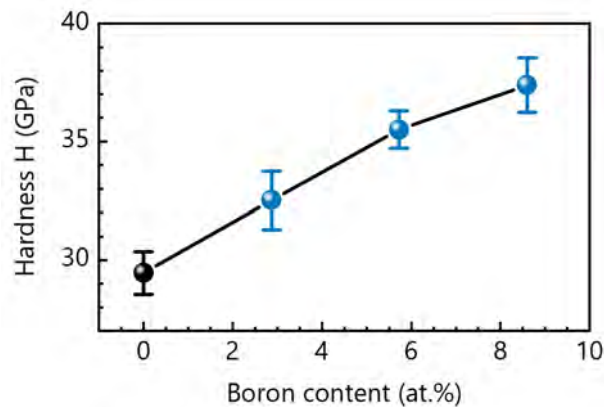


Fig. 3.7: Hardness of Ti-B-N coatings as a function of the boron content. The coatings were deposited along the TiN-TiB₂ tie line.

This series also has a lower grain size compared to the TiN-TiB system, as one can identify on the XRD patterns in figure 3.8:

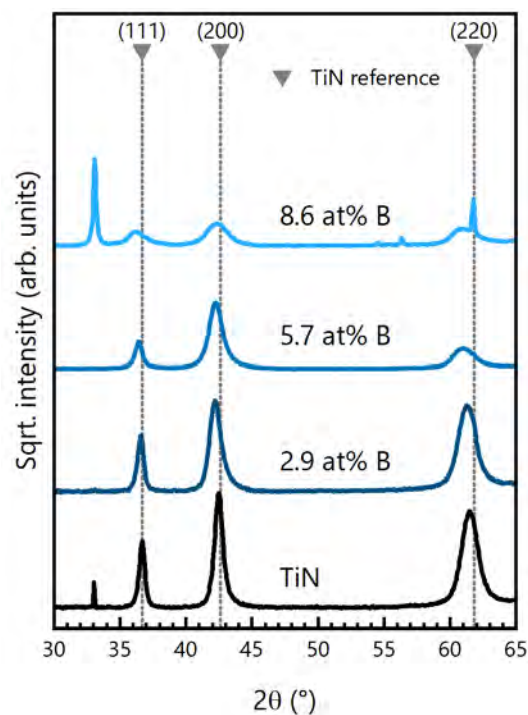


Fig. 3.8: X-ray diffraction patterns of B alloyed TiN coatings. Here the elemental composition is along the TiN-TiB₂ tie line.

Here the boron alloying does not lead to such a peak shift as observed for the TiN-TiB tie line patterns, this is a first indication that the boron is not fully incorporated as solid solution element in TiN, instead a migration to the grain boundaries is imaginable, causing the small grain size. Consequential, the higher hardness of this coating series compared to TiN-TiB

coatings can be explained. However, the measured fracture toughness values reveal a different picture. A slight increase in fracture toughness is observed for the TiN-TiB coatings, whereas the TiN-TiB₂ coatings show a significant drop in fracture toughness (see figure 3.9):

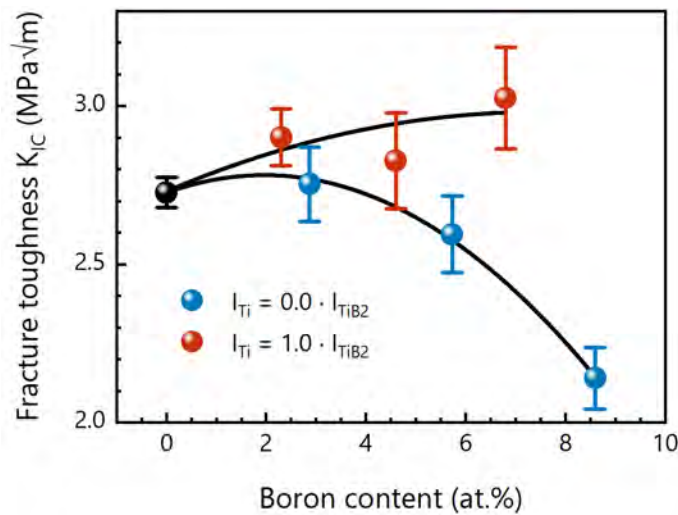


Fig. 3.9: Fracture toughness K_{IC} of TiN-TiB and TiN-TiB₂ tie line coatings measured using *in-situ* single cantilever bending tests, calculated under the condition of linear elastic fracture mechanics. The line connecting the data points is a parabolic fit guiding the eye.

Here the slight increase in K_{IC} for the TiN-TiB coatings with increasing boron content is attributed to toughening by increasing the ductility of the coating, as the Young's modulus of this coating series is actually decreasing with increasing boron content:

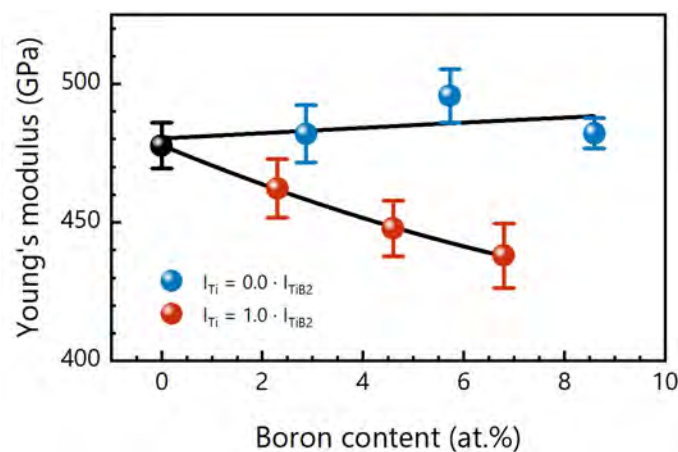


Fig. 3.10: The Young's modulus vs. the boron content of coatings with an elemental composition on the TiN-TiB and TiN-TiB₂ tie line.

Therefore, when boron is dissolved in the TiN matrix, a slight improvement in ductility is obtained. In turn, as soon as boron cannot be dissolved in TiN, it segregates to the column boundaries, leading to earlier, brittle failure.

3.2.2 Other Mechanisms Increasing the Fracture Toughness

Besides the described enhancement (and lowering) in K_{IC} for the Ti-B-N system, other mechanisms were investigated within this thesis. These are presented in the upcoming sections (publication I to publication III and publication V to publication VIII).

Bibliography

- [1] K. Bobzin, N. Bagcivan, P. Immich, C. Pinero, N. Goebbels, and A. Krämer, *Materialwissenschaft und Werkstofftechnik* **39**, 5 (2008).
- [2] P. M. Martin, *Handbook of Deposition Technologies for Films and Coatings: Science, Applications and Technology*. (Elsevier Science, 2009) p. 931.
- [3] B. Denkena and H. K. Tönshoff, *Spanen* (Springer Berlin Heidelberg, Berlin, Heidelberg, 2011).
- [4] K. Seshan and D. Schepis, *Handbook of thin film deposition* (Elsevier Science, 2018) p. 470.
- [5] H. Asanuma, P. Polcik, S. Kolozsvari, F. Klimashin, H. Riedl, and P. Mayrhofer, *Surface and Coatings Technology* **326**, 165 (2017).
- [6] H. Asanuma, F. Klimashin, P. Polcik, S. Kolozsvári, H. Riedl, and P. Mayrhofer, *Thin Solid Films* (2019).
- [7] H. Asanuma, F. Klimashin, P. Polcik, S. Kolozsvari, H. Riedl, and P. Mayrhofer, *Vacuum* **166**, 231 (2019).
- [8] R. Hollerweger, H. Riedl, J. Paulitsch, M. Arndt, R. Rachbauer, P. Polcik, S. Primig, and P. Mayrhofer, *Surface and Coatings Technology* **257**, 78 (2014).
- [9] P. E. Hovsepian, A. Ehiasarian, Y. Purandare, P. Mayr, K. Abstoss, M. Mosquera Feijoo, W. Schulz, A. Kranzmann, M. Lasanta, and J. Trujillo, *Journal of Alloys and Compounds* **746**, 583 (2018).
- [10] S. Wurster, C. Motz, and R. Pippan, *Philosophical Magazine* **92**, 1803 (2012).
- [11] K. Matoy, H. Schönherr, T. Detzel, T. Schöberl, R. Pippan, C. Motz, and G. Dehm, *Thin Solid Films* **518**, 247 (2009).
- [12] M. Alfreider, D. Kozic, O. Kolednik, and D. Kiener, *Materials and Design* **148**, 177 (2018).

- [13] G. Dehm, B. N. Jaya, R. Raghavan, and C. Kirchlechner, *Acta Materialia* **142**, 248 (2018).
- [14] G. Gottstein, *Physical Foundations of Materials Science* (Springer Berlin Heidelberg, Berlin, Heidelberg, 2004).
- [15] W. Seidl, M. Bartosik, S. Kolozsvári, H. Bolvardi, and P. Mayrhofer, *Surface and Coatings Technology* **347**, 92 (2018).
- [16] R. Hollerweger, H. Riedl, M. Arndt, S. Kolozsvari, S. Primig, and P. Mayrhofer, *Thin Solid Films* (2019).
- [17] H. Asanuma, F. Klimashin, P. Polcik, S. Kolozsvári, H. Riedl, and P. Mayrhofer, *Surface and Coatings Technology* **372**, 26 (2019).
- [18] A. A. Griffith, *Philosophical Transactions of the Royal Society A: Mathematical, Physical and Engineering Sciences* **221**, 163 (1921).
- [19] G. R. Irwin, *J. Appl. Mech.* (1957).
- [20] M. Liu, Y. Gan, D. A. Hanaor, B. Liu, and C. Chen, *Engineering Fracture Mechanics* **149**, 134 (2015).
- [21] T. L. Anderson, *Fracture Mechanics* (CRC Press, 2005).
- [22] W. D. Callister, *Materials science and engineering: An introduction* (John Wiley & Sons, 2003) p. 820.
- [23] E. Orowan, *Rep. Prog. Phys.* **12**, 185 (1949).
- [24] A. Anders, *Thin Solid Films* **502**, 22 (2006).
- [25] C. Koller, *Thermal Stability and Oxidation Resistance of Ti-Al-N / Ta-Al-N Multilayers*, Master thesis, Montanuniversität Leoben (2012).
- [26] S. Dushman, *Reviews of Modern Physics* **2**, 381 (1930).
- [27] B. Jüttner, *Physica B+C* **114**, 255 (1982).
- [28] B. Jüttner, in *High Voltage Vacuum Insulation* (Academic Press, 1995) pp. 515–561.
- [29] G. Mesyats, *Journal of Nuclear Materials* **128-129**, 618 (1984).
- [30] A. Anders, *Cathodic arcs: From fractal spots to energetic condensation* (Springer, 2008) p. 540.

- [31] S. Harris, E. Doyle, Y.-C. Wong, P. Munroe, J. Cairney, and J. Long, *Surface and Coatings Technology* **183**, 283 (2004).
- [32] P. Sigmund, *Physical Review* **184**, 383 (1969).
- [33] IAP/TU Wien, “A Simple Sputter Yield Calculator, URL: <https://www.iap.tuwien.ac.at/www/surface/sputteryield>, accessed on 2019-06-06,” .
- [34] H. A. Lorentz, in *Collected Papers* (Springer Netherlands, Dordrecht, 1937) pp. 1–138.
- [35] M. Ohring, *Materials science of thin films* (Elsevier Science, 2001) p. 794.
- [36] A. A. Fridman and L. A. Kennedy, *Plasma Physics and Engineering*. (CRC Press, 2011) p. 912.
- [37] P. Mayrhofer, *Materials Science Aspects of Nanocrystalline PVD Hard Coatings*, Ph.D. thesis, Montanuniversität Leoben (2001).
- [38] G. Betz and K. Wien, *International Journal of Mass Spectrometry and Ion Processes* **140**, 1 (1994).
- [39] I. Petrov, A. Hall, A. B. Mei, N. Nedfors, I. Zhirkov, J. Rosen, A. Reed, B. Howe, G. Greczynski, J. Birch, L. Hultman, and J. E. Greene, *Journal of Vacuum Science & Technology A: Vacuum, Surfaces, and Films* **35**, 050601 (2017).
- [40] P. Mayrhofer, *Script to the lecture Surface Technology* (Vienna, 2017).
- [41] P. H. Mayrhofer, C. Mitterer, L. Hultman, and H. Clemens, *Progress in Materials Science* **51**, 1032 (2006).
- [42] B. Movchan and A. Demchishin, *Fiz. Metal. Metalloved.* **28**, 653 (1969).
- [43] J. A. Thornton, *Journal of Vacuum Science and Technology* **12**, 830 (1975).
- [44] R. Messier, A. P. Giri, and R. A. Roy, *Journal of Vacuum Science & Technology A: Vacuum, Surfaces, and Films* **2**, 500 (1984).
- [45] A. Anders, *Thin Solid Films* **518**, 4087 (2010).
- [46] B. Lawn and R. Wilshaw, *Journal of Materials Science* **10**, 1049 (1975).
- [47] G. Anstis, P. Chantikul, B. Lawn, and D. Marshall, *Journal of the American Ceramic Society* **64**, 533 (1981).
- [48] N. Cuadrado, J. Seuba, D. Casellas, M. Anglada, and E. Jiménez-Piqué, *Journal of the European Ceramic Society* **35**, 2949 (2015).

- [49] J. Ast, M. Ghidelli, K. Durst, M. Göken, M. Sebastiani, and A. Korsunsky, *Materials & Design* **173**, 107762 (2019).
- [50] S. Zhang and X. Zhang, *Thin Solid Films* **520**, 2375 (2012).
- [51] J. Chen, *Journal of Physics D: Applied Physics* **45**, 203001 (2012).
- [52] M. Sebastiani, K. E. Johanns, E. G. Herbert, F. Carassiti, and G. M. Pharr, *Philosophical Magazine* **95**, 1928 (2015).
- [53] M. Ghidelli, M. Sebastiani, K. E. Johanns, and G. M. Pharr, *Journal of the American Ceramic Society* **100**, 5731 (2017).
- [54] B. N. Jaya, C. Kirchlechner, and G. Dehm, *Journal of Materials Research* **30**, 686 (2015).
- [55] W. Luo, C. Kirchlechner, X. Fang, S. Brinckmann, G. Dehm, and F. Stein, *Materials & Design* **145**, 116 (2018).
- [56] R. Soler, S. Gleich, C. Kirchlechner, C. Scheu, J. Schneider, and G. Dehm, *Materials & Design* **154**, 20 (2018).
- [57] S. Brinckmann, C. Kirchlechner, and G. Dehm, *Scripta Materialia* **127**, 76 (2017).
- [58] S. Brinckmann, K. Matoy, C. Kirchlechner, and G. Dehm, *Acta Materialia* **136**, 281 (2017).
- [59] NJ Petch, *Journal of the Iron and Steel* **174**, 25 (1953).
- [60] E. O. Hall, *Proceedings of the Physical Society. Section B* **64**, 747 (1951).
- [61] Oruç Süleyman Fıçıcı, *Thermische Eigenschaften von Ti-B-N Hartstoffschichten*, Bachelor thesis, Technische Universität Wien (2018).
- [62] P. Scherrer, *Nachrichten von der Gesellschaft der Wissenschaften zu Göttingen, Mathematisch-Physikalische Klasse*, 98 (1918).
- [63] J. Musil, P. Zeman, H. Hrubý, and P. H. Mayrhofer, *Surface and Coatings Technology* **120**, 179 (1999).
- [64] T. H. Courtney, *Mechanical behavior of materials* (McGraw Hill, 2000) p. 733.
- [65] P. M. Morse, *Physical Review* **34**, 57 (1929).
- [66] G. Mie, *Annalen der Physik* **316**, 657 (1903).

- [67] H. Kindlund, D. G. Sangiovanni, L. Martínez-de Olcoz, J. Lu, J. Jensen, J. Birch, I. Petrov, J. E. Greene, V. Chirita, and L. Hultman, *APL Materials* **1**, 042104 (2013).
- [68] D. Sangiovanni, *Acta Materialia* **151**, 11 (2018).
- [69] D. G. Sangiovanni, V. Chirita, and L. Hultman, *Physical Review B* **81**, 104107 (2010).
- [70] J. G. Lee, *Computational materials science: An introduction* (Taylor & Francis, 2011) p. 280.

Contributions to the field

Besides the studies on the Ti-B-N system, the results of the work done within this thesis is presented in publications accepted from international peer-reviewed journals, or in final preparation for submission. In chapters 4.1. and 4.2. a brief summary of this contributions is provided, further publications are listed with full bibliographic details in chapter 4.3.

The supervision done within this thesis is listed in chapter 4.4, and contributions (talks and poster presentations) to international conferences are presented in chapter 4.5.

4.1 First Author Publications

Publication I

R. Hahn, M. Bartosik, R. Soler, C. Kirchlechner, G. Dehm, and P.H. Mayrhofer
Superlattice effect for enhanced fracture toughness of hard coatings
Scr. Mater. 124 (2016). doi:10.1016/j.scriptamat.2016.06.030.

TiN and CrN hard coatings are well described material systems, successfully applied as wear resistant top layer in several industrial applications. The superlattice coating – a multilayer with coherent growth and a bilayer period Λ in the range of some nm – based on these two constituents shows an effect of the bilayer period on the hardness. However, the fracture toughness of such systems had yet to be quantified. In this publication we show that unbalanced magnetron sputtered TiN-CrN superlattice coatings exhibit a peak in fracture toughness (measured with single cantilever bending tests) similar to the well-known hardness peak. Importantly this peak is in the same bilayer period range (~ 6 nm) as the hardness peak, the measured values are $K_{IC} = 2.0 \pm 0.2 \text{ MPa}\sqrt{m}$ and $H = 24 \pm 1 \text{ GPa}$. Hence, we added an important detail of a mechanism now known for increasing both, hardness and toughness. The reason for the increase in hardness is covered by the hindrance of dislocation motion within and across the interfaces and draw upon in difference in shear

moduli ΔG of its constituents, our micromechanical experiments however, show little-to-non plasticity. Thus, an intrinsic bilayer period dependent property is responsible for the fracture toughness enhancement which has yet to be figured out. Besides the mechanical properties, we complemented our study by describing the microstructure of our coatings using x-ray diffraction, x-ray reflectivity, and high-resolution transmission electron microscopy (HRTEM).

Publication II

R. Hahn, M. Bartosik, M. Arndt, P. Polcik, and P.H. Mayrhofer

Annealing effect on the fracture toughness of CrN/TiN superlattices

Int. J. Refract. Met. Hard Mater. (2017). doi:10.1016/j.ijrmhm.2017.11.008.

The behavior of hard coatings at elevated temperatures is of great importance as such coatings are usually applied at high temperatures. Following the findings in publication I for TiN-CrN superlattice coatings, we were therefore interested in the high-temperature performance of these coatings. A series of annealing between 600 °C and 800 °C was performed for our superlattices with $\Lambda = 9.0$ nm and $\Lambda = 18.0$ nm (deposited on Al_2O_3) in vacuum (to measure solely the material behavior instead of a combination due to oxidation) and after that analyzed. Again, we performed micromechanical tests to quantify K_{IC} , different to our previous study we did not etch the substrate away, instead we milled pockets using a FIB. The main findings of this study were a – expected – decrease in H with annealing temperature, as well as a differing behavior of K_{IC} . We attribute the loss in hardness to a combination of recovery effects and interdiffusion between the layers reducing the superlattice effect on the hardness. The fracture toughness of the sample with 9.0 nm bilayer period follows the hardness, and is reduced from 2.3 ± 0.15 to $1.8 \pm 0.2 \text{ MPa}\sqrt{m}$. The other investigated sample shows an unexpected increase in K_{IC} from 1.7 ± 0.15 to $2.2 \pm 0.1 \text{ MPa}\sqrt{m}$ at 700 °C, leading to the conclusion that hardness and fracture toughness can show a different dependence on annealing treatments.

Publication III

R. Hahn, A. Kirnbauer, M. Bartosik, S. Kolozsvári, and P.H. Mayrhofer

Toughness of Si alloyed high-entropy nitride coatings

Mater. Lett. 251 (2019) 238–240. doi:10.1016/j.matlet.2019.05.074.

In this contribution we quantified, for the first time, the inherent fracture properties of an emerging class of coating materials: high entropy nitrides (HEN). Our (Al,Ta,Ti,V,Zr)N thin film exhibits a hardness of 30.7 ± 1.5 GPa and a fracture toughness of $2.4 \pm 0.1 \text{ MPa}\sqrt{m}$. Typically, the addition of the unsolvable Si to a nitride coating leads to the formation of a nanocrystalline structure which increases the hardness and toughness (publication VII) of a material. Though, we did not observe this effect on high entropy nitrides, although

the coating shows a nanocrystalline fracture cross section. Instead we observed similar H and K_{IC} values (29.2 ± 0.8 GPa and 2.3 ± 0.1 MPa \sqrt{m} respectively) as in the coating without silicon. Yet, we noticed a significant difference in the elastic response: The Young's modulus is reduced by ~ 100 GPa from 433 ± 23 GPa to 326 ± 6 GPa and consequently, the elastic strain to failure is increased by 33%. This is of significance, as the elastic deformability of a hard coating also determines its damage tolerance. This study further shows that the addition of Si – considering the decreased Young's modulus, the essentially constant K_{IC} , and the relation $K_{IC} \propto \sqrt{G \cdot E}$ – provides mechanisms to increase the dissipated energy during fracture.

Publication IV

R. Hahn, V. Moraes, A. Limbeck, P. Polcik, P.H. Mayrhofer, and H. Eychner
Electron-configuration stabilized (W,Al)B₂ solid solutions
Acta Mater. (2019). doi:10.1016/j.actamat.2019.05.056.

Transition metal diborides (TMBs) are – like high entropy materials – an emerging class of thin film- and bulk materials. In recent years these systems attracted attention from industry, as well as from academic research groups. These systems mainly crystallize in two different hexagonal structures: the α -type (space group #191) and the ω -type (space group #194). Due to a strong covalent bonding present in the hexagonal boron planes in both structures, they achieve excellent mechanical properties. However, hardness values over 45 GPa and indentation moduli up to 650 GPa were reported for the α -modification of TMBs. Here especially the α -structure of WB₂ is of great interest due to its balanced properties (high hardness and high fracture toughness, see publication VIII). However, a drawback of this coating is their relatively poor oxidation resistance. A well-known concept for increasing the oxidation resistance is alloying with aluminum, silicon, and zirconium. All of these elements form a dense oxide scale prohibiting further oxidation. Hence, using an ab initio calculation approach, we calculated the energy of formation, crystal structures, and stabilization limits for Al-alloyed W_{1-x}Al_xB₂ coatings and supplemented these findings with an experimental study. We found hardness values reaching 42 ± 2 GPa and an indentation modulus of 593 ± 12 GPa for pure WB₂, decreasing with increasing Al content, where the maximum content was ~ 20 at% Al to obtain crystalline films. This coating also showed an indication of spinodal decomposition upon annealing at 1000 °C in He atmosphere. The driving force for this decomposition is confirmed by our ab initio calculations which furthermore reveal vacancies as major cause for the experimentally received α -WB₂ and the impeded formation of binary AlB₂ and Al-rich W_{1-x}Al_xB₂.

Publication V

R. Hahn, N. Koutná, T. Wójcik, A. Davydok, D. Holec, M. Bartosik, and P. H. Mayrhofer
Influence of the Superlattice Effect on the Mechanical Properties of the MoN-TaN system: a computational and experimental approach

Manuscript in final preparation.

MoN and TaN are so-called late transition metal nitrides; thus, their valence electron concentration is comparatively high. This indicates an increased ductility, which was confirmed by our DFT studies using calculated ductility criteria (Pugh criterion: $G/B > 0.571$, Frantsevich criterion: $\nu > 0.26$, and Pettifor criterion: $c_{12}-c_{44} > 0$). A preceding DFT study (see chapter 4.3) furthermore revealed the formation of a tetragonal distorted ζ -phase for TaN in a superlattice structure, whereas MoN is present in its most stable form, MoN_{0.5}. These two constituents have a difference in lattice constants of $\Delta a \sim 0.23 \text{ \AA}$, a relatively large value, plus a comparatively small difference in shear modulus of $\Delta G \sim 30 \text{ GPa}$. Although the small difference in shear modulus, we measured a peak in fracture toughness with a relative increase of 23% to $3.0 \text{ MPa}\sqrt{m}$, whereas the increase in hardness is within the experimental error. Hence, we argue that the difference in lattice constants is the dominating origin for the increase in fracture toughness of superlattice coatings. In addition, the resulting strain at the interface leads to different atomic binding length, thus to increased cleavage energies for superlattices. Within this study we also investigated the elastic constants of the superlattice system, performed high-resolution XRD studies, and synchrotron nanodiffraction experiments. These studies led to the conclusion that TaN is stabilized in the ζ -structure up to a layer thickness of $\sim 2.5 \text{ nm}$. Thicker layers then form a metal deficient Ta_{0.75}N phase. We complemented this paper with FEGSEM and HRTEM studies showing an uneventful microstructure for hard coatings, although importantly confirming the diffraction studies.

4.2 Thesis-Related Co-Author Publications

Besides the first author contributions described in chapter 4.1, micromechanical tests were performed on different hard coating materials. These papers deal with the fracture properties of following material systems:

- Publication VI: Here the industrial highly important Ti-Al-N system was investigated. We found a slight increase in fracture toughness with increasing annealing temperature, whereas TiN remains unchanged. Importantly, when measuring the apparent fracture toughness on the substrate – using indentation fracture – an increase after annealing is found.
- Publication VII: In this contribution we show an enhancement in K_{IC} of TiN by more

than 50% to $3.0 \text{ MPa}\sqrt{m}$ by alloying with up to 14 at.% Si. The peak was found for 8.5%, at the same time we observed also an improvement in hardness of $\sim 6 \text{ GPa}$.

- Publication VIII: In this article we present, for the first time, quantified fracture toughness values of transition metal diborides without any substrate influence. We predicted and measured a decrease in K_{IC} for Ta-alloyed WB_2 . A simultaneous hardness increase was observed, leading to the conclusion of successful (although reversed) toughening via increased ductility.
- Publication IX: Here we performed cube corner indentation on low-temperature deposited TiN-CrN superlattices and multilayer coating. These indents were then examined by cross sectional SEM micrographs exposed using FIB, and additional TEM studies of such indents. The SEM observations of the residual imprints reveal columnar glide as the main deformation mechanisms under the indenter tip, and crack deflection of circumferential cracks around the tip for bilayer period $< 37.5 \text{ nm}$.

4.3 Further Publications

Apart from the thesis-relevant assignments, following publications were co-authored:

- C.M. Koller, R. Hahn, J. Ramm, S. Kolozsvári, and P.H. Mayrhofer, *Microstructural modifications in powder-metallurgically produced $\text{Al}_{0.675}\text{Cr}_{0.275}\text{Fe}_{0.05}$ targets during cathodic arc evaporation*, J. Vac. Sci. Technol. A Vacuum, Surfaces Film. 34 (2016). doi:10.1116/1.4938407.
- C.M. Koller, R. Hahn, B. Widrig, J. Ramm, S. Kolozsvári, J. Paulitsch, and P.H. Mayrhofer, *Triggering the Phase Evolution Within $(\text{Al,Cr})_2\text{O}_3$ -based Coatings by Alloying and Microstructural Concepts*, BHM Berg- Und Hüttenmännische Monatshefte. 161 (2016) 325–329. doi:10.1007/s00501-016-0506-2.
- C.M. Koller, A. Kirnbauer, R. Hahn, B. Widrig, S. Kolozsvári, J. Ramm, and P.H. Mayrhofer, *Oxidation behavior of intermetallic Al-Cr and Al-Cr-Fe macroparticles*, J. Vac. Sci. Technol. A Vacuum, Surfaces, Film. 35 (2017) 061601. doi:10.1116/1.4986928.
- N. Koutná, R. Hahn, J. Zálešák, M. Friák, M. Bartosik, J. Keckes, M. Šob, P.H. Mayrhofer, and D. Holec, *Point-defect engineering of MoN/TaN superlattice films: A first-principles and experimental study*, ArXiv E-Prints. (2019) arXiv:1905.04155. Submitted for publication to Pure and Applied Chemistry.
- T. Glechner, R. Hahn, T. Wojcik, D. Holec, S. Kolozsvári, H. Zaid, S. Kodambaka, P.H. Mayrhofer, and H. Riedl, *Assessment of ductile character in superhard Ta-C-N thin films*, Submitted for publication to Acta Materialia.

- V. Nedelkovski, R. Hahn, P.H. Mayrhofer, A. Steiger-Thirsfeld, J. Bernardi, and P.J. Thurner, *Influence of experimental constraints on micromechanical assessment of hard tissues: a validation study in silicon*, Manuscript in final preparation.

4.4 Supervision

Bachelor Thesis

- *Einfluss von Bor auf die mechanischen Eigenschaften von TiN-Schichten*, Arnold Tymoszuk, finished in April 2018.
- *Thermische Eigenschaften von Ti-B-N Hartstoffschichten*, Oruç Süleyman Fıçıcı, finished in June 2018.

Master Thesis

- *Mechanische Eigenschaften von Übergitter-Strukturen*, Arnold Tymoszuk, ongoing work, started in September 2018

Co-Supervision of Foreign PhD Students on their Stay at TU Wien

- *Investigation of cracking mechanisms in hard multilayer ceramic coatings considering a layer-arrangement effect*, Ahmad Azizpour, from May 2018 until November 2018

4.5 International Conference Contributions

- 46th ICMCTF 2019
Fracture toughness enhancement in superlattice hard coatings
San Diego (USA), Oral presentation.
- 45th ICMCTF 2018
Effect of Boron on the Mechanical Properties, especially Fracture Toughness, of TiN
San Diego (USA), Oral presentation.
- MRS Fall Meeting 2017
Fracture toughness enhancement of epitaxially grown CrN/TiN superlattice thin films
Boston (USA), Oral presentation.
- Nanomechanical Testing in Materials Research and Development VI 2017
Annealing Effect on the Fracture Toughness of CrN/TiN Superlattice Systems
Dubrovnik (Croatia), Oral presentation.

- 19th Plansee Seminar 2017
Annealing effect on the fracture toughness of CrN/TiN superlattices
Reute (Austria), Oral presentation.
- 63rd Metallkunde Kolloquium 2017
X-ray nano-diffraction demonstrating microstructural evolution and formation limits of CrN/AlN superlattice thin films
Lech am Arlberg (Austria), Oral presentation.
- Stress Evolution in Thin Films and Coatings 2016
Superlattice Effect for Enhanced Fracture Toughness of Hard Coatings
Chicago (USA), Oral presentation.
- Future Possible Use of Neutron and Synchrotron Sources by the Austrian User Community 2016
X-Ray nano-diffraction pointing out formation limitations of c-AlN in nanolayered thin films
Graz (Austria), Poster presentation.

4.6 PhD Related Awards

- Graduate Student Award Silver Medalist at the 46th ICMCTF in San Diego (USA)

CHAPTER 5

Publications

Publication I



Superlattice effect for enhanced fracture toughness of hard coatings

R. Hahn, M. Bartosik, R. Soler, C. Kirchlechner, G. Dehm, and P. H. Mayrhofer



Contents lists available at ScienceDirect

Scripta Materialia

journal homepage: www.elsevier.com/locate/scriptamat

Regular Article

Superlattice effect for enhanced fracture toughness of hard coatings

R. Hahn ^{a,b,*}, M. Bartosik ^{a,b}, R. Soler ^c, C. Kirchlechner ^{c,d}, G. Dehm ^c, P.H. Mayrhofer ^{a,b}^a Institute of Materials Science and Technology, TU Wien, A-1060 Vienna, Austria^b Christian Doppler Laboratory for Application Oriented Coating Development at the Institute of Materials Science and Technology, TU Wien, A-1060 Vienna, Austria^c Max-Planck-Institut für Eisenforschung, Max-Planck-Straße 1, D-40237 Düsseldorf, Germany^d Department Material Physics, University of Leoben, A-8700 Leoben, Austria

ARTICLE INFO

Article history:

Received 9 May 2016

Received in revised form 23 June 2016

Accepted 24 June 2016

Available online xxxx

Keywords:

Fracture toughness

Superlattice toughness

Nanolayer

Hard coatings

Micromechanical testing

ABSTRACT

Coherently grown nanolayered TiN/CrN thin films exhibit a superlattice effect in fracture toughness, similar to the reported effect in indentation hardness. We found –by employing *in-situ* micromechanical cantilever bending tests on free-standing TiN/CrN superlattice films– that the fracture toughness increases with decreasing bilayer period (Λ), reaching a maximum at $\Lambda \sim 6$ nm. For ultrathin layers ($\Lambda \sim 2$ nm), the fracture toughness drops to the lowest value due to intermixing and loss of superlattice structure. Both, fracture toughness and hardness peak for similar bilayer periods of TiN/CrN superlattices.

© 2016 Elsevier Ltd. This is an open access article under the CC BY-NC-ND license (<http://creativecommons.org/licenses/by-nc-nd/4.0/>).

Hard coatings are used to protect engineering components, e.g. cutting tools, from severe external loads and harsh environments [1]. Thereby, the coatings should ideally be strong and tough. Multilayer coatings composed of two coherently stacked, alternating materials with a periodicity length in the nanometer range, referred to as superlattice films, have been reported to possess exceptional high hardness values exceeding that of their single layered constituents by some hundred percent. In the 1980s, Helmersson et al. [2] reported on a hardness enhancement of up to $\sim 250\%$ compared to single-layered materials for the single-crystalline coherent TiN/VN superlattice (SL) structure grown by physical vapor deposition on single crystalline MgO (100) substrates. Thereby, the peak hardness was found for a periodicity length of ~ 5 nm. Later, an hardness enhancement was observed for a row of other SL film systems grown on MgO (100), but also on (native oxide) of Si (100) and polycrystalline steel substrates [3].

Besides high hardness values, a sufficiently high fracture toughness is needed to ensure the integrity of bulk and coated engineering components. Unfortunately, these material properties are commonly mutually influential (especially for materials showing plastic behavior), as a high strength often implies a low fracture toughness and vice versa [4]. In the last decades various strategies have successfully shown how to break down this relationship, spanning from grain refinement toughening –based on the classical Hall-Petch relation used in a variety of steels

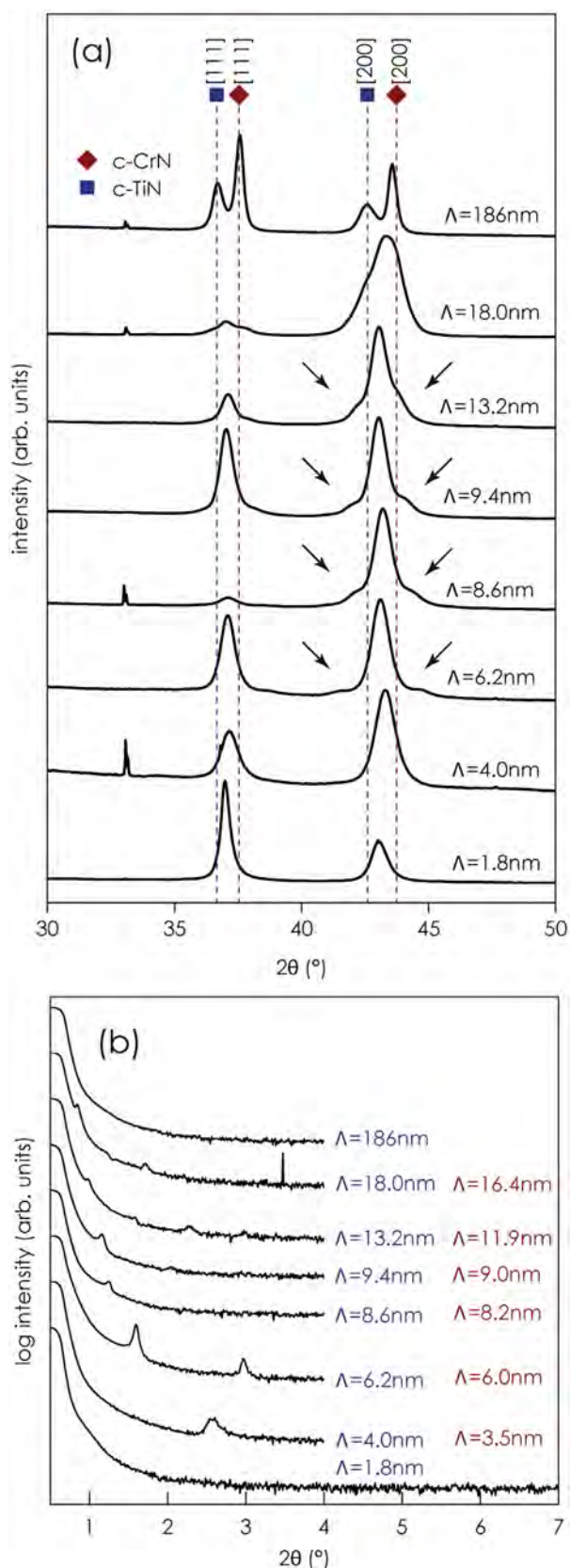
[5,6]– to recently found nanoscaled twinning mechanisms being operative in high-entropy alloys –enabling exceptional high fracture-resistance even at cryogenic temperatures [7]– and several other mechanisms presented in Ref. [4]. Strategies for enhancing the (fracture) toughness of ceramic coatings (see review by Zhang et al. [8]) include: incorporating a ductile phase; toughening through a nanocrystalline microstructure, composition, or structure grading; multilayer structuring; phase transformation toughening; or apparent toughening by implementation of compressive stresses, most of them being already effectively applied in industrial products. However, the exceptional effect of a superlattice structure on the fracture toughness has yet not been reported.

Here, we study the influence of the superlattice structure on the fracture toughness. Therefore, we have conducted micromechanical experiments on freestanding superlattice coatings with different bilayer periods (Λ). The isomorphous face-centered cubic (B1) TiN/CrN superlattice grown on Si (100) substrates served as a model system. The constituents TiN and CrN represent one of the most widely used nitrogen-based hard coating materials and their shear moduli (~ 180 GPa [9] and ~ 135 GPa [10], respectively) are significantly different, which promotes the superlattice effect [11].

TiN/CrN multilayer films with equal thick layers –bilayer periods ranging from ~ 2 to 200 nm, and total film thicknesses of ~ 2 μm – were synthesized by dc unbalanced reactive magnetron sputtering. All films were grown on Si (100) substrates ($7 \times 20 \times 0.38$ mm³) in an AJA International Orion 5 magnetron sputtering system equipped with one two-inch Cr and one three-inch Ti target (both from Plansee Composite Materials GmbH, 99.6 at.% purity). Prior to the deposition, the substrates

* Corresponding author at: Institute of Materials Science and Technology, TU Wien, A-1060 Vienna, Austria.

E-mail address: rainer.hahn@tuwien.ac.at (R. Hahn).



were ultrasonically cleaned in ethanol and acetone, for 5 min each. Subsequently, the substrates were mounted inside the deposition chamber (evacuated to a base pressure below 10^{-4} Pa), thermally cleaned at 500 °C for 20 min, and Ar-plasma etched (Ar pressure = 6 Pa) at the same temperature for 10 min. The deposition was carried out at 500 °C in an Ar/N₂ gas mixture with a flow ratio of 1/1 and a total pressure of 0.4 Pa. Both targets were dc powered using a target power density of 6.8 W/cm² for Ti and 7.6 W/cm² for Cr. To ensure a dense film morphology, a constant negative bias potential of -60 V was applied to the substrates. The alternating and equally thick TiN and CrN layers were deposited by using a computer controlled shutter system mounted in front of the Ti and Cr targets. Films with the following nominal bilayer periods (obtained by dividing the total film thickness with the number of TiN/CrN pairs) were synthesized: 1.8, 4.0, 6.2, 8.6, 9.4, 13.2, 18.0, and 186 nm. To highlight the superlattice effect itself, we intentionally used only a moderate bias potential of -60 V during the deposition of our polycrystalline TiN/CrN thin films, although Barshilia et al. [12], for instance, reported even higher peak hardnesses for TiN/CrN superlattice films when prepared with high bias potentials of -150 V.

X-ray diffraction (XRD) patterns from all coatings were collected in symmetric Bragg-Brentano configuration using Cu-K α radiation and are presented in Fig. 1(a). The XRD patterns show that the films grew in the face-centered cubic crystal structure. Cumulative diffraction peaks with peak positions laying in between TiN and CrN peaks (instead of two clearly differentiate peaks) reveal the presence of a superlattice structure with strained layers. Furthermore, positive and negative satellite peaks reflecting the SL structure (marked exemplarily with arrows in Fig. 1(a) in the vicinity of the 200 Bragg peak) emerge for the $\Lambda = 6.2$ nm multilayer film and become more apparent with increasing bilayer period. In the case of the multilayer film with the thickest bilayer period ($\Lambda = 186$ nm), two clearly separated Bragg peaks matching TiN and CrN lattice constants are observed, suggesting a largely independent growth of TiN and CrN layers with incoherent or semi-coherent interfaces, as expected for large bilayer periods. The native oxides on the Si (100) substrates lead to the formation of a polycrystalline structure within all our thin films.

In order to confirm the estimated nominal bilayer periods we conducted X-ray reflectivity (XRR) measurements, Fig. 1(b), and used a modified Bragg's-law approach to calculate Λ :

$$\sin^2(\theta) = \left(\frac{m * \lambda}{2 * \Lambda}\right)^2 + 2 * \delta, \quad (1)$$

where m denotes the order of the reflection, λ the wavelength of radiation (here Cu-K α) and δ the real part of the average refractive index (in our case $\delta \sim 1.6 * 10^{-5}$) [13]. The XRR obtained bilayer periods excellently fit to the nominal bilayer periods, see the listed values in Fig. 1b. The XRR patterns show no signs for a superlattice structure for our thin films with the largest and smallest nominal bilayer periods ($\Lambda = 186$ and 1.8 nm), hence, no XRR obtained bilayer periods could be calculated for these. This suggests that for our thin film with the smallest nominal bilayer period of 1.8 nm, the intermixing interface regions between TiN and CrN layers are too dominant to allow for the development of a superlattice structure. These results are further supported

Fig. 1. XRD (a) and XRR (b) scans of TiN/CrN superlattice films with different bilayer periods Λ . The arrows in (a) exemplarily mark satellite peaks in the vicinity of the 200 Bragg peak reflecting the SL structure. The bilayer periods quoted in the left column (blue) in (b) were calculated by dividing the total film thickness through the number of TiN/CrN pairs (obtained from the computer controlled deposition system), those in the right column (red) were calculated from the 2 θ peak-positions. The coatings with the thickness-obtained Λ of 1.8 nm and 186 nm show no signs of a superlattice structure. (For interpretation of the references to colour in this figure legend, the reader is referred to the web version of this article.)

by transmission electron microscopy (TEM) cross section images, Figs. 2(a) and (b). In contrast to our thin film with a nominal Λ of 13.2 nm (exhibiting a pronounced superlattice structure) no layered structure can be observed for the sample with a nominal Λ of 1.8 nm, explaining the missing XRR peak. The TEM samples were prepared by conventional grinding of a film-substrate lamella down to a thickness of $\sim 10 \mu\text{m}$ using a diamond abrasive. A GATAN Precise Ion Polishing System was used to further thin the sample down till electron transparency. The TEM-images were recorded using a FEI TECNAI F20 operating with an acceleration voltage of 200 kV.

To determine the fracture toughness of all TiN/CrN thin films, micromechanical single cantilever bending tests were performed on free-standing films. This approach allows to effectively eliminate potential sources of errors, like the influence of the substrate material and residual film stresses on the fracture toughness [14]. The Si substrates were locally dissolved by 90 min wet chemical etching in a 30 wt.% potassium hydroxide (KOH) solution heated to 60 °C. As a result, free-standing films ($\sim 20 \mu\text{m}$ broad and a few mm wide) were obtained. Cantilevers with dimensions of $\sim 2 \times 2 \times 14 \mu\text{m}^3$ were fabricated by Ga^+ focused ion beam (FIB) milling perpendicular to the film surface, using a FEI Quanta 200 3D DBFIB work station. A final milling current of 500 pA at an acceleration voltage of 30 kV was employed. The pre-notch was milled using 50 pA. A scanning electron microscope image (30° inclined from top view) of a pre-notched single cantilever specimen after FIB milling is depicted in Fig. 3(a).

The in-situ micromechanical experiments were performed in a JEOL scanning electron microscope (JEOL JSM 6430, JEOL Ltd., Akishima, Japan) equipped with an UNAT SEM-2 nanoindenter (ASMEC GmbH, Radeberg, Germany). A 2 μm spherical diamond tip was used for the experiments. The tests were carried out on a displacement-controlled mode, at a constant displacement rate of 5 nm/s. For each multilayer film system, 10 μm -beams were tested (with an average success rate of $\sim 76\%$). Representative load-deflection curves for the SL films with $\Lambda = 1.8, 6.2,$ and 18.0 nm are shown in Fig. 3(b). Note that deviations on loading stiffness arise for different cantilevers due to small variations on actual cross-sections and distances of applied load, l . Nonetheless, all

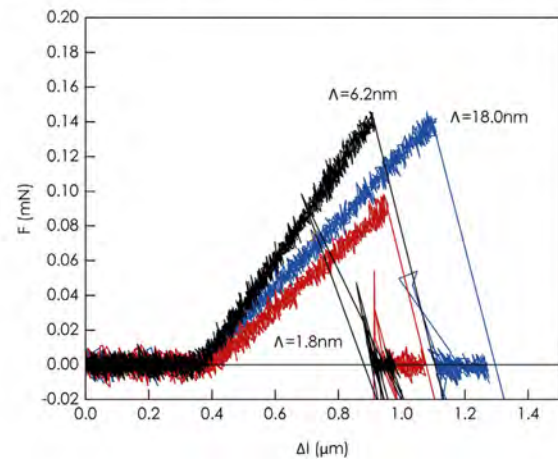
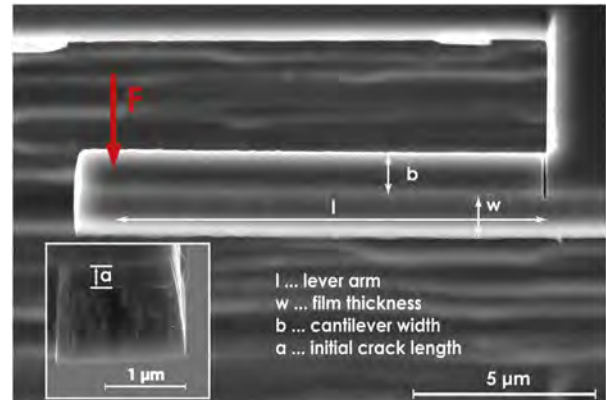


Fig. 3. (a) Scanning electron microscope image (30° inclined from top view) of a pre-notched single cantilever specimen before micromechanical testing. The insert is a post mortem SEM image of the fractured surface showing pre-notch depth a . (b) Representative bending stress-deflection curves recorded in the micromechanics single cantilever bending experiments from TiN/CrN superlattice films with bilayer periods of 1.8, 6.2 and 18.0 nm.

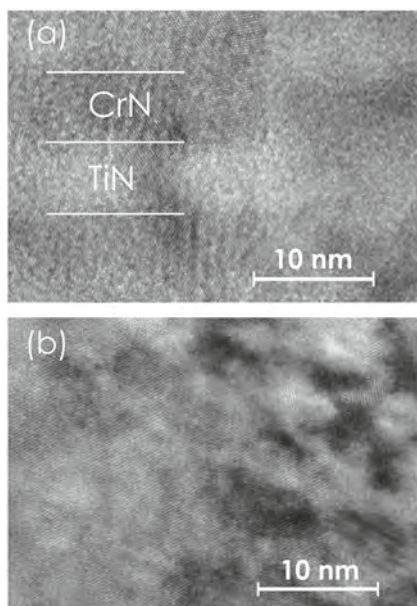


Fig. 2. HR-TEM images of the TiN/CrN superlattice films exhibiting bilayer periods of 13.2 (a) and 1.8 nm (b), respectively. While the nanolayered structure can be clearly seen for the large bilayer period sample (a) the interdiffusion-areas between TiN and CrN and loss of the layer structure becomes evident for the smallest bilayer period samples shown in (b).

SL structures present a perfect linear-elastic brittle fracture behavior without any signs of plasticity in the load-displacement response. Therefore, linear-elastic fracture mechanics was applied to quantify the fracture toughness K_{IC} :

$$K_{IC} = \frac{P_{max} \cdot l}{b \cdot w^{3/2}} \cdot f\left(\frac{a}{w}\right), \quad (2)$$

whereby the geometry factor $f\left(\frac{a}{w}\right)$ was taken as:

$$f\left(\frac{a}{w}\right) = 1.46 + 24.36 \cdot \left(\frac{a}{w}\right) - 47.21 \cdot \left(\frac{a}{w}\right)^2 + 75.18 \cdot \left(\frac{a}{w}\right)^3, \quad (3)$$

according to Matoy et al. [15]. P_{max} denotes the maximum force, l the lever arm, b the width of the cantilever, and w the film thickness (see Fig. 3(a)). The initial crack length, a , was determined from SEM micrographs of the post mortem fracture surface, as shown in an example in the insert of Fig. 3(a). The relatively flat fracture surface together with the absence of dimples or any other sign of significant plastic deformation, confirm the brittle fracture response of our thin films.

The derived fracture toughness (K_{IC}) vs. the bilayer period for all superlattices studied – as well as those of the thin films with a nominal Λ of ~ 186 and 1.8 nm – is presented in Fig. 4 showing a pronounced bilayer-period-dependent behavior. For large bilayer periods ($\Lambda \geq 13$ nm), K_{IC} remains relatively constant, at $\sim 1.65 \pm 0.1 \text{ MPa}\sqrt{\text{m}}$. For smaller

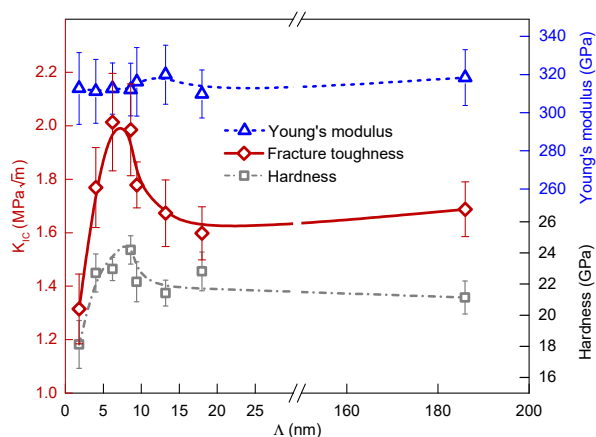


Fig. 4. Fracture toughness K_{IC} , indentation hardness H and moduli E of our TiN/CrN superlattice thin films as a function of their bilayer period Λ . The individual data points are connected to guide the eye.

bilayer periods, K_{IC} significantly raises, reaching a maximum value of $\sim 2.01 \pm 0.18 \text{ MPa}\sqrt{\text{m}}$ at $\Lambda \sim 6.2 \text{ nm}$. Further decreasing Λ drops dramatically K_{IC} to a minimum value of $\sim 1.31 \pm 0.13 \text{ MPa}\sqrt{\text{m}}$ at $\Lambda \sim 1.8 \text{ nm}$. Interestingly, a very similar dependency is observed for the hardness measurements, with H vs. Λ exhibiting a hardness peak with $24.2 \pm 0.9 \text{ GPa}$ at $\Lambda \sim 8.6 \text{ nm}$. The agreement between K_{IC} vs. Λ and H vs. Λ suggests that similar bilayer-period-dependent mechanisms could be responsible for both, the indentation hardness and the fracture toughness enhancement. The relatively constant indentation modulus as a function of the bilayer period, E vs. Λ , further proofs our K_{IC} vs. Λ curve by the coincidence with the H/E empirical criteria, often used to qualitatively rate materials for their toughness [16,17]. This simplified criterion predicts for brittle materials with similar E values, that a higher hardness would result in a higher energy absorbed until fracture.

The hardness enhancement due to the superlattice effect, described by the model after Chu and Barnett [18], is based on two mechanisms being operative during plastic deformation of a superlattice system. For small bilayer periods, the stresses required for dislocations to glide across layers with different shear moduli increase with increasing bilayer periods. The second mechanism describes the stress required to move preexisting dislocations within the layers, as well as the stress required to activate dislocation sources. The latter two required stresses, τ , decrease with increasing bilayer period, following a Hall-Petch-like relationship:

$$\tau \propto \Lambda^{-m}. \quad (4)$$

According to Chu and Barnett [18] the hardness enhancement in superlattices is, therefore, a plasticity driven phenomenon, and as such, is governed by dislocation mobility. In contrast, the herein presented fracture experiments show an absence of plastic deformation, hence, behave in a linear-elastic brittle manner. In this case the failure of the material is controlled by the average defect density and average maximum defect size. Thereby, rather than a bilayer-period-dependent dislocation-based mechanism, there must be an underlying bilayer-period-dependent property governing both SL effects. Some of these bilayer-period-dependent properties might be: coherency strains; misfit dislocation arrays at the interface; spatially oscillating elastic moduli influencing crack growth; average grain size and other defects confined into individual layers.

It is yet to be discovered which intrinsic SL property is responsible for the fracture toughness enhancement. But based on our results, a power-law relationship similar as for τ will hold between the fracture toughness and the bilayer period:

$$K_{IC} \propto \Lambda^{-m}, \quad (5)$$

with the exponent m depending on the type and interface constitution of the superlattice structure. The exponent m equals roughly 0.25 for our superlattice TiN/CrN coatings with $\Lambda \geq 6.2 \text{ nm}$.

The decline in H as well as K_{IC} when further reducing the bilayer period (below $\sim 6 \text{ nm}$) is also based on the decreasing SL effect, as with smaller bilayer periods the intermixing interface-regions between both layer types become dominant – see Figs. 1(b) and 2(b) and the missing signs for a superlattice structure with a nominal Λ of 1.8 nm .

Based on our results on polycrystalline TiN/CrN SL structures – deposited by unbalanced magnetron sputtering with different bilayer periods on Si (100) substrates – we can conclude, that a significant increase in fracture toughness is observed when SL structures are formed, similar to the well-known SL effect on hardness. However, further investigations into the toughening mechanisms are required in order to better understand this behavior and how it relates to the hardness SL effect. This new superlattice effect represents a significant improvement in mechanical properties of hard thin films, especially when both, hardness and fracture toughness, are simultaneously enhanced as it is the case here.

Acknowledgements

The financial support by the START Program (Y371) of the Austrian Science Fund (FWF) is gratefully acknowledged. SEM, TEM, and XRD investigations were carried out using facilities of the XRC and USTEM centers of TU Wien, Austria. The financial support by the Austrian Federal Ministry of Economy, Family and Youth and the National Foundation for Research, Technology and Development are gratefully acknowledged. The work of RS has been conducted within the project EPPL, co-founded by grants from Austria, Germany, The Netherlands, France, Italy, Portugal and the ENIAC Joint Undertaking.

References

- [1] P.H. Mayrhofer, A. Hörling, L. Karlsson, J. Sjöblom, T. Larsson, C. Mitterer, L. Hultman, *Appl. Phys. Lett.* 83 (2003) 2049.
- [2] U. Helmersson, S. Todorova, S.A. Barnett, J.-E. Sundgren, L.C. Markert, J.E. Greene, *J. Appl. Phys.* 62 (1987) 481.
- [3] M. Stueber, H. Holleck, H. Leiste, K. Seemann, S. Ulrich, C. Ziebert, *J. Alloys Compd.* 483 (2009) 321.
- [4] R.O. Ritchie, *Nat. Mater.* 10 (2011) 817.
- [5] J.W. Morris, *The Influence of Grain Size on the Mechanical Properties of Steel*, Lawrence Berkeley National Laboratory, 2001.
- [6] M. Calcagnotto, D. Ponge, D. Raabe, *Mat. Sci. Eng. A* 527 (2010) 7832.
- [7] B. Gludovatz, A. Hohenwarter, D. Catoor, E.H. Chang, E.P. George, R.O. Ritchie, *Science* 345 (2014) 1153.
- [8] S. Zhang, D. Sun, Y. Fu, H. Du, *Surf. Coat. Technol.* 198 (2005) 2.
- [9] D. Holec, M. Friák, J. Neugebauer, P.H. Mayrhofer, *Phys. Rev. B* 85 (2012) 064101.
- [10] L. Zhou, D. Holec, P.H. Mayrhofer, *J. Appl. Phys.* 113 (2013) 043511.
- [11] M. Shinn, S.A. Barnett, *Appl. Phys. Lett.* 64 (1994) 61.
- [12] H.C. Barshilia, A. Jain, K.S. Rajam, *Vacuum* 72 (2004) 241.
- [13] P.C. Yashar, W.D. Sproul, *Vacuum* 55 (1999) 179.
- [14] B.N. Jaya, C. Kirchlechner, G. Dehm, *J. Mater. Res.* 30 (2015) 686.
- [15] K. Matoy, H. Schönherr, T. Detzel, T. Schöberl, R. Pippan, C. Motz, G. Dehm, *Thin Solid Films* 518 (2009) 247.
- [16] B.R. Lawn, A.G. Evans, D.B. Marshall, *J. Am. Ceram. Soc.* 63 (1980) 574.
- [17] A.G. Evans, E.A. Charles, *J. Am. Ceram. Soc.* 59 (1976) 371.
- [18] X. Chu, S.A. Barnett, *J. Appl. Phys.* 77 (1995) 4403.

Publication II



Annealing effect on the fracture toughness of CrN/TiN superlattices

R. Hahn, M. Bartosik, M. Arndt, P. Polcik and P. H. Mayrhofer

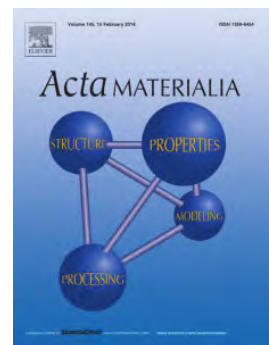
Publication III



Toughness of Si alloyed high-entropy nitride coatings

R. Hahn, A. Kirnbauer, M. Bartosik, S. Kolozsvári and P. H. Mayrhofer

Publication IV



Electron-configuration stabilized (W,Al)B₂ solid solution

R. Hahn, V. Moraes, A. Limbeck, P. Polcik, P. H. Mayrhofer, and H. Euchner



Contents lists available at ScienceDirect

Acta Materialia

journal homepage: www.elsevier.com/locate/actamat

Full length article

Electron-configuration stabilized (W,Al)B₂ solid solutionsRainer Hahn^{a,*}, Vincent Moraes^a, Andreas Limbeck^b, Peter Polcik^c, Paul H. Mayrhofer^a, Holger Euchner^{a,d}^a Institute of Materials Science and Technology, TU Wien, 1060, Vienna, Austria^b Institute of Chemical Technologies and Analytics, TU Wien, 1060, Vienna, Austria^c Plansee Composite Materials GmbH, 86983, Lechbruck am See, Germany^d Helmholtz Institute for Electrochemical Energy Storage, 89081, Ulm, Germany

ARTICLE INFO

Article history:

Received 1 March 2019

Received in revised form

16 May 2019

Accepted 26 May 2019

Available online 29 May 2019

Keywords:

Thin films

Borides

Sputtering

Vacancies

Density functional theory

ABSTRACT

By combining experimental and theoretical methods, we have conducted a detailed study of the ternary diboride system (W_{1-x}Al_x)_{1-y}B_{2(1-z)}. Tungsten rich solid solutions of (W_{1-x}Al_x)_{1-y}B_{2(1-z)} were synthesized by physical vapor deposition and subsequently investigated for structure, mechanical properties and thermal stability. All crystalline films show hardness values above 35 GPa, while the highest thermal stability was found for low Al contents. In this context, the impact of point defects on the stabilization of the AlB₂ structure type is investigated, by means of ab initio methods. Most notably, we are able to show that vacancies on the boron sublattice are detrimental for the formation of Al-rich (W_{1-x}Al_x)_{1-y}B_{2(1-z)}, thus providing an explanation why only tungsten rich phases are crystalline.

© 2019 Acta Materialia Inc. Published by Elsevier Ltd. This is an open access article under the CC BY-NC-ND license (<http://creativecommons.org/licenses/by-nc-nd/4.0/>).

1. Introduction

Nowadays the increasing interest in sustainability also results in a growing industrial demand for protective coatings with superior mechanical properties such as high hardness, good elastic properties, and improved thermal stability. As a consequence, the search for improved physical properties leads to the exploration of new material systems. Despite the fact that transition metal (TM) based nitrides are successfully applied in automotive or aerospace industries, the quest for improved functional materials is an ongoing challenge [1–3].

One of the peculiarities of vapor phase deposition techniques is the fact that they allow the growth of supersaturated non-equilibrium phases like cubic Ti_{1-x}Al_xN (NaCl-prototype, Fm $\bar{3}$ m, space group 225). Here, the supersaturation of the cubic TiN phase essentially starts with small aluminum contents [4] leading to Ti_{1-x}Al_xN solid solutions. A further increase of the Al fraction causes a further supersaturation of the cubic phase, which is found to result in age hardening effects at elevated temperatures. The origin of this

age hardening is found in the spinodal decomposition of cubic Ti_{1-x}Al_xN, which goes along with the formation of TiN- and AlN-rich cubic domains [5–8]. A degradation of the mechanical properties may only occur under further annealing when the metastable cubic AlN transforms into the thermodynamically stable wurtzite phase. A major retarding force for this phase transformation arises from the associated huge volume increase of almost 30% [7]. However, the significant volume change going along with this cubic to wurtzite transition may trigger toughening effects for controlled AlN phase fractions [9–11]. Consequently, the exceptional properties of Ti_{1-x}Al_xN can be attributed to the interplay and competition of the two boundary phases—cubic TiN and wurtzite AlN—which prefer to crystallize in different structure types.

This well-known concept, being responsible for the unique properties of Ti_{1-x}Al_xN and its derivatives, has lately been evoked as design principle for ternary borides, opening access to this new class of functional materials with various exceptional properties such as improved mechanical properties and enhanced thermal stability [12–17]. Despite the large progress that has been achieved with such concepts for ternary and even quaternary TM nitrides, the field of multinary borides is still largely unexplored and also lacks fundamental understanding.

Many diborides, comprising the technologically relevant TiB₂ phase [18,19], have been observed to crystallize in the so-called α -

* Corresponding author. Institute of Materials Science and Technology, TU Wien, Getreidemarkt 9/E308, A-1060, Vienna, Austria.

E-mail address: rainer.hahn@tuwien.ac.at (R. Hahn).

<https://doi.org/10.1016/j.actamat.2019.05.056>

1359-6454/© 2019 Acta Materialia Inc. Published by Elsevier Ltd. This is an open access article under the CC BY-NC-ND license (<http://creativecommons.org/licenses/by-nc-nd/4.0/>).

type structure [20], with a three atom unit cell of space group 191 (AlB_2 -prototype, $P6/mmm$) [21]. This structure type can be illustrated as a stacking of boron planes (the boron atoms form covalently bonded hexagons) separated by hexagonal metal planes as given in Fig. 1. The boron atoms sit in every vertex formed by three neighboring metal atoms (or in other words, the metal atoms are always in the center of a hexagon formed by the boron atoms). Apart from the prevailing α -type modification, other binary boride phases are known to adopt slightly different crystal structures. WB_2 is observed to crystallize in at least two different modifications [22,23]. Physical vapor deposited WB_2 thin films have been reported to crystallize in the α -type [24,25] structure, whereas bulk materials prefer the so-called ω modification, also known as W_2B_{5-z} -prototype [23]. The ω -phase is closely related to the AlB_2 -prototype, however, it consists of alternating flat and puckered boron layers. Still the boron atoms form covalently bonded hexagons (either flat or puckered) and the metal atoms form flat hexagonal planes. In Fig. 1 it is also apparent that the position (“stacking” on the metal sublattice) of the hexagonal metal-planes changes due to the puckered boron plane (i.e. from the “A” site to the “B” site and then back to again to the “A” site with the next puckered plane – using the well-known notification of AB stacking of densely packed layer in hexagonal close packed structures). As a consequence of the alternating layers an increased unit cell, comprising twelve atoms and adapting space group 194 ($P6_3/mmc$), is necessary to describe the ω -modification, as presented in Fig. 1.

Here, $(W_{1-x}Al_x)_{1-y}B_{2(1-z)}$ thin films with varying Al metal fractions x up to 50.1 at% on the metal sublattice have been deposited using physical vapor deposition (PVD). The obtained films reveal a high hardness, with the maximum value reaching almost 42 GPa for the case of WB_{2-z} . Furthermore, high thermal stability was observed with the films remaining stable after 30 min of annealing at 1000 °C. Decomposition and stabilization of α - $(W_{1-x}Al_x)_{1-y}B_{2(1-z)}$ is investigated by ab initio methods, once more pointing out the importance of point defects for the phase evolution of PVD deposited materials [13,26,27] and most strikingly giving an explanation for the fact that it is extremely difficult to grow Al-rich ternary boride thin films. In fact, a detailed literature review showed that there is no report about a crystalline AlB_2 thin film in the as deposited state. Nevertheless, the addition of Al to WB_2 will promote their self-passivating effects, as observed for Al alloying in ReB_2 [28].

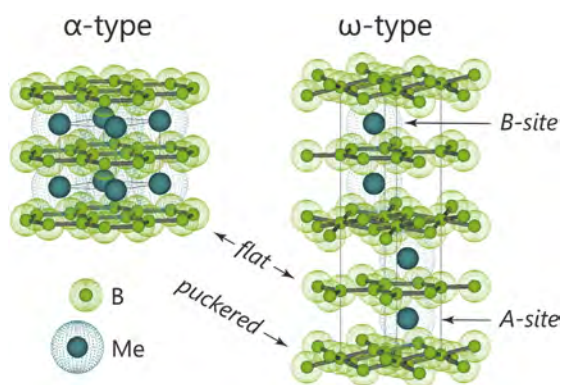


Fig. 1. Structure of the α - AlB_2 and ω - W_2B_{5-z} prototypes with the corresponding layer sequence.

2. Experimental and computational methods

A lab-scale magnetron sputtering system (AJA Orion 5) was used to deposit ternary $(W_{1-x}Al_x)_{1-y}B_{2(1-z)}$ films with varying Al content (the base pressure was below 0.1 mPa). Two diboride targets, namely a 2-inch W_2B_{5-z} and a 2-inch AlB_2 target (Plansee Composite Materials GmbH), were operated by dc plasma generators with a power-controlled signal. The maximum target power density was set to $7.4 W \cdot cm^{-2}$ and accordingly reduced for chemical variations. In our setup, the magnetrons, in a dual confocal arrangement, face the rotating substrate holder, which is placed at a distance of 11 cm. After reaching a temperature of 500 °C, single crystalline Si (100-oriented) and sapphire substrates (1T02-oriented) were ion etched in Ar atmosphere (at a pressure of 6 Pa). During the depositions, the substrate temperature was kept constant at a temperature of 500 °C, while a working gas pressure (Ar) of 0.7 Pa was used and no bias voltage was applied (the floating potential is about $-20 V$). We had to reduce the working gas pressure to 0.4 Pa for obtaining close to stoichiometric WB_2 films, because with 0.7 Pa we ended up with a $WB_{1.4}$ film. A similar dependence of the B/metal ratio on the working gas pressure was reported for TiB_x [29]. The deposition time was 240 min resulting in 1.1–1.8 μm thin films, depending on the power density of the W_2B_{5-z} target and working gas pressure used (resulting in a typical deposition rate of $6 nm \cdot min^{-1}$). The high Al-containing thin film was deposited for 480 min to obtain a comparable thickness.

The elemental composition of the as-deposited thin films on Si substrates was determined by inductively coupled plasma atomic emission spectroscopy (ICP-AES), for dissolution samples were treated with a mixture of nitric acid and hydrofluoric acid at elevated temperature [30]. This method was chosen since it allows for an accurate determination of the boron content, which is difficult to access by other characterization techniques. Structure and morphology of the as-deposited films on sapphire substrates were investigated by X-ray diffraction (XRD).

The thermal stability was investigated by comparing XRD measurements of the thin films in as-deposited state and after annealing (base pressure below 0.1 mPa) at 1000 °C for 30 min in He atmosphere (the heating rate was 20 K/min and the cooling rate by simply turning off the heater was $>50 K/min$ down to 500 °C). XRD measurements were conducted with a PANalytical XPert Pro MPD (θ - θ diffractometer) in Bragg Brentano geometry equipped with a CuK_{α} cathode (wave length $\lambda = 1.54 \text{ \AA}$, 45 kV, 40 mA).

Moreover, a FEI Quanta 250 scanning electron microscope equipped with a field emission gun (FEGSEM) was used to take cross section micrographs. The residual stresses of our thin films were determined using the Stoney-equation [31], after extracting the substrate curvature making use of a Nanovea PS50 chromatic confocal profilometer.

The mechanical properties of both, the as-deposited and the annealed coatings on sapphire substrates, were studied by nano-indentation, using an ultra-micro indentation system (UMIS). Loads within a range from 3 to 45 mN were applied with a Berkovich type indenter. Indents exceeding an indentation depth greater than 10% of the film thickness were excluded from the analysis to minimize the substrate interference. Hardness and indentation modulus were determined from the resulting load-displacement curves of the nanoindents using the standard approach after Oliver and Pharr [32], the errors noted are standard deviations.

The structural stability of α - and ω - $(W_{1-x}Al_x)_{1-y}B_{2(1-z)}$ with respect to stoichiometry and changing vacancy concentrations on the respective sublattice y and z was investigated by means of density functional theory (DFT). For this purpose the Vienna Ab Initio Simulation Package (VASP) [33,34], using the projector augmented wave method [35], was applied. Exchange and

correlation were accounted for by the generalized gradient approximation as introduced by Perdew and Wang [36]. To start with, supercells of the α - and the ω -modification of $(W_{1-x}Al_x)_{1-y}B_{2(1-z)}$ were constructed. For the smaller α -phase a $2 \times 2 \times 4$ supercell, containing 48 atoms, was selected, whereas in case of ω - $(W_{1-x}Al_x)_{1-y}B_{2(1-z)}$ a $2 \times 2 \times 1$ supercell with the same number of atoms was created. For the realization of solid solutions or random alloys with different stoichiometries the metal sublattices were populated by the respective Al/W ratios, by making use of the special quasirandom structure (SQS) approach [37]. The corresponding SQS structures were then constructed using the *at* package [38]. As a next step, atomic coordinates and lattice geometry of the obtained SQS configurations were optimized using the VASP code with an energy cutoff of 600 eV and a $8 \times 8 \times 4$ Γ -centered *k*-point mesh. The plane wave cutoff energy and the *k*-point resolution were chosen to ensure convergence and an accuracy of the calculation within a few meV/at. To introduce vacancies in the two structure types, the same approach was used by simply considering vacancies as additional alloying element in the SQS approach.

Schematics were produced using VESTA [39].

3. Results and discussion

Solid solutions of $(W_{1-x}Al_x)_{1-y}B_{2(1-z)}$ thin films have been prepared for various Al/W ratios, evidencing boron contents between 60 and 66%, thus being close to stoichiometric $(W_{1-x}Al_x)_{1-y}B_{2(1-z)}$ diborides (see Table 1).

Our XRD results highlight that only for Al metal fractions far below 50 at%, as-deposited crystalline films can be obtained (see Fig. 2). For Al metal fractions below 20% (*i.e.*, $x < 0.2$), we clearly see single phase solid solution of α - $(W_{1-x}Al_x)_{1-y}B_{2(1-z)}$ with the *c*-axis lattice parameters lying in between those of α -AlB₂ [40] and the experimentally observed one of α -WB₂ [22]. With increasing Al content, the positions of the (001) and (002) reflections shift to lower angles also confirming the incorporation of Al on the metal sublattice.

In agreement with these XRD investigations, the fracture cross sectional SEM micrographs, Fig. 3, show dense columnar growth morphologies for all thin films, except the highest Al-containing one. The cross section of the latter is more comparable to amorphous-like films. Additionally, an increased growth rate when reducing the deposition pressure is seen for the binary WB₂-based thin film.

Interestingly, our $(W_{1-x}Al_x)_{1-y}B_{2(1-z)}$ thin films exhibit significant changes in their XRD patterns upon 30-min annealing in He atmosphere at 1000 °C. The initially amorphous film with an Al fraction of 50.1 at% on the metal sublattice (absolute Al content of 17.3 at%) shows clearly crystalline XRD peaks at the position of ω -W₂B_{5-z} [41]. The (nano-) crystals of this coating are randomly

oriented (contrary to our other thin films) and they crystallize in the ω -type structure. For the film with 19.2 at% Al on the metal sublattice (absolute Al content of 6.9 at%), we observe a peak splitting of the (002) reflection upon annealing, which will also be discussed in the DFT section. This peak-splitting points to a spinodal decomposition of our W_{0.81}Al_{0.19}B₂ film towards a less defected Al-enriched W_{0.81- ξ} Al_{0.19+ ξ} B₂ (ξ indicates an increased Al content and a decreased W content) phase and a vacancy containing W-enriched WB_{2-z} phase. All other films show no signs of decomposition, but also a shift of the major XRD peaks (001) and (002) towards higher 2θ angles indicating recovery events (where structural defects rearrange towards lower energy sites, leading to a relief of microstrains).

The amorphous film—based on previous studies showing that sputtering of AlB₂ targets leads to amorphous films, we correlate this to the high Al content—shows a hardness of 24 GPa and an indentation modulus of 341 GPa. Both values are considerably lower than those of our crystalline materials. For the whole composition range, the hardness values of the crystalline α - $(W_{1-x}Al_x)_{1-y}B_{2(1-z)}$ thin films lie above 35 GPa, with the maximum of 42 ± 2 GPa for the binary α -WB₂ thin film (see Table 1). A noteworthy trend is the decreasing hardness with increasing Al content. This decrease in hardness of our $(W_{1-x}Al_x)_{1-y}B_{2(1-z)}$ thin films can be attributed to reduced bond strengths, mirrored also by decreasing indentation moduli. The residual stresses of our thin films are given in Table 1, we observe a decrease with increasing Al-content. The hardness of our thin films on Si substrates is ~1 GPa lower than on sapphire substrates, which can be attributed to lower residual compressive stresses on Si (~0.9 GPa, resulting from differences in the thermal expansion coefficients of the substrate materials). Also, the Young's modulus yields slightly lower values on Si than on sapphire substrates (however, well within the experimental error), which can again be attributed to the influence of residual stresses. The elastic recovery of our coatings varied between 61 and 63%, with a trend to higher recovery at lower Al contents, an exception was found for the initially amorphous film, where the recovery was only 53%. The mechanical properties of the annealed samples (1000 °C for 30 min) are listed in Table 1. Due to delamination of the binary α -WB_{2-z} thin film during annealing, no *H* and *E** could be obtained from this sample in the annealed state. Also $(W_{1-x}Al_x)_{1-y}B_{2(1-z)}$ thin films with Al metal fractions of 9.7 and 19.2 at% showed a significant crack pattern after annealing. However, the initially amorphous W_{0.50}Al_{0.50}B₂ thin film showed no crack formation during annealing, allowing to measure their mechanical properties to be *H* = 28 GPa and *E** = 407 GPa, hence, higher than in the as deposited state.

Ab initio calculations for $(W_{1-x}Al_x)_{1-y}B_{2(1-z)}$ predict the α -phase to become energetically more stable when the Al population on the metal sublattice exceeds ~50%, considering any types of vacancies

Table 1

Hardness *H*, indentation moduli *E**, elastic recovery ϵ_R , and residual stress σ_R of $(W_{1-x}Al_x)_{1-y}B_{2(1-z)}$ thin films depicted with respect to the sputtering power ratio, film thickness, and the chemical composition before and after annealing at 1000 °C in He atmosphere. All errors are standard deviations.

Sputtering-power ratio AlB ₂ /W ₂ B _{5-z} (-)	Film thickness <i>h</i> (μm)	Chemical composition (at%)					Mechanical properties (Sapphire substrate)					
		Al	W	B	$\frac{Al}{Al+W}$	As deposited				Annealed 1000 °C		
						<i>H</i> (GPa)	<i>E*</i> (GPa)	ϵ_R (%)	σ_R (GPa)	<i>H</i> (GPa)	<i>E*</i> (GPa)	
0.0(0/150)	1.8	0.0	35.0 ± 0.2	65.0 ± 0.2	0	42 ± 2	593 ± 12	63 ± 2	-1.5 ± 0.1	-	-	
0.5 (75/150)	1.5	0.9 ± 0.1	38.9 ± 0.2	60.2 ± 0.1	2.3	39 ± 1	550 ± 35	63 ± 2	-1.1 ± 0.1	37 ± 2	559 ± 15	
1.0 (150/150)	1.7	3.6 ± 0.2	34.0 ± 0.2	62.4 ± 0.1	9.7	38 ± 2	494 ± 31	63 ± 2	-0.7 ± 0.1	(35 ± 2)	†	
2.0 (150/75)	1.1	6.9 ± 0.1	29.1 ± 0.1	64.0 ± 0.1	19.2	36 ± 1	459 ± 29	62 ± 2	-0.6 ± 0.1	‡	‡	
4.0 (150/38)	1.8	17.3 ± 1.0	17.3 ± 0.3	65.4 ± 1.3	50.1	24 ± 1	341 ± 7	53 ± 2	-1.2 ± 0.1	28 ± 2	407 ± 24	

* delamination due to compressive stresses.

† little crack formation during annealing.

‡ crack formation during annealing.

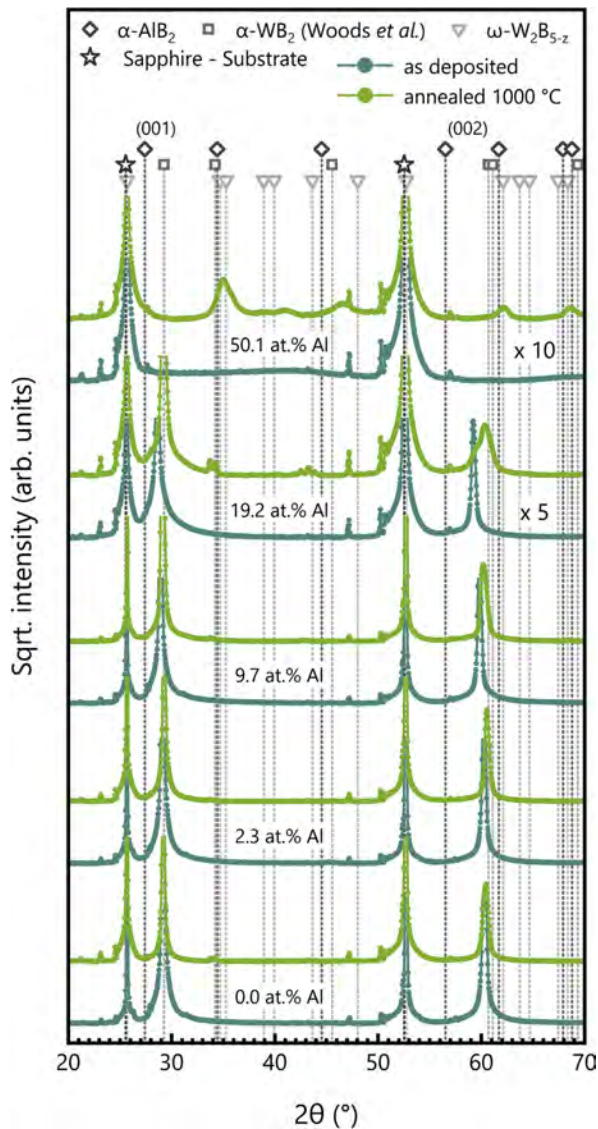


Fig. 2. XRD patterns of as deposited (blue) and annealed (green) $W_{1-x}Al_xB_2$ thin films. The symbols with vertical lines represent diffraction peak positions of α - AlB_2 , α - WB_2 and ω - W_2B_{5-z} . Substrate reflections are also indicated. The XRD patterns of the films containing an Al metal fraction of 19.2 and 50.1 are presented with 5 times respectively 10 times their intensity. (For interpretation of the references to color in this figure legend, the reader is referred to the Web version of this article.)

[12]. However, experimentally the α -phase is unambiguously observed for all our crystalline thin films. This is in good agreement with other recent PVD studies [13,24,25], which report that even the binary WB_2 crystallizes in the α modification. As PVD methods are known to promote the incorporation of point defects—such as vacancies—during crystal growth, detailed ab initio studies on the impact of point defects on crystal structure and energy of formation have been performed, suggesting that these are the major reasons for the stabilization of WB_2 (and also other diborides) in its metastable α -structure [13,42].

To study the consequences of an increased vacancy concentration on the phase stability of ternary $(W_{1-x}Al_x)_{1-y}B_{2(1-z)}$ we have

analyzed the energy of formation, E_f , of both, the α -type and the ω -type modification, for changing chemical compositions and concentrations of vacancies, following eqn. (1):

$$E_f = \frac{1}{\sum_i n_i} \left(E_{tot} - \sum_i n_i E_i \right) \quad (1)$$

here, E_{tot} and E_i gives the total energy of the alloy and its elemental constituents, as obtained from DFT, whereas n_i denotes the number of atoms of a given species i . In case of $(W_{1-x}Al_x)_{1-y}B_{2(1-z)}$ the energy of formation is a measure for the energy gain when an $(W_{1-x}Al_x)_{1-y}B_{2(1-z)}$ alloy is formed from fcc-Al, bcc-W and α -B.

In perfect agreement with earlier results [13], we find WB_2 to be more stable in the ω -phase, whereas AlB_2 prefers the α structure type. However, by including vacancies, the α -phase of WB_2 can indeed be shown to become energetically more favorable [43]. To further interpret our diffraction patterns, we have investigated the evolution of the lattice parameter for the α -phase of AlB_2 and WB_2 with different vacancy concentrations (see Table 2.)

The calculations clearly show that for defect-free crystals, the c-axis lattice parameter of α - WB_2 is actually larger than that one of α - AlB_2 . Thus, the c-axis lattice parameter would decrease with decreasing W content for defect-free α - $(W_{1-x}Al_x)_{1-y}B_{2(1-z)}$ solid solutions, causing a shift of the (001) reflection to higher diffraction angles. However, the opposite effect is observed in our XRD patterns. Again, the incorporation of vacancies in our crystalline structures (due to the PVD process) can account for this behavior. Table 2 clearly shows that the difference in c-axis lattice parameters between α - WB_2 and α - AlB_2 decreases with increasing vacancy content. Finally, in case of $M_{0.875}B_{1.75}$ (i.e., 12.5% Schottky defects) the c-axis lattice parameter of the defected α - WB_2 becomes smaller than that of the defected α - AlB_2 thus being significantly smaller than that of defect-free α - AlB_2 which is in perfect agreement to our previous study [42]. Consequently, the combination of experimental and computational studies strongly points towards an increased vacancy concentration in our PVD films. Moreover, the overall residual stresses can be ruled out as origin of a peak shift in our XRD measurements, as the trend in σ_r would cause a shift in the opposite direction.

The impact of vacancies on the phase stability of $(W_{1-x}Al_x)_{1-y}B_{2(1-z)}$ is indeed striking, as detailed in Fig. 4a. In this figure we show the energy of formation with respect to the chemical composition for defect-free α - and ω - $(W_{1-x}Al_x)_{1-y}B_{2(1-z)}$, and compare it to structures with incorporated metal and boron vacancies. The results clearly point out that the formation of B vacancies, Me vacancies, as well as B and Me vacancies, lead to more positive E_f values for ω -structured $(W_{1-x}Al_x)_{1-y}B_{2(1-z)}$ solid solutions across the entire x range (generally, the E_f -vs-x curve for ω - $(W_{1-x}Al_x)_{1-y}B_{2(1-z)}$ moves upwards when defects are included, Fig. 4a, slightly more on the W-rich side). Consequently, the formation of vacancies is energetically penalized in the ω -phase.

The impact on the α -phase is different. The formation of B, Me, as well as B and Me vacancies leads to more negative E_f values for W-rich solid solutions. The Al-rich part, especially for $x = 1$, only shows slightly more negative E_f values if a small amount of Me vacancies is considered (E_f is slightly more negative for α - $Al_{0.9375}B_2$ than α - AlB_2 , Table 2). The formation of boron vacancies is strongly penalized, leading to E_f values close to zero for $AlB_{1.9375}$ or even positive for higher B-vacancy concentrations (Table 2). Consequently, the formation of B and Me vacancies (especially in form of Schottky defects, the two most right columns of Table 2) turns α - AlB_2 unstable. But with increasing W content this impact is reversed, leading to more negative E_f values for defected α - $(W_{1-x}Al_x)_{1-y}B_{2(1-z)}$ (than defect-free α - $(W_{1-x}Al_x)_{1-y}B_{2(1-z)}$) if x is under

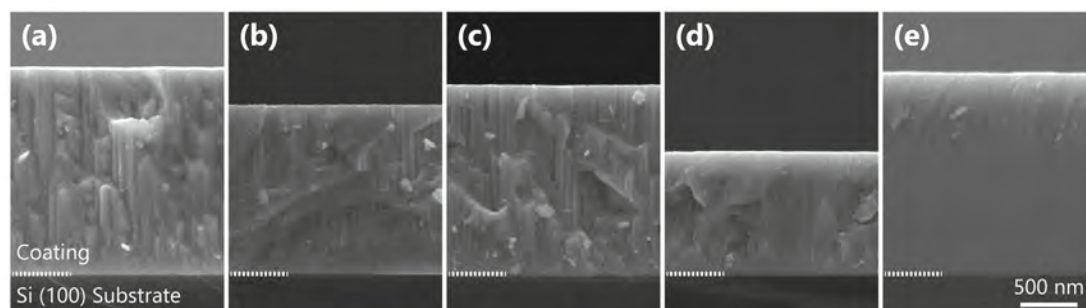


Fig. 3. SEM cross section micrographs of our thin films. The Al content increases from left to right, (a) was deposited with $7.4 \text{ W} \cdot \text{cm}^{-2}$ on the W_2B_{5-z} target and $0.0 \text{ W} \cdot \text{cm}^{-2}$ on the AlB_2 target, (b) with 7.4 and 3.7, (c) 7.4 and 7.4, (d) 3.7 and 7.4, and (e) with 1.9 and $7.4 \text{ W} \cdot \text{cm}^{-2}$ on the W_2B_{5-z} and AlB_2 target respectively. The dashed horizontal line, indicating the interface between film and Si substrate, has the same length as the 500-nm-scale bar.

Table 2

c-axis lattice parameter and E_f for binary $\alpha\text{-AlB}_2$ and $\alpha\text{-WB}_2$ with different vacancy concentrations. Note that a positive E_f means that the structure is unstable with respect to the elemental constituents.

M	MB_2	$\text{MB}_{1.9375}$	$\text{M}_{0.9375}\text{B}_2$	$\text{M}_{0.9375}\text{B}_{1.9375}$	$\text{M}_{0.9375}\text{B}_{1.875}$	$\text{M}_{0.875}\text{B}_{1.75}$
Al	3.30 Å −0.044 eV/at	3.25 Å −0.0125 eV/at	3.26 Å −0.056 eV/at	3.24 Å −0.013 eV/at	3.24 Å +0.041 eV/at	3.17 Å +0.153 eV/at
W	3.40 Å −0.055 eV/at	3.32 Å −0.088 eV/at	3.32 Å −0.096 eV/at	3.24 Å −0.133 eV/at	3.25 Å −0.141 eV/at	3.11 Å −0.165 eV/at

−0.6 (Fig. 4a). For $\alpha\text{-WB}_2$ the impact of B and Me vacancies is similar, both lead to more negative E_f values. Hence, the formation of B vacancies, Me vacancies, as well as B and Me vacancies, is not penalized but even rewarded.

The combination of these effects (promotion of vacancies in the α -structure but penalization thereof in the ω -structure, especially on the W-rich side) leads to the result that the preference of the α -structure over the ω -structure shifts towards higher W-contents, if vacancies are considered. Indeed, while the ω -to α -transition of the defect-free phases is observed at about 40 at% W on the metal sublattice (indicated by the right dashed vertical line in Fig. 4a)—in agreement with recent calculations for increased supercell sizes [13]—all three vacancy types (metal vacancy, boron vacancy and metal plus boron vacancy), shift the transition clearly to the W-rich side, to ~60 at% W for the Me and B vacancy containing structures considered here (indicated by the left dashed vertical line in Fig. 4a). The shift of the ω to α transition to higher W concentrations with increasing vacancy content is nicely represented by the distance of the two dashed vertical lines (Fig. 4a), which emphasizes the importance of point defects such as vacancies on the phase stability.

The fact that all of our crystalline films crystallize in the α structure suggests the presence of even higher defect concentrations as considered within Fig. 4a. For example, when considering 12.5% Schottky defects, the energy of formation of $\alpha\text{-WB}_2$ is with −0.165 eV/at (Table 2) already more negative than that of $\omega\text{-W}_2\text{B}_{5-z}$ ($E_f^{\text{def}} - E_f^{\text{p}}$ is +0.26 eV/at for defect-free WB_2 and only +0.063 eV/at for 6.25% Schottky defect containing WB_2).

For W-metal-fractions below 40 at% not just the energy of formation is always more positive for the ω -phase than for the α -phase, but it is also rather close to zero (if not even positive) for B vacancy containing as well as B and Me vacancy containing Al-rich structures. This agrees with our experiments showing that Al-rich ($\text{W}_{1-x}\text{Al}_x$) $_{1-y}\text{B}_{2(1-z)}$ thin films always became X-ray amorphous, and no crystalline AlB_2 film could be realized so far (in its as deposited state).

In principle, the ab initio calculations predict the formation of the ω -phase for a broad compositional range for defect-free and

low vacancy containing ($\text{W}_{1-x}\text{Al}_x$) $_{1-y}\text{B}_{2(1-z)}$, thus holding as explanation for the formation of $\omega\text{-Al}_{0.50}\text{W}_{0.50}\text{B}_2$ under annealing of the amorphous thin film: here the film (i.e. the crystalline parts inside the film) forms rather under equilibrium like conditions, such that potentially less defects are created during crystal formation, being a prerequisite for the formation of the ω -phase.

In Fig. 4b we depict the energy of formation for $\alpha\text{-}(\text{W}_{1-x}\text{Al}_x)_{1-y}\text{B}_{2(1-z)}$ without ($y = 0, z = 0$) and with Schottky defects (6.25%, i.e. $y = 0.0625, z = 0.625$), indicated by the diamond and asterisk symbols, respectively. Consequently, both cases correspond to stoichiometric compounds. We immediately observe that especially the W-rich side even promotes the formation of Schottky defects. On the Al-rich side (W-metal-fractions below 0.5), clearly the defect-free structure is most stable. This indicates that vacancy containing single-phase ternary ($\text{W}_{1-x}\text{Al}_x$) $_{1-y}\text{B}_{2(1-z)}$ PVD thin films (as observed in our experiments) decompose upon annealing towards vacancy-containing W-rich phases and nearly vacancy-free Al-rich phases. Such a scenario is also indicated in Fig. 4b. Moreover, several compositions were calculated twice with different positions of the considered vacancies in the crystal lattice (Al-near and W-near) which again highlights the preference of vacancies towards the W-rich regions.

Thus, the experimentally observed decomposition of our as deposited single-phase $\alpha\text{-W}_{0.81}\text{Al}_{0.19}\text{B}_2$ thin film upon annealing at 1000°C for 30 min, points towards a spinodal decomposition to form vacancy-free Al-rich domains and defected W-rich domains.

Besides an isostructural spinodal decomposition, a second decomposition pathway is conceivable, as especially the W-rich domains (which would prefer the ω -type for lower vacancy concentrations) could also form an intermediate phase (between the α -type and ω -type). Such an intermediate phase (i.e. a transition from α to ω via a continuous transformation of flat to puckered B-planes) could be seen as a mixture of α - and ω -type or an intermediate structure with e.g. two puckered and four flat boron layers (here simply denoted as μ -type). The formation of such an intermediate phase during decomposition would yield a higher energy gain as puckered layers are energetically favorable for the W-rich part (see the red hexagon in Fig. 4a), with E_f of −0.23 eV.

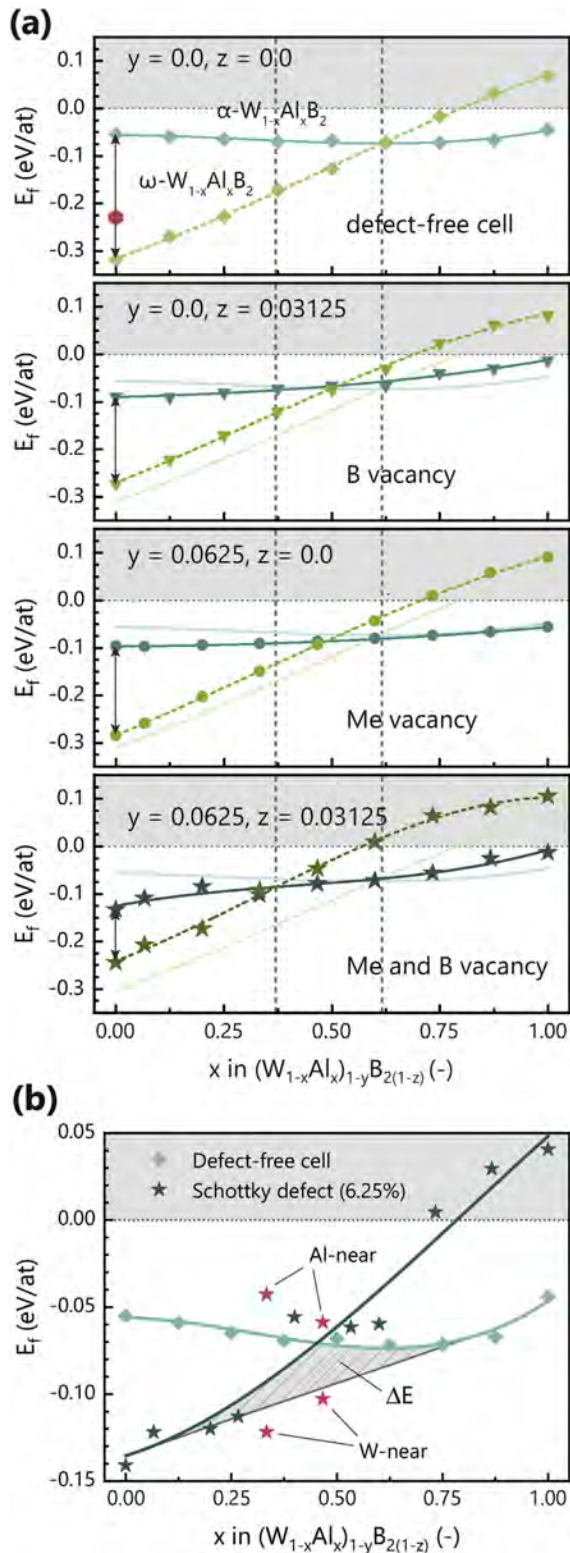


Fig. 4. (a) Energy of formation for different vacancy concentrations of α - $(W_{1-x}Al_x)_{1-y}B_{2(1-z)}$ (solid lines) and ω - $(W_{1-x}Al_x)_{1-y}B_{2(1-z)}$ (dashed lines), as function of the Al metal fraction $x = Al/(Al + W)$. The dashed vertical lines indicate the position of the ω

The above discussion has its focus on the energy of formation and completely neglects entropic contributions to the phase stability. Due to the configurational entropy being a function of the chemical composition, meaning equivalent entropic contributions for both structural modifications of $(W_{1-x}Al_x)_{1-y}B_{2(1-z)}$, it will not affect the composition at which the transition takes place. The vibrational entropy on the other hand, may in principle be different for both modifications, however due to their structural similarity, these differences are expected to become significant only at strongly elevated temperatures. Yet, vacancy containing structures on the other hand may indeed be stabilized by entropy at elevated temperatures.

To investigate the finding that vacancies have especially in the α -structure a different impact on Al-rich or W-rich phases, we have analyzed the electronic density of states (DOS) for different vacancy contents of α -structured AlB_2 and WB_2 . Indeed, both phases α - AlB_2 and α - WB_2 , show a pseudogap in their DOS, which, for the stoichiometric compound, lies below the Fermi level (see Fig. 5). For AlB_2 the pseudogap is only slightly below the Fermi level (E_F), such that introducing vacancies on the metal sublattice indeed moves E_F into the pseudogap, while the DOS otherwise remains rather unchanged. This corresponds to what we would expect from a rigid band model by removing electrons from the system. These findings moreover indicate that for a stoichiometry close to $Al_{0.9375}B_2$ an electronic stabilization of the structure can be expected with the Fermi energy lying in the pseudogap. This is in good agreement with experimental and theoretical work on bulk AlB_2 where stoichiometries of about $Al_{0.9}B_2$ have been proposed [44,45]. For vacancies on the boron sublattice on the other hand, the Fermi level also comes close to the pseudogap, however, the number of states around the Fermi energy is clearly increased, indicating a change in the band structure, going along with a destabilization due to additional anti-bonding states (Fig. 5). Note that the value at E_F is almost the same, but in case of the defect-free structure, the number of states below E_F (antibonding states) decreases, whereas it increases for the boron substoichiometry. Interestingly, further vacancies indeed render the AlB_2 system unstable with respect to decomposition in fcc-Al and α -boron (see E_f in Table 2). This is also clearly visible from the DOS for the case of one metal and two boron vacancies (a Schottky defect, for our supercells used, this is equivalent to 6.25% Schottky defects), which is also depicted in Fig. 5. Here, a significant increase in states in the antibonding region close to E_F is observed. Similarly, we also have studied the effect of vacancies on the electronic structure of α - WB_2 . Now, we find the structure to be highly tolerant with respect to metal and boron vacancies. In fact, with increasing vacancy content the DOS at the Fermi level is gradually decreasing, such that we indeed see an electronic stabilization of the structure. Interestingly, we find that structures with stoichiometric vacancy distribution over the two sublattices (Schottky defects, i.e. $(W_{1-x}Al_x)_{1-y}B_{2(1-z)}$ with $z = 0.03125$ and 0.0625) are more stable than defect-free α - WB_2 in agreement to our previous study [16]. This means that while α - AlB_2 tolerates only a small vacancy content on the metal sublattice, α - WB_2 is electronically stabilized by higher vacancy concentrations

to ω transition for crystals without vacancies (right dashed line) and with Me and B vacancy (left dashed line). The transparent lines shown in the second, third, and fourth panel are the normalized (with regard to chemical composition) data of the first panel (for defect-free cells), providing an overview on the trends. The red hexagon denotes an intermediate phase between α - WB_2 and ω - W_2B_{5-z} , consisting of two puckered and four flat boron layers. (b) shows a possible scenario for the decomposition of the experimentally observed $(W_{0.81}Al_{0.19})_{1-y}B_{2-z}$ coating into defect-free Al rich $(Al,W)B_2$ and defected W-rich $(W,Al)B_2$. The consequential minimum energy gain is marked as grey area. The red asterisks denote variations in the vacancy distribution (near the W-atom or the Al-atom). (For interpretation of the references to color in this figure legend, the reader is referred to the Web version of this article.)

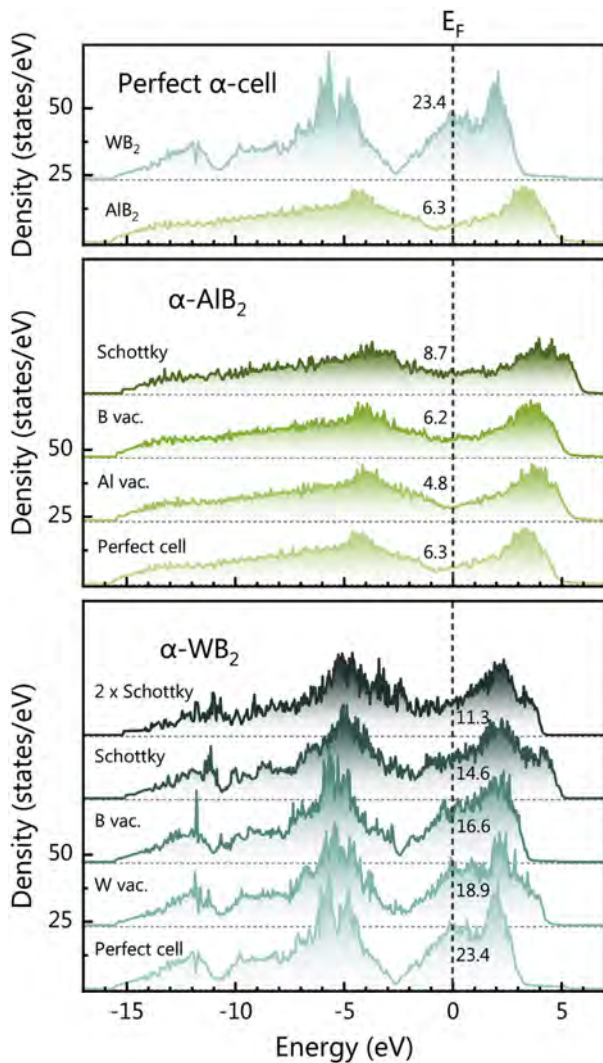


Fig. 5. DOS for different vacancy configurations of α -AlB₂ and α -WB₂. The values besides the dashed line showing the Fermi-level indicate the number of states at the Fermi energy.

on both sublattices. Finally, we need to mention that the samples showed a significant difference in their oxidation stability if containing Al or not. The Al-free WB₂ coatings showed already after 1 week of ambient air exposure a change of their color towards greenish appearance, indicating ongoing oxidation processes. Contrary, the Al-containing samples (even if only 2.3 at% at the metal sublattice) did not show such a change.

4. Summary and conclusion

Making use of the interplay between two different polymorphs has been shown to result in materials with improved mechanical properties. Especially in the well-known Ti_{1-x}Al_xN system metastable cubic solid solutions have shown significantly improved hardness and better ductility. Similarly, we show here that WB₂ can be alloyed with up to 20 at% Al metal-fraction without significant performance loss, pointing to an increased oxidation stability due to Al, as one would expect the formation of an Al-oxide passivation

layer. This, however, has to be further investigated. Hence, the main advantage of Al addition to WB₂ thin films is a self-passivation at ambient conditions, as well as an increased oxidation resistance in possible future applications. Unfortunately, a further increase of the Al-content to the Al-rich side could be shown to be difficult, which is especially due to the destabilizing nature of boron vacancies. This leaves us with an interesting situation: While vacancies electronically stabilize the α -over the ω -phase for high W contents, they at the same time destabilize the α -phase at high Al contents, making it difficult to grow crystalline α -AlB₂ by PVD (with their typically high fraction of point defects). This once more points to the importance of point defects for stability and mechanical properties of PVD deposited coatings, a fact that is now also understood to be crucial for boride-based coatings.

Acknowledgment

We thank Dr. Helmut Riedl and Dr. Matthias Bartosik for fruitful discussions on thin film deposition and XRD analysis. We thank the Vienna Scientific Cluster for the attribution of computation time, the center for transmission electron microscopy of TU Wien (USTEM) for providing the SEM, and the X-ray center of TU Wien for beam time. The present study was partly held within START Project (Y371) of the Austrian Science Fund. The financial support by the Austrian Federal Ministry of Economy, Family and Youth and the National Foundation for Research, Technology and Development is greatly acknowledged. We also thank Oerlikon Surface Solutions AG and Plansee Composite Materials GmbH for the financial support.

References

- [1] P.H. Mayrhofer, C. Mitterer, L. Hultman, H. Clemens, Microstructural design of hard coatings, *Prog. Mater. Sci.* 51 (2006) 1032–1114, <https://doi.org/10.1016/j.pmatsci.2006.02.002>.
- [2] R. Hahn, M. Bartosik, R. Soler, C. Kirchlechner, G. Dehm, P.H. Mayrhofer, Superlattice effect for enhanced fracture toughness of hard coatings, *Scripta Mater.* 124 (2016), <https://doi.org/10.1016/j.scriptamat.2016.06.030>.
- [3] H. Riedl, A. Vieweg, A. Limbeck, J. Kalas, M. Arndt, P. Polcik, H. Euchner, M. Bartosik, P.H. Mayrhofer, Thermal stability and mechanical properties of boron enhanced Mo-Si coatings, *Surf. Coating Technol.* (2015), <https://doi.org/10.1016/j.surfcoat.2015.09.015>.
- [4] P.H. Mayrhofer, D. Music, J.M. Schneider, Ab initio calculated binodal and spinodal of cubic Ti_{1-x}Al_xN, *Appl. Phys. Lett.* 88 (2006) 071922, <https://doi.org/10.1063/1.2177630>.
- [5] P.H. Mayrhofer, L. Hultman, J.M. Schneider, P. Staron, H. Clemens, Spinodal decomposition of cubic Ti_{1-x}Al_xN: comparison between experiments and modeling, *Int. J. Mater. Res.* 98 (2007) 1054–1059, <https://doi.org/10.3139/146.101570>.
- [6] R. Rachbauer, S. Massl, E. Stergar, D. Holec, D. Kiener, J. Keckes, J. Patscheider, M. Stiefel, H. Leitner, P.H. Mayrhofer, Decomposition pathways in age hardening of Ti-Al-N films, *J. Appl. Phys.* (2011), <https://doi.org/10.1063/1.3610451>.
- [7] P.H. Mayrhofer, A. Hörling, L. Karlsson, J. Sjölen, T. Larsson, C. Mitterer, L. Hultman, Self-organized nanostructures in the Ti-Al-N system, *Appl. Phys. Lett.* 83 (2003) 2049–2051, <https://doi.org/10.1063/1.1608464>.
- [8] A. Hörling, L. Hultman, M. Odén, J. Sjölen, L. Karlsson, Thermal stability of arc evaporated high aluminum-content Ti_{1-x}Al_xN thin films, *J. Vac. Sci. Technol. A Vacuum, Surfaces, Film.* 20 (2002) 1815–1823, <https://doi.org/10.1116/1.1503784>.
- [9] M. Schlögl, C. Kirchlechner, J. Paulitsch, J. Keckes, P.H. Mayrhofer, Effects of structure and interfaces on fracture toughness of CrN/AlN multilayer coatings, *Scripta Mater.* 68 (2013) 917–920, <https://doi.org/10.1016/j.scriptamat.2013.01.039>.
- [10] M. Bartosik, C. Rumeau, R. Hahn, Z.L. Zhang, P.H. Mayrhofer, Fracture toughness and structural evolution in the TiAlN system upon annealing, *Sci. Rep.* 7 (2017) 16476, <https://doi.org/10.1038/s41598-017-16751-1>.
- [11] M. Bartosik, H.J. Böhm, C. Krywka, Z.L. Zhang, P.H. Mayrhofer, Influence of phase transformation on the damage tolerance of Ti-Al-N coatings, *Vacuum* (2018), <https://doi.org/10.1016/j.vacuum.2018.06.001>.
- [12] H. Euchner, P.H. Mayrhofer, Designing thin film materials — ternary borides from first principles, *Thin Solid Films* 583 (2015) 46–49, <https://doi.org/10.1016/j.tsf.2015.03.035>.
- [13] H. Euchner, P.H. Mayrhofer, H. Riedl, F.F. Klimashin, A. Limbeck, P. Polcik, S. Kolozsvari, Solid solution hardening of vacancy stabilized Ti_xW_{1-x}B₂, *Acta Mater.* 101 (2015) 55–61, <https://doi.org/10.1016/j.actamat.2015.08.048>.

- [14] O.V. Sobol, O.N. Grigoryev, Y.A. Kunitsky, S.N. Dub, A.A. Podtelezchnikov, A.N. Stetsenko, Peculiarities of structure state and mechanical characteristics in ion-plasma condensates of quasibinary system borides W₂B₅-TiB₂, *Sci. Sinter.* (2006), <https://doi.org/10.2298/SOS0601063S>.
- [15] B. Alling, H. Högberg, R. Armiento, J. Rosen, L. Hultman, A theoretical investigation of mixing thermodynamics, age-hardening potential, and electronic structure of ternary M^{1-x}M^{2-x}B₂ alloys with AlB₂ type structure, *Sci. Rep.* (2015), <https://doi.org/10.1038/srep09888>.
- [16] C. Fuger, V. Moraes, R. Hahn, H. Bolvardi, P. Polcik, H. Riedl, P.H. Mayrhofer, Influence of Tantalum on phase stability and mechanical properties of WB₂, *MRS Commun* (2019) 1–6, <https://doi.org/10.1557/mrc.2019.5>.
- [17] V. Moraes, C. Fuger, V. Paneta, D. Primetzhofer, P. Polcik, H. Bolvardi, M. Arndt, H. Riedl, P.H. Mayrhofer, Substoichiometry and tantalum dependent thermal stability of α -structured W-Ta-B thin films, *Scripta Mater.* 155 (2018) 5–10, <https://doi.org/10.1016/j.scriptamat.2018.06.005>.
- [18] P. Losbichler, C. Mitterer, Non-reactively sputtered TiN and TiB₂ films: influence of activation energy on film growth, *Surf. Coating. Technol.* (1997), [https://doi.org/10.1016/S0257-8972\(97\)00331-9](https://doi.org/10.1016/S0257-8972(97)00331-9).
- [19] P.H. Mayrhofer, C. Mitterer, J.G. Wen, J.E. Greene, I. Petrov, Self-organized nanocolumnar structure in superhard TiB₂ thin films, *Appl. Phys. Lett.* 86 (2005) 131909, <https://doi.org/10.1063/1.1887824>.
- [20] V. Moraes, H. Riedl, C. Fuger, P. Polcik, H. Bolvardi, D. Holec, P.H. Mayrhofer, Ab initio inspired design of ternary boride thin films, *Sci. Rep.* (2018), <https://doi.org/10.1038/s41598-018-27426-w>.
- [21] W. Hofmann, W. Jäniche, Der strukturtyp von Aluminiumborid (AlB₂), *Naturwissenschaften* 23 (1935) 851.
- [22] H.P. Woods, F.E. Wawner, B.G. Fox, Tungsten diboride: preparation and structure, *Science* (1966), <https://doi.org/10.1126/science.151.3706.75>.
- [23] M. Frotscher, W. Klein, J. Bauer, M₂B₅ or M₂B₄ Reinvestigation of the Mo/B and W/B System, vol. 633, 2007, pp. 2626–2630.
- [24] C. Jiang, Z. Pei, Y. Liu, J. Xiao, J. Gong, C. Sun, Preparation and characterization of superhard AlB₂-type WB₂ nanocomposite coatings, *Phys. Status Solidi* 210 (2013) 1221–1227, <https://doi.org/10.1002/pssa.201228828>.
- [25] Y.M. Liu, C.L. Jiang, Z.L. Pei, H. Lei, J. Gong, C. Sun, Microstructure and properties of AlB₂-type WB₂ thin films deposited by direct-current magnetron sputtering, *Surf. Coating. Technol.* 245 (2014) 108–116, <https://doi.org/10.1016/j.surfcoat.2014.02.049>.
- [26] H. Euchner, P.H. Mayrhofer, Vacancy-dependent stability of cubic and wurtzite Ti_{1-x}Al_xN, *Surf. Coating. Technol.* 275 (2015) 214–218, <https://doi.org/10.1016/j.surfcoat.2015.05.017>.
- [27] F.F. Klimashin, N. Koutná, H. Euchner, D. Holec, P.H. Mayrhofer, The impact of nitrogen content and vacancies on structure and mechanical properties of Mo-N thin films, *J. Appl. Phys.* (2016), <https://doi.org/10.1063/1.4966664>.
- [28] P. Bliem, S. Mráz, S. Sen, O. Hunold, J.M. Schneider, Self-passivating (Re,Al)B₂ coatings synthesized by magnetron sputtering, *Sci. Rep.* 8 (2018) 15570, <https://doi.org/10.1038/s41598-018-34042-1>.
- [29] I. Petrov, A. Hall, A.B. Mei, N. Nedfors, I. Zhirkov, J. Rosen, A. Reed, B. Howe, G. Greczynski, J. Birch, L. Hultman, J.E. Greene, Controlling the boron-to-titanium ratio in magnetron-sputter-deposited TiB_x thin films, *J. Vac. Sci. Technol. A Vacuum, Surfaces, Film.* (2017), <https://doi.org/10.1116/1.4982649>.
- [30] A. Cakara, M. Bonta, H. Riedl, P.H. Mayrhofer, A. Limbeck, Development of a multi-variate calibration approach for quantitative analysis of oxidation resistant Mo-Si-B coatings using laser ablation inductively coupled plasma mass spectrometry, *Spectrochim. Acta Part B At. Spectrosc.* (2016), <https://doi.org/10.1016/j.sab.2016.04.004>.
- [31] W.D. Nix, Mechanical properties of thin films, *Metall. Trans. A.* 20 (1989) 2217–2245, <https://doi.org/10.1007/BF02666659>.
- [32] G.M. Pharr, W.C. Oliver, Measurement of thin film mechanical properties using nanoindentation, *MRS Bull.* 17 (2013) 28–33, <https://doi.org/10.1557/S0883769400041634>.
- [33] G. Kresse, J. Hafner, Ab-initio molecular dynamics for liquid metals, *Phys. Rev. B* 47 (1993) 558–561.
- [34] G. Kresse, Efficient iterative schemes for ab initio total-energy calculations using a plane-wave basis set, *Phys. Rev. B* 54 (1996) 11169–11186, <https://doi.org/10.1103/PhysRevB.54.11169>.
- [35] G. Kresse, J. Furthmüller, Efficiency of ab-initio total energy calculations for metals and semiconductors using a plane-wave basis set, *Comput. Mater. Sci.* (1996), [https://doi.org/10.1016/0927-0256\(96\)00008-0](https://doi.org/10.1016/0927-0256(96)00008-0).
- [36] J.P. Perdew, Y. Wang, Accurate and simple analytic representation of the electron-gas correlation energy, *Phys. Rev. B* (1992), <https://doi.org/10.1103/PhysRevB.45.13244>.
- [37] A. Zunger, S.H. Wei, L.G. Ferreira, J.E. Bernard, Special quasirandom structures, *Phys. Rev. Lett.* (1990), <https://doi.org/10.1103/PhysRevLett.65.353>.
- [38] A. Van De Walle, P. Tiwary, M. De Jong, D.L. Olmsted, M. Asta, A. Dick, D. Shin, Y. Wang, L.Q. Chen, Z.K. Liu, Efficient stochastic generation of special quasirandom structures, *Calphad Comput. Coupling Phase Diagrams Thermochem.* (2013), <https://doi.org/10.1016/j.calphad.2013.06.006>.
- [39] K. Momma, F. Izumi, VESTA 3 for three-dimensional visualization of crystal, volumetric and morphology data, *J. Appl. Crystallogr.* (2011), <https://doi.org/10.1107/S0021889811038970>.
- [40] Powder Diffraction File 00-009-0154, International Center for Diffraction Data, 2011 (n.d.).
- [41] Powder Diffraction File 00-006-0243, International Center for Diffraction Data, 2011 (n.d.).
- [42] V. Moraes, C. Fuger, V. Paneta, D. Primetzhofer, P. Polcik, H. Bolvardi, M. Arndt, H. Riedl, P.H. Mayrhofer, Substoichiometry and tantalum dependent thermal stability of α -structured W-Ta-B thin films, *Scripta Mater.* 155 (2018) 5–10, <https://doi.org/10.1016/j.scriptamat.2018.06.005>.
- [43] W. Hayami, A. Momozawa, S. Otani, Effect of defects in the formation of AlB₂-Type WB₂ and MoB₂, *Inorg. Chem.* 52 (2013) 7573–7577, <https://doi.org/10.1021/ic400587j>.
- [44] U. Burkhardt, V. Gurin, F. Haarmann, H. Borrmann, W. Schnelle, A. Yaresko, Y. Grin, On the electronic and structural properties of aluminum diboride AlO₉B₂, *J. Solid State Chem.* 177 (2004) 389–394, <https://doi.org/10.1016/j.jssc.2002.12.001>.
- [45] I. Loa, K. Kunc, K. Syassen, P. Bouvier, Crystal structure and lattice dynamics of AlB₂ under pressure and implications for MgB₂, *Phys. Rev. B Condens. Matter* 66 (2002) 1–8, <https://doi.org/10.1103/PhysRevB.66.134101>.

Publication V

Influence of the Superlattice Effect on the Mechanical Properties of the MoN-TaN system: a computational and experimental approach

R. Hahn, N. Koutná, T. Wójcik, A. Davydok, D. Holec, M. Bartosik, and P. H. Mayrhofer
Manuscript in final preparation

Influence of the Superlattice Effect on the Mechanical Properties of the MoN-TaN system: a computational and experimental approach

R. Hahn,^{1,*} N. Koutná,¹ T. Wójcik,¹ A. Davydok,² D. Holec,³ M. Bartosik,¹ and P. H. Mayrhofer¹

¹*Institute of Materials Science and Technology, TU Wien, 1060 Vienna, Austria*

²*Aix Marseille Univ, Univ de Toulon, CNRS, IM2NP UMR 7334, 13397 Marseille, France*

³*Department of Materials Science, Montanuniversität Leoben, 8700 Leoben, Austria*

(Dated: June 6, 2019)

Machining and forming tools are exposed to challenging environments, requiring protective coatings for enhanced lifetime and reliability. The properties needed to withstand mechanical and chemical attacks are primarily fulfilled by transition metal nitrides. However, they lack in ductility and are thus prone to premature failure due to peak stresses. Herein we present a computational and experimental study revealing structural and mechanical properties of the MoN-TaN superlattice system. We found a metastable tetragonal distorted phase of TaN (ζ -structure) up to layer thicknesses of 2.5 nm together with an increased fracture toughness and hardness. Density functional theory calculations and experimental results further reveal an ensuing metal-vacancy stabilized Ta_{0.75}N phase with an increased Young's modulus but significant lower fracture toughness. Apart from this context we discuss the influence of coherency strains on the fracture properties of superlattice thin films. Our results demonstrate the impact of phase formation and -stabilization on the mechanical properties of MoN-TaN superlattices. Most notably we were able to predict those properties by ab initio calculations.

Keywords: Thin films; sputtering; superlattices; micromechanical testing; density functional theory

I. INTRODUCTION

Thin ceramic films deposited using physical vapour deposition (PVD), i.e. transition metal borides, carbides, nitrides, and oxides, are used as protective coatings in the cutting and forming tool industry [1, 2]. They prolong the lifetime of their underlying tool, e.g. WC-Co or hot working steel, by up to some 100%. Their beneficial properties like high hardness, high Young's modulus, chemical stability, thermal stability, and oxidation resistance provide an ideal basis for application in harsh environments [3–5]. However, the constant endeavour in industrial processes for increased throughput in cutting and forming processes without suffering restrictions in reliability leads to a demand for even better coatings. A weak point of such coatings is their low fracture toughness K_{IC} , a material property difficult to quantify for hard coatings and thus has yet to be comprehensively researched. However, recent advances in micromechanical testing methods – applying in-situ secondary electron microscope testing (SEM) using focused ion beam (FIB) shaped geometries – established the possibility to do so [6–8]. Since low K_{IC} values can lead to premature failure of the coating and thus to lack of performance in industrial processes, especially when mechanical loads dominate the wear behaviour, the fracture toughness is technologically relevant [2]. Not only the fracture toughness – a property describing the resistance of a material against crack propagation – but also the damage tolerance, a term including strength and fracture toughness, is important to prevent early failure.

Known mechanisms to increase the fracture toughness of ceramic materials can be divided in two characteristics: intrinsic and extrinsic mechanisms [9]. While extrinsic mechanisms often base on a reduction of the stress intensity at the crack tip, intrinsic effects draw upon increasing necessary maximum stress intensities for crack propagation as well as crack initiation. Examples for extrinsic strategies commercially used in hard coatings are for instance ductile phase toughening, toughening through nanostructural design, and toughening through multi-(nano-) layered structures [10–16]. Intrinsic mechanisms are in contrast not easily accessible; however, Sangiovanni *et al.* calculated increased Poisson's ratio, Cauchy pressure (C_{12} - C_{44}), and decreased G/B ratio (all of the latter are indicating a more ductile behaviour) for Mo, W, Nb, and Ta alloyed nitrides [17]. They conclude a toughness increase primarily originating from increased valence electron concentration (VEC) and a following change in bonding states.

Our study [18] was a first probe of the cubic-based nanolayered MoN/TaN system analysing the impact of vacancies on the thermodynamics, elasticity, vibrational and electronic properties employing first principles calculations. The most stable (defect) configurations at bilayer period of 2 nm were predicted for various experimental conditions (i.e., by varying chemical potentials). Chemical analysis using EDX suggested that our experimental coatings contained N vacancies in MoN layers. Together with the XRD analysis and indentation data vs. the DFT Young's moduli, the proposed chemistry was MoN_{0.5}/Ta_{0.5}N. Such result was somewhat surprising, considering the well-known driving force of TaN for point defects (mainly vacancies). In our case, the TaN layers of the superlattice were formed by a stoichiometric tetragonally distorted ζ -Ta_{0.5}N [18].

* rainer.hahn@tuwien.ac.at, Tel.: +43 (0)1 58801 308 104

The purpose of this study is to investigate the fracture properties of nanolayered MoN/TaN coatings, referred to as superlattices (SL), with different bilayer periods. This system was chosen because of the high VECs of both of its constituents. Furthermore, they possess a similar shear modulus G (124 GPa for the stable MoN_{0.5} and 127 GPa for cubic, defect free TaN, and 159 GPa for ζ -TaN) [19], while having different lattice parameter a , which enables us to provide new insight on the relevant mechanism behind the fracture toughness enhancement observed for superlattice films apart from the well-known hardness increase [20]. We demonstrate the structure property relation of this coating system by applying *in situ* micromechanical experiments, x-ray diffraction, scanning electron microscopy, transmission electron microscopy investigations, and synchrotron nanodiffraction experiments. The results are corroborated and supplemented using *ab initio* calculations.

II. EXPERIMENTAL

Our coatings were deposited using a lab scale AJA Orion 5 sputtering system. Two confocal 2-inch cathodes, equipped with an unbalanced magnetron system were powered in current controlled mode at a maximum current density of 19.7 mA/cm². Our targets had a purity of 99.6% (Plansee Composite Materials GmbH). The nanolayer architectures were realized using a computer-controlled shutter system. The base pressure of our coating system was lower than 10⁻⁴ Pa. Prior to deposition the substrates were ultrasonically cleaned in acetone and ethanol for five minutes each, heated to deposition temperature (380 °C), thermally cleaned for 20 minutes and plasma etched in Ar plasma (6 Pa). We used a gas mixture of Ar and N₂, 7 and 3 sccm respectively, at a total pressure of 0.4 Pa to deposit our thin films on the rotating substrates (Si (100), MgO (100), Al₂O₃ (1102)). The nominal bilayer periods were set to 1.5, 3.0, 6.0, 9.0, 15.0, and 45.0 nm. Additionally – to achieve a dense coating morphology – we applied a negative bias voltage of -40 V.

Mo and N are thereby stabilized – depending on the total nitrogen content during deposition – by nitrogen vacancies in the cubic NaCl (space group #225, Fm $\bar{3}$ m) structure, and thus present as MoN_{0.5}. TaN on the other hand crystallizes in a hexagonal crystal system (space group #189, P-62m, TaN prototype); however, we expect it to be stabilized in its less stable tetragonal structure (ζ -TaN) due to the template effect from MoN_{0.5}, a similar mechanism reported in CrN/AlN hard coatings for c-AlN [21]. Other possible phases occurring are the metal vacancy stabilized cubic Ta_{0.75}N, and Schottky-defect stabilized rock-salt (rs)-Ta_{1-x}N_{1-x} (sd-TaN), see Ref. [19].

To carry out the DFT calculations, we used the Vienna Ab-initio Simulation Package (VASP) [22, 23] together with the projector augmented plane wave (PAW) pseudopotentials. The exchange-correlation effects were incorporated employing the generalized gradient approxima-

tion (GGA) [24] using a Perdew-Burke-Ernzerhof (PBE) exchange and correlation functional [25]. The plane-wave cut-off energy was always set to 600 eV, while the k-vector sampling of the Brillouin zone provided a total energy accuracy of about 10⁻³ eV/at or better.

The models for MoN/TaN superlattices were based on the cubic rock salt (Fm $\bar{3}$ m) structure. Various bilayer periods were constructed by stacking a desired number of cubic cells in the (100) direction. The desired number of point defects (vacancies or Schottky defects) was generated in an ordered or disordered manner employing the SQS method [26]. In the latter case, a sufficiently large supercell (containing 64 and 128 atoms for the bulk and the SL systems, respectively) was produced. Lattice parameters of the defect-free structures were optimized by fitting the energy vs. volume data with the Birch-Murnaghan equation of state [27], while all structure optimizations in the vacancy-containing supercells were performed by relaxing the volume, shape, and atomic positions.

To provide an insight into the elastic behaviour of selected systems, a tensor of elastic constants was derived from the Hooke's law by applying the stress-strain method [28–30]. Subsequently, we used the Voigt's notation to transform this fourth-order elastic tensor to a 6x6 matrix which was further projected onto a desirable (cubic or tetragonal) symmetry [31]. The polycrystalline bulk, B, and shear, G, moduli were determined by averaging the Hill's and Voigt's estimates [32, 33], while the polycrystalline Young's modulus, E, was evaluated as

$$E = \frac{9 \cdot BG}{3 \cdot B + G} \quad (1)$$

Following formulas in Ref. [34], we computed Young's modulus values in the prominent crystallographic directions. Tendency for brittle/ductile behavior was estimated by plotting the G/B ratio vs. Poisson's ratio, $\nu = (3B - 2G)/(6B + 2G)$, or alternatively, Cauchy pressure/E, $c_{12} - c_{44}/E$. Considering the defected SLs – which do not exhibit overall cubic but tetragonal symmetry – as well as the hexagonal boride systems, effective Cauchy pressure value was estimated as $1/3(c_{12} - c_{66} + c_{13} - c_{55} + c_{23} - c_{44})$. Since bilayer period dependent trends in mechanical properties are very costly to obtain from first-principles (especially when it comes to defected systems).

The increasing demands on CPU time and/or memory motivated us to estimate elastic properties of SLs with higher bilayer periods using a computationally cheaper approach by Grimsditch and Nizzoli [35]. In the original formulation, this linear elasticity continuum model allows to calculate effective elastic constants of a system composed of two layers having arbitrary symmetry requiring elastic constants of the two-layer materials together with their molar ratio. The model, however, disregards any heterogeneity introduced by interfaces. In particular, the input elastic constants correspond to the equilibrium lattice parameters of each individual phase which not properly represent the stress state of the material in the

SL. To provide a more realistic picture of the interface, the original formalism was extended to a generally n layers forming the SL in question [36]. The interface effects were modelled by setting the elastic constants of one of the n layer materials to those of a chosen superlattice with a small bilayer period. By varying the volume ratio of the interface layer (of a certain thickness) and the remaining bulk-like layers, we managed to predict elastic data depending on the desired bilayer period, which would not have been possible using the original Grimsditch-Nizzoli formalism. Furthermore, to corroborate our fracture experiments, tensile strength in terms of cleavage energy and stress for brittle cleavage were estimated using the rigid-block displacement method [37, 38].

Transmission electron microscopy (TEM) investigations were performed on a FEI Tecnai F20 equipped with a field emission gun. All our TEM samples were produced using the dual beam Focused Ion Beam (FIB) and applying the lift-out method [39]. To reduce the Ga^+ ion damage, we reduced the milling current down to 0.1 nA and sputter-cleaned our sample using a Technoorg Linda Gentle mill. X-ray diffraction patterns were recorded using a Panalytical XPert Pro MPD θ - θ diffractometer in Bragg Brentano configuration. The x-ray source was a $\text{Cu-K}\alpha$ source ($\lambda = 1.5418 \text{ \AA}$). Nanodiffraction experiments were conducted at the nanofocus endstation of Beamline P03 at PETRAIII located at synchrotron facility DESY (Hamburg), the used monochromatic X-ray radiation had a wavelength of $\lambda = 0.80533 \text{ \AA}$ (15.0 keV beam energy). The sample was placed in transmission geometry, to collect Debye Scherrer patterns using a cross sectional approach [40]. Hardness measurements were performed in compliance with guidelines given by [41], and evaluated using the method after Oliver and Pharr with a Fischer Cripps Laboratories ultra-micro indentation system (UMIS) equipped with a Berkovich diamond tip [42]. To eliminate possible substrate effects, we calculated the Young's modulus of our coatings by extrapolating E vs. h to zero indentation depth for different substrates following [43].

We conducted micromechanical experiments to calculate the fracture toughness of our thin films. Hereby we first dissolved the substrate (Si (100)) in aqueous KOH (with a concentration of 40 wt.% KOH and a temperature of 70°C) to obtain free standing thin film material. We FIB machined microcantilevers (FEI Quanta 200 3D DBFIB) according to regulations given by [44]. The initial current used for milling with our Ga^+ ion source was 1.0 nA, subsequently reduced to 0.5 nA to prevent unwanted damage. The initial notch was machined with a current of 50 pA. These cantilevers were then loaded with a Hysitron PI-85 Scanning electron microscope (SEM) PicoIndenter equipped with a spherical diamond tip (diameter of $1 \mu\text{m}$) inside a FEI Quanta 200 FEGSEM. We performed these tests in displacement-controlled mode ($5 \text{ nm}\cdot\text{s}^{-1}$) to obtain the maximum force before failure. This also enabled us to monitor possible mode I violations and assure linear elastic behaviour of our beams. The fracture toughness was then calculated according to

Matoy *et al.* [45]:

$$K_{IC} = \frac{P_{max} \cdot l}{b \cdot w^{\frac{3}{2}}} \cdot f\left(\frac{a}{w}\right) \quad (2)$$

with

$$f\left(\frac{a}{w}\right) = 1.46 + 24.36 \cdot \left(\frac{a}{w}\right) - 47.21 \cdot \left(\frac{a}{w}\right)^2 + 75.18 \cdot \left(\frac{a}{w}\right)^3 \quad (3)$$

where P_{max} is the maximum force before fracture, a the depth of the initial notch, b the cantilever width, and w the cantilever thickness (film thickness in this case). We performed 7 fracture tests for each system with a total success rate of 87%.

III. RESULTS

In order to estimate relative tendency for brittle/ductile behavior of the monolithic as well as SL coatings, first-principles calculations on elastic constants were carried out. The structures in question were rs-MoN_{0.5}, rs-TaN, MoN_{0.5}/TaN SL with (001) interface and $\Lambda=1.7$ and 3.5 nm , as well as rs-AlN, rs-TiN, and AlN/TiN SL with (001) interface and $\Lambda=1.7 \text{ nm}$ for comparison. The polycrystalline bulk, B, shear, G, and Young's moduli, E, together with the Poisson's ratio, ν , and Cauchy pressure, c_p , were evaluated using the calculated elastic constants. Subsequently, the brittleness/ductility map was constructed by plotting ν and c_p/E , respectively, against the G/B ratio. Fig. 1 clearly shows that all our data points fall onto the decreasing hyperbolic line connecting c_p/E over B/G values of cubic and hexagonal structures. Unlike the rs-AlN, rs-TiN, and AlN/TiN SL, the rs-MoN_{0.5}, rs-TaN, MoN_{0.5}/TaN SL are found within the ductile region. The rs-TaN is predicted to slightly outperform its monolithic rs-MoN_{0.5} counterpart in terms of ductility, whereas the behavior of MoN_{0.5}/TaN SL seems to be largely influenced by the bilayer period. Specifically, the SL with $\Lambda=1.7 \text{ nm}$ is less ductile than its single-phase components, unlike the $\Lambda=3.5 \text{ nm}$ variant, which leads to the highest ductility out of all the here considered structures.

The literature data presented in Fig. 1 (gray fitted lines are cubic oxides, nitrides, and carbides, as well as hexagonal borides) show a hyperbolic relationship between the G/B and the c_p/E ratio. The relation is described by [48] as a universal criterion for cubic materials regarding their strength and ductility. Deviations from this relation mostly belong to metastable structures, i.e. c-AlN or c-TaN. Also, the data for hexagonal diborides (light gray stars in Fig. 1) fall on a hyperbola, located $\sim 0.3 c_p/E$ under that of cubic materials. This in turn would tell us that diborides in general tend to be stronger but less ductile in comparison with their cubic counterparts. Also, in this case, deviations from the hyperbola mostly belong to metastable structures.

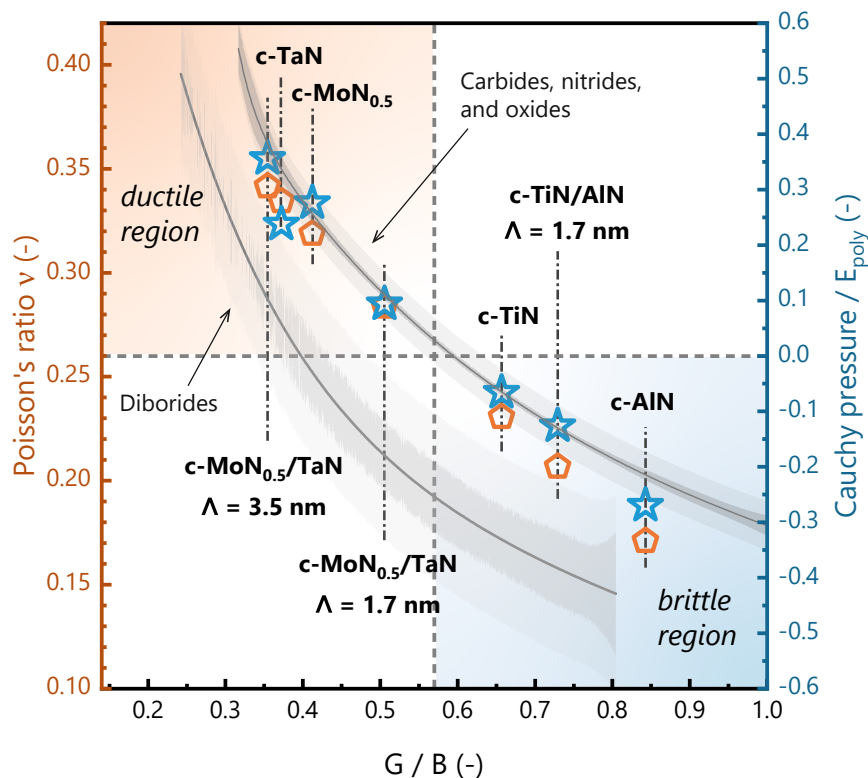


Fig. 1. The G/B ratio (according to the Pugh criterion, $G/B \geq 0.571$ for ductile materials [46]) as a function of the Poisson's ratio (according to the Frantsevich criterion: $\nu > 0.26$ for ductile materials [47]) is indicated by orange pentagons. The G/B dependence on the Cauchy pressure over the polycrystalline Young's modulus ($c_p/E > 0$ for tough materials [48]) is indicated with blue stars. The gray fitted curves with a 95% confidence band and a 95% prediction band correspond to data for cubic carbides, nitrides, and oxides, and to hexagonal borides. Our calculations are labelled using dot dashed lines. The ductile region is located at the left top corner (orange background), the brittle region at the bottom right corner (blue background). The dashed lines mark the various toughness criteria (the scale was chosen in a way that the Frantsevich criterion and the criterion by [48] are on the same height). The literature data can be found in Tab. A-I (see Appendix).

Motivated by the ab initio predicted promising toughness and ductility of the MoN/TaN system, we proceeded with experimental investigations. As a first step, we employed electron microscopy and diffraction methods to study morphology of the deposited MoN_{0.5}/TaN multilayered coatings.

Our coatings have a dense morphology, visible in the SEM cross section pictures (Fig. 2(a)-(c)). We can further state that there was no interrupted growth as the columns are not re-nucleating between the single layers (insert in Fig. 2(c)), indicating coherent growth. This is also shown in Fig. 2(d) depicting a TEM cross section of the coating with $\Lambda = 3.0$ nm. Additionally, we observe the desired layered structure; the bilayer period of this sample was measured to be ~ 2.9 nm (by averaging 10 bilayers, not shown here). The white square in Fig. 2(d) shows the region chosen for Fast Fourier Transformation (FFT) in Fig. 2(g). We do not observe any sign of other phases than cubic structures in the [110] orientation.

A typical plan view TEM image is shown in Fig. 2(e) ($\Lambda = 1.5$ nm). The in-plane grain size, i.e. the column width, of our coatings is $D_{||} \sim 46$ nm as obtained by applying the linear intercept method [49]. A Selected Area Electron Diffraction (SAED) pattern of this region is shown in Fig. 2(f). In order to enhance the visibility of the structures present, we integrated this pattern using the PASAD plugin [50] in Gatan Digital Micrograph and subtracted the underground (inserted). The obtained

pattern shows no signs of other phases than cubic, the main peaks are labelled.

X-ray diffraction experiments show cubic structures in the measured out-of-plane direction (Bragg-Brentano). We do not observe any signs of the hexagonal TaN phase; also, Mo-N is present in its cubic MoN_{0.5} structure following the accordance of measured, calculated, and literature-based lattice constants (Fig. 3(a)) [19, 51]. The coatings with $\Lambda = 1.5$ and 3.0 nm show an average Bragg-reflection in between the calculated peak positions for TaN and MoN_{0.5}. With increasing bilayer period, this peak splits into two peaks, staying at a similar position for larger Λ (Fig. 3(a)). Additionally, one can deduce from the XRD measurements a pronounced layered structure due to positive and negative satellite peaks (indicated with $m \pm 1$ and arrows). The intensity of these satellites relative to the main peaks increases with increasing bilayer period (1.5 to 9.0 nm), suggesting an improving layer quality (definiteness) when assuming a constant inter-diffused zone (due to similar deposition conditions). The peaks in between both Bragg reflections for the sample with 9 nm bilayer period as well as those in between the peaks of $\Lambda = 15$ nm are assumed to be superlattice reflections. In order to confirm our adjusted nominal bilayer period, we evaluated the bilayer period using following equation:

$$\sin(\theta)_{\pm} = \sin(\theta)_B \pm \frac{m \cdot \lambda}{2 \cdot \Lambda} \quad (4)$$

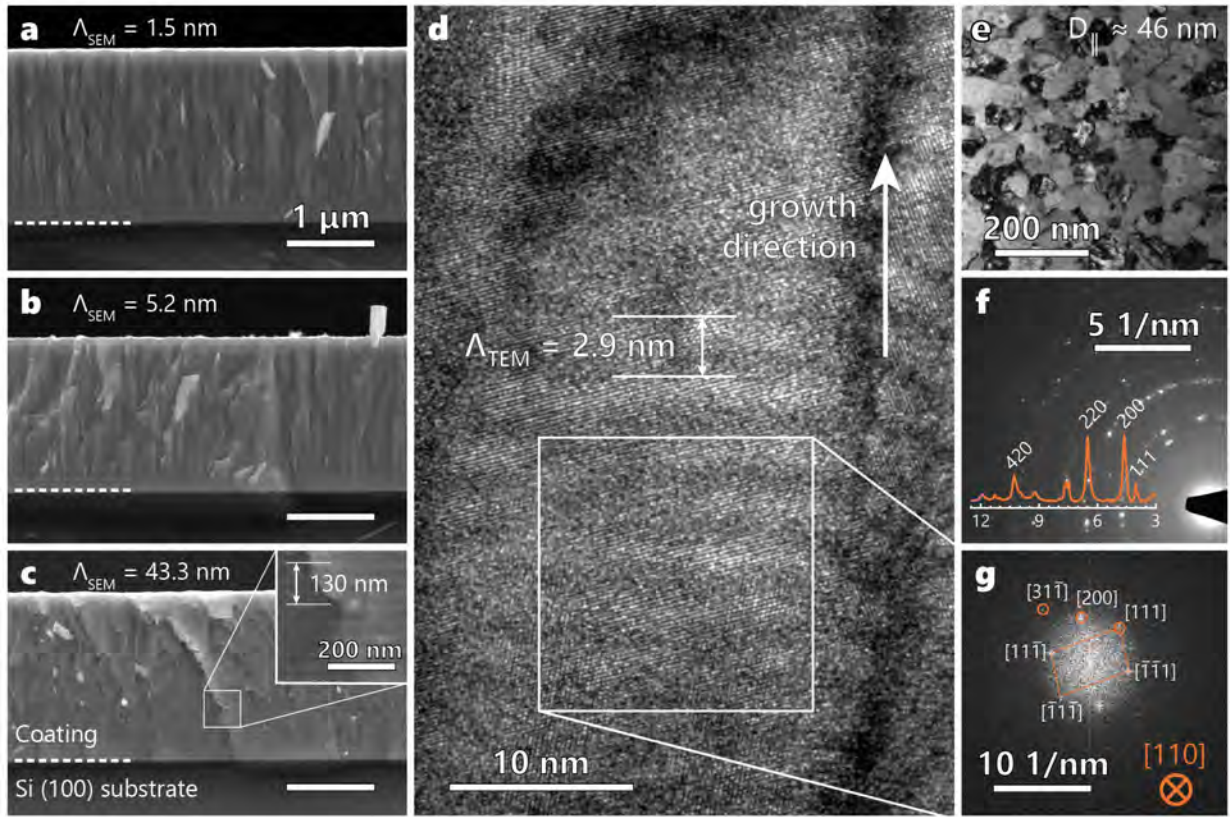


Fig. 2. The SEM-micrographs in (a)-(c) show cross sections of our MoN-TaN coatings with nominal bilayer periods of 1.5, 5.2, and 43.3 nm respectively. The scale bars in (b) and (c) are of equal length to the one in (a). The dashed lines sign the interface between coating and Si (100) substrate. The inset in (c) shows an enlarged view visualizing the layered structure of this coating. The HR-TEM micrograph (d) shows a cross section of the coating with a nominal bilayer period of 3.0 nm. The white marked area was used to generate the FFT pattern in (g) using Gatan Digital Micrograph. The TEM top view in (e) was taken from the sample with $\Lambda=1.5$ nm, the column width was calculated using the linear intercept method. (f) shows a SAED pattern of the region in (e) including an integration of the pattern.

where θ_{\pm} donates the angle of the satellite peak (positive or negative), θ_B the angle of the Bragg peak for the solid solution, m the order of the satellite peak, λ the wavelength of the used x-ray source, and Λ the bilayer period. The results of these calculations given in Table I correlate well with the nominal bilayer periods (also with those calculated by dividing the film thickness by the number of bilayers).

Figure 3(b) shows a quarter of the Debye Scherrer pattern of a $\text{MoN}_{0.5}\text{-TaN}$ superlattice coating with a bilayer period of 5.2 nm grown on austenitic steel. The growth direction of this sample is towards $\phi=0^\circ$. One can therefore identify the textured (200) nature of this sample, also indicated in the Bragg Brentano High Definition (BBHD) laboratory XRD measurements in Fig. 3(a). In order to calculate the corresponding lattice constants in out-of-plane and in in-plane direction we integrated in ϕ direction and fitted this data (using Lorentz-peak-shapes). The corresponding lattice parameters vs. $\sin^2(\phi)$ are

linearly fitted and extrapolated to $\phi=0^\circ$ and 90° . The coefficient of determination was $R^2=0.976$. We found a tetragonal distorted unit cell with a c/a ratio of 1.013. This distortion mostly originates from residual stresses, which are calculated to be -3.8 ± 0.2 GPa using the $\sin^2(\phi)$ method; however, we also calculated a slight unit cell distortion in our *ab initio* simulations stemming from the

Tab. I. Nominal and measured bilayer periods.

Λ_{nom} (nm)	Λ_{SEM} (nm)	Λ_{XRD} (nm)	Λ_{TEM} (nm)
1.5	1.49 ± 0.01	1.40 ± 0.10	-
3.0	2.67 ± 0.01	2.69 ± 0.12	2.9
6.0	5.17 ± 0.04	5.28 ± 0.24	-
9.0	8.32 ± 0.04	8.71 ± 0.62	-
15.0	13.1 ± 0.20	14.0 ± 1.68	-
45.0	43.3 ± 0.06	-	-

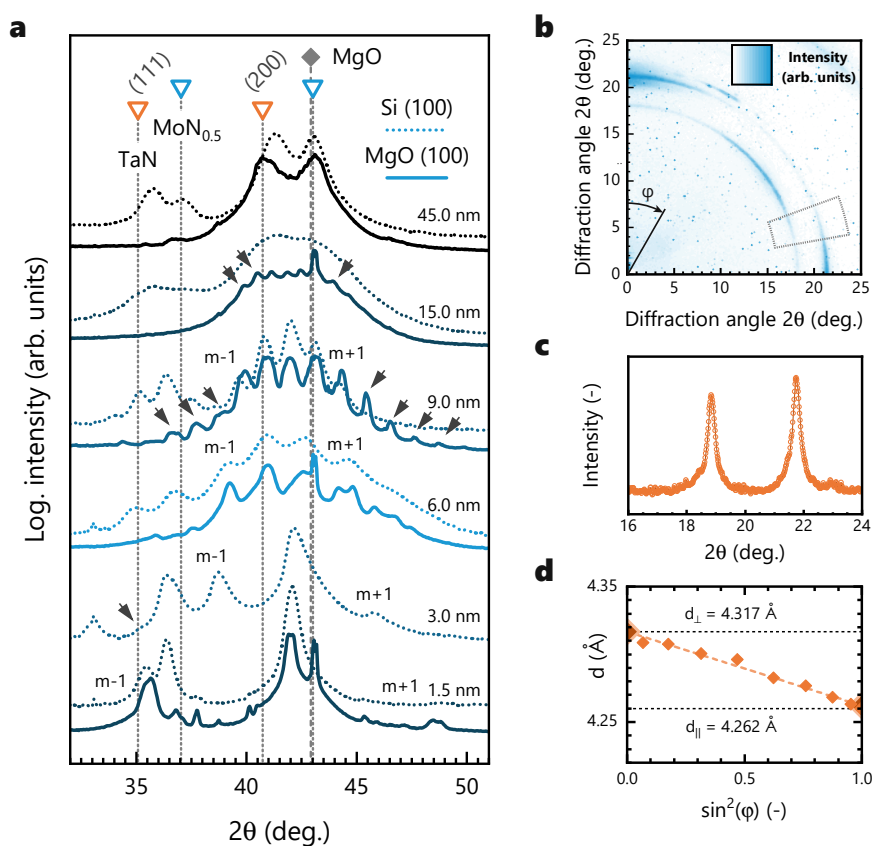


Fig. 3. X-ray diffraction patterns in (a) of our superlattice thin films. The labeling (m+1) and (m-1) and the arrows mark the satellite peaks stemming from the layered structure of our coatings. The solid lines and dashed lines are diffraction patterns of thin films deposited on MgO (100) and Si (100) substrates respectively. The bilayer periods quoted on the right side of (a) are the nominal ones. The intensity plot in (b) shows a quarter of a Debye Scherrer pattern recorded in transmission geometry (sample thickness in beam direction was $\sim 50 \mu\text{m}$) at the nanofocus endstation at the beamline P03 of PETRAIII at Deutsches Elektronen-Synchrotron (DESY). The gray marked area was integrated in ϕ direction and plotted in (c). The plot in (d) shows derived lattice parameters over $\sin^2(\phi)$ and the corresponding linear fit.

superlattice structure and its intrinsic residual stresses on the atomic scale.

These values, as well as the constants derived from nanodiffraction experiments and our BBHD measurements are illustrated in Fig. 4(a). Figure 4(b) shows the unit cell of $\text{MoN}_{0.5}/\zeta\text{-TaN}$ with $\Lambda=1.72 \text{ nm}$. In Fig. 4(a), it is clearly visible that the lattice constants move towards the calculated constituent values with increasing bilayer period (5.2 nm). For larger bilayer periods we observe decreasing lattice constants, well coinciding with our calculations as this decrease indicates a bilayer period depending phase evolution: with increasing bilayer period an epitaxial stabilization of $\zeta\text{-TaN}$ on $\text{MoN}_{0.5}$ becomes energetically less favourable. We propose that a different structural variant of TaN starts to form in TaN layers at the expense of $\zeta\text{-TaN}$ when the bilayer period exceeds some critical level. The possible candidates are $\text{Ta}_{0.75}\text{N}$ or $\text{Ta}_{0.875}\text{N}_{0.875}$, containing vacancies and Schottky defects (i.e., the same amount of vacancies on both Ta and N sublattice), respectively, and being clearly energetically preferred over the stoichiometric TaN. Importantly, both $\text{Ta}_{0.75}\text{N}$ and $\text{Ta}_{0.875}\text{N}_{0.875}$ exhibit a lattice parameter that results in a d_{200} value closely overlapping with the experimental one. Also, the parameters derived from the nanodiffraction experiments are consistent with the *ab initio* calculations.

The hardness and the Young's modulus of our coatings are plotted in Fig. 5(a) and (b). The hardness H shows no significant increase due to the similar shear moduli of $\text{MoN}_{0.5}$, $\zeta\text{-TaN}$, and $c\text{-TaN}$, as the hardness enhancement in superlattices is usually obtained by the hindrance of dislocation movement over the interface due to those differences [52]. Our *ab initio* calculations indicate shear moduli for $\text{MoN}_{0.5}$, $\zeta\text{-TaN}$, and $c\text{-TaN}$ of 124 GPa, 159 GPa and 127 GPa, respectively. The shear moduli of the Schottky defect containing TaN is depending on the vacancy concentration and calculated to be 191 and 121 GPa for $\text{Ta}_{0.75}\text{N}$ and $\text{Ta}_{0.875}\text{N}_{0.875}$ respectively. Nonetheless the indentation hardness is at a reasonable high level, comparable with that of typical physical vapour deposited $\text{Ti}_{1-x}\text{Al}_x\text{N}$.

A relatively large scatter of indentation moduli, from about 375 up to 430 GPa, is measured depending on the bilayer period. While the experimental records above $\sim 6 \text{ nm}$ —slowly saturate from 380 to about 400 GPa (the coating with $\Lambda \sim 45 \text{ nm}$), they show an increase up to $\sim 430 \text{ GPa}$ when approaching $\Lambda=1.7 \text{ nm}$. To take a closer look on this peculiar dependence of our indentation data on the bilayer period, we applied the linear elasticity continuum model by Grimsditch and Nizzoli (cf. Methodology section). Our generalised version of this model allows to calculate the overall elasticity of a SL contain-

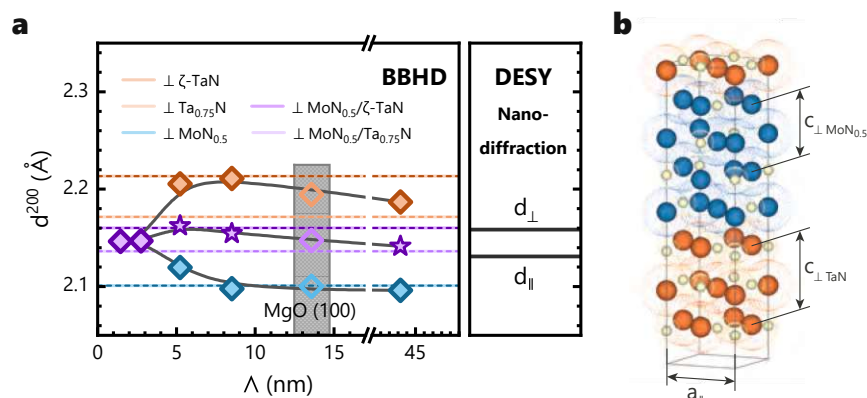


Fig. 4. Diamonds symbols in (a) show the obtained lattice plane distances from the XRD patterns of our superlattices on Si (100) (Fig. 3(a)). An exception is the coating with $\Lambda=13.1$ nm as the polycrystalline and layered nature of the sample did not allow a determination of d_{200} . For comparison we plotted the lattice plane distance obtained from films on the MgO (100) substrate. Data points in stars are obtained by calculating the average. The right side of (a) shows in-plane and out-of-plane lattice plane distances obtained from our synchrotron experiments. In (b) the unit cell of the superlattice with $\Lambda=1.72$ nm is shown.

ing material A and B based on the elastic contributions from the A/B interface layer and the bulk-like A and B layers. Furthermore, both A and B bulk-like layers can possibly contain n sub-layers with different concentration of the respective material to consider, e.g., compositional fluctuations within one material. The bilayer period dependence enters via varying the volume ratio between the interface (of a certain thickness) and the bulk-like layers. Applied to our SL system, the $\text{MoN}_{0.5}/\text{Ta}_{0.75}\text{N}$ SL with $\Lambda=1.7$ nm was supposed to form the interface layer, while the two bulk-like layers were approximated by $\text{rs-MoN}_{0.5}$ and tetragonally distorted ζ -TaN. Figure 5(b) reveals that under such assumptions, the 1.7-5 nm range of the indentation data can be very closely reproduced. On the other hand, the model deviates from the experimental records noticeably when bilayer period exceeds 5 nm, hence suggesting on possible structural transformations in one of the layers (or both). Based on the dependence of the d_{200} spacings on the bilayer period, we proposed a hypothesis that the defect-containing $\text{rs-Ta}_{0.75}\text{N}$ or $\text{rs-Ta}_{0.875}\text{N}_{0.875}$ could form when the TaN layers become too thick to retain the defect-free ζ -TaN. Consequently, the material suspicious from structural transformations was the TaN, well-known for its strong driving force for vacancies/Schottky defects. Specifically, the $\text{rs-Ta}_{0.75}\text{N}$ with 25% of ordered metal vacancies (illustrated as comic in Fig. 5(c)) is the energetically most favourable variant of the cubic TaN [19]. The TaN bulk-like layer of the SL in our Grimsditch-Nizzoli model was therefore divided into two sublayers containing ζ -TaN and a) Schottky-defected TaN or b) $\text{rs-Ta}_{0.75}\text{N}$. When the $\text{rs-Ta}_{0.75}\text{N}$ was implemented in the simulation, we obtained a close overlap between the indentation data and the calculated Young's moduli. Considerations of elastic response thus helped to differentiate between (energetically and structurally close) $\text{rs-Ta}_{0.75}\text{N}$ and $\text{rs-Ta}_{0.875}\text{N}_{0.875}$: we concluded that the presence of the former one in the SL is more likely. Therefore, the decrease of the indentation modulus was ascribed to the decreasing interface density as well as to

the increasing volume fraction of ζ -TaN in the TaN layers. As elasticity of the bulk-like region predominantly contributes to the overall elasticity of the SL at higher bilayer periods (i.e., the interface effects are largely diminished), this leads to the saturation of the indentation modulus towards the average polycrystalline Young's modulus of $\text{rs-MoN}_{0.5}$ and $\text{rs-Ta}_{0.75}\text{N}$.

The micromechanical testing setup with necessary dimensions used to calculate the fracture toughness is exemplarily shown in Fig. 5(d). We gave special attention to the positioning of the spherical indenter tip in order to avoid deviations from mode I load conditions. Figures 5(e) and 5(f) show fracture cross sections of cantilevers after testing. The thin material bridges are visible, as well as the initial notch depth a . The spherical indenter tip accompanies with a reduction of the lever arm l during the micromechanical test. The resulting overall error due to this uncertainty is calculated to be less than 2% (calculated in the framework of Euler-Bernoulli beam theory, also accounting for uncertainties coming with a blunted tip) and is already included in the experimental error. This is justified since a sharp indenter (i.e. Berkovich or cube corner) could possibly lead to unwanted plastic deformation in the contact area, falsifying the outcome by incorrect displacement data, as well as by violations in mode I conditions due to forces in lateral direction (inducing yield stresses in the cross section).

The derived fracture toughness K_{IC} of our MoN/TaN superlattice coatings (Fig. 5(g)) reaches a maximum value of $2.97 \pm 0.21 \text{ MPa}\cdot\text{m}^{\frac{1}{2}}$ at a bilayer period of $\Lambda=5.2$ nm. Compared to TiN/CrN superlattices, we observe higher fracture toughness values (there the maximum was $2.01 \pm 0.18 \text{ MPa}\cdot\text{m}^{\frac{1}{2}}$ at a bilayer period of ~ 6.2 nm) [16]. With increasing bilayer period, we observe a decrease in fracture toughness to $2.32 \pm 0.23 \text{ MPa}\cdot\text{m}^{\frac{1}{2}}$ for 8.3 nm, when Λ is further increased, K_{IC} stays constant at $\sim 2.5 \text{ MPa}\cdot\text{m}^{\frac{1}{2}}$. For decreasing bilayer periods ($\Lambda=1.5$ nm) we see a decrease to $2.30 \pm 0.13 \text{ MPa}\cdot\text{m}^{\frac{1}{2}}$. This progression has been observed in a previous work on superlattices,

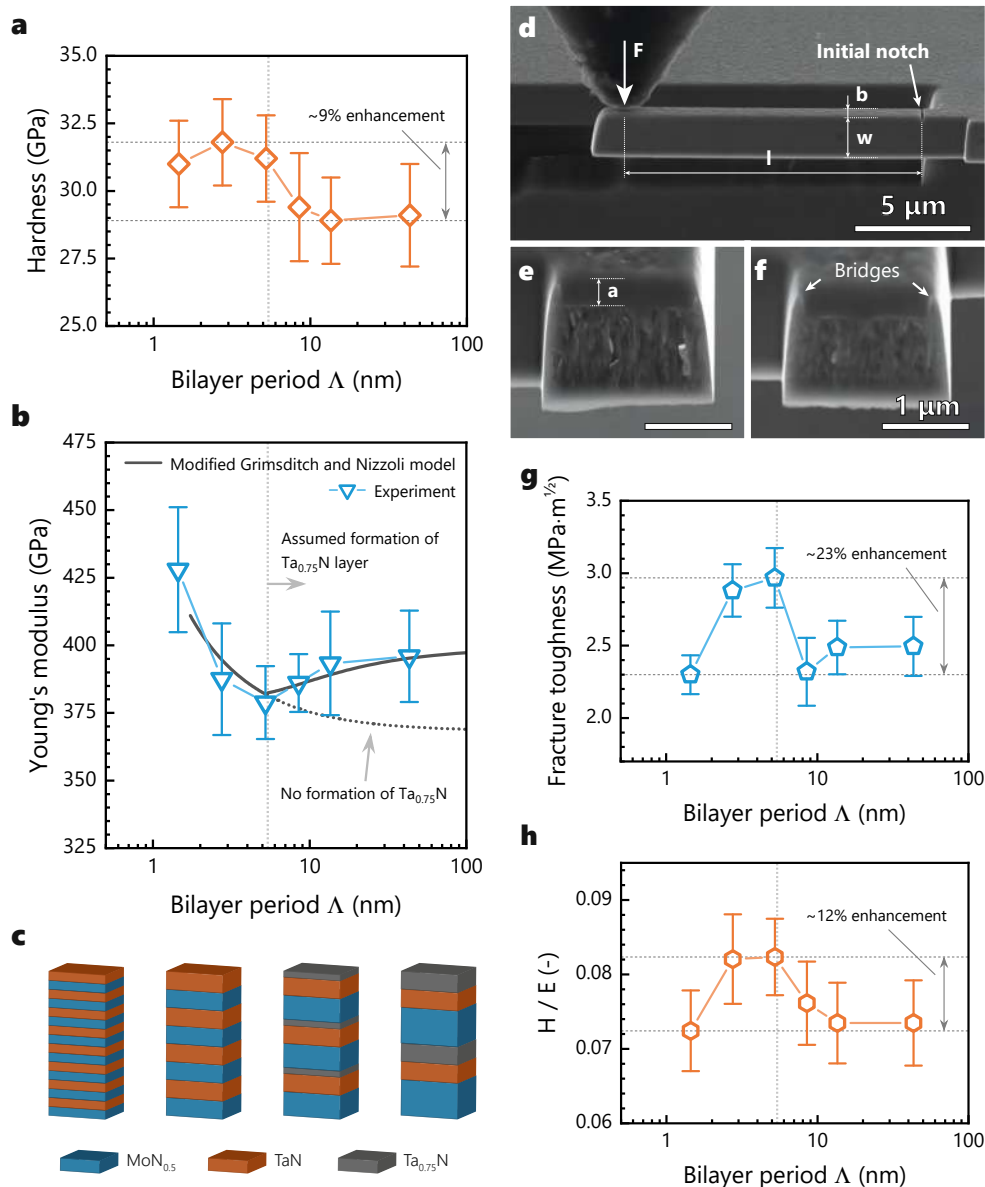


Fig. 5. The hardness as a function of the (log) bilayer period is shown in (a). The vertical dashed line indicates the bilayer period where we assume the formation of a second phase in the TaN layer. The Young's modulus over Λ is shown in (b). Here besides the computational Young's modulus (Grimsditch and Nizzoli) including a second phase in TaN, we also plotted the one without it. The comic in (c) shows the imagined coating architecture. The SEM micrograph (d) shows a cantilever before micromechanical testing in a 10° inclined view including the dimensions of the lever arm l , cantilever width b , cantilever height w , the initial notch, and the point of application of force. The fracture cross sections in (e) and (f) show the depth of the initial notch a ; exemplary marked are the thin bridges necessary for our micromechanical tests. The plots (g) and (h) show the derived fracture toughness K_{IC} and the empirical H/E toughness criteria, respectively.

importantly in this study without significant differences in the shear moduli of its constituents and hence with no substantial hardness increase.

The H/E ratio (Fig. 5(h)), an empirical indication used to describe the toughness of hard coatings also shows an

increase for bilayer periods between 3 and 6 nm. However, it has to be noted that the error bars are overlapping, thus these differences are not significant [53].

To provide an insight into the K_{IC} dependence on the bilayer period, we performed ab initio calculations quanti-

Tab. II. Elastic properties and cleavage properties of the constituents of our superlattices as well as of the superlattice with a bilayer period of 1.72 nm and a Mo-Ta-N disordered (SQS) solid solution. We note that the cleavage properties of the non-cubic (e.g., ζ -TaN) and the defected systems can generally fluctuate depending on the chosen cleavage plane. In accordance to the SL systems, which were cleaved perpendicularly to the interface, the ζ -TaN, was cleaved along the tetragonal c axis. Cleavage data for the cubic but defected systems were averaged based on the results for the distinct cleavage planes in our simulation cell.

Structure	Elastic properties (GPa)					Cleavage properties		
	B	G	E_{poly}	E_{100}	E_{111}	E_c (J/m ²)	σ_c (GPa)	K_{IC} MPa·m ^{1/2}
rs-MoN _{0.5}	300	124	326	399	284	4.0	34.6	2.59
rs-TaN	340	127	338	674	190	-	-	-
ζ -TaN	283	156	396	674	319	5.4	44.4	3.72
rs-Ta _{0.75} N	317	191	479	671	374	3.9	34.6	3.25
rs-Ta _{0.875} N _{0.875}	299	121	319	387	279	-	-	-
SL 1.7 nm	316	160	411	618	330	3.6	32.6	3.00
Mo _{0.5} Ta _{0.5} N	310	110	296	403	238	-	-	-

fying cleavage properties of MoN_{0.5}/TaN SL as well as of the monolithic rs-MoN_{0.5}, ζ -TaN, and rs-Ta_{0.75}N, which were predicted to form in the bulk-like layers of the SL. Specifically, we determined cleavage energy, E_c , which represents the energy to separate a solid material into two blocks, and critical stress, σ_c , which corresponds to the maximum tensile stress perpendicular to the cleavage plane before cleavage happens [54]. In accordance with the experimental procedure, our SLs were cleaved perpendicular to the interfaces. Subsequently, the K_{IC} values were estimated using a simple formula

$$K_{IC} = \sqrt{cE_{hkl}E_c} \quad (5)$$

where E_{hkl} and E_c are the directional Young's modulus and the cleavage energy, respectively, and c is a scaling factor, conventionally set to 4 [55]. Tab. II shows that the E_{100} value of the SL, i.e., the Young's modulus perpendicular to the interface, is 618 GPa, which is close to the 645 and 671 GPa of ζ -TaN, and rs-Ta_{0.75}N, but a way above the rs-MoN_{0.5}, which yields $E_{100} \sim 389$ GPa. All the cleavage stresses are found within a close range, 33-35 GPa. The cleavage energies, however, vary quite significantly between 3.6 J/m² (SL) and 5.4 J/m² (ζ -TaN). According to the predicted K_{IC} values, crack propagation is the easiest in the case of MoN_{0.5} yielding $K_{IC} \sim 2.59$ MPa·m^{1/2}. The 2.99 MPa·m^{1/2} obtained for the 1.72 nm SL suggests, that the interface is slightly stronger, but does not exceed the K_{IC} values of both the ζ -TaN, and rs-Ta_{0.75}N.

IV. DISCUSSION

Using *ab initio* calculations to predict material properties has been proven to serve as a powerful tool in materials science. Our calculated elastic constants and

their comparison with literature values clearly indicate a trend towards increased ductility for MoN_{0.5}/TaN superlattice coatings, not only compared to its constituents, also compared to a solid solution of MoN_{0.5} and TaN. Furthermore, we could identify TaN based layers (both, ζ -TaN and Ta_{0.75}N) as the stronger constituents in terms of cleavage energy in the MoN-TaN superlattice system. The calculated cleavage stresses are within the same range between 33 and 35 GPa. Based on this calculated behaviour, we deposited MoN_{0.5}/TaN superlattice coatings with various bilayer periods. Thereby, different coatings including various phases could be identified. Importantly, our introduced architecture (Fig. 5(c)) – including an epitaxially stabilized tetragonal distorted ζ -TaN up to ~ 2.5 nm layer thickness, and a thereon growing Ta_{0.75}N – could be confirmed so far by comparing calculated lattice constants and elastic properties with x-ray diffraction experiments and the Young's moduli derived from nanoindentation respectively.

Our thin films possess sharp interfaces, recognisable in the XRD pattern showing multiple satellite reflections, even for a nominal bilayer period of 1.5 nm. Besides that, we were able to confirm calculated lattice parameter also for MoN_{0.5}. For 1.5 and 3.0 nm bilayer we observed just one peak in out-of-plane direction which can be explained by the increasing interface-influenced regions (strained unit cells due to lattice mismatch) with decreasing bilayer period.

Usually superlattice coatings with such good interface qualities achieve hardness values outperforming their constituents by up to 100%. As discussed and explained before we do not observe such a significant increase. Importantly though, we observe a clear peak in fracture toughness, what gives rise to an interesting question: what is the origin of this increase?

The fact that the experimental K_{IC} increases with bilayer period, peaks at about 5 nm and then decreases again

can be partially interpreted via compositional and structural changes within TaN layers of the SL. As the $K_{IC} \sim 3.72 \text{ MPa}\cdot\text{m}^{\frac{1}{2}}$ of ζ -TaN exceeds both the MoN_{0.5}/TaN interface and the rs-MoN_{0.5} layers, the overall K_{IC} increases with bilayer period, since larger volume fractions of ζ -TaN are stabilised as compared to the diminishing volume fraction of the interfaces. The drop of K_{IC} above $\sim 5 \text{ nm}$ might origin from the vacancy formation in TaN layers, leading to the rs-TaN_{0.75} with $K_{IC} \sim 3.25 \text{ MPa}\cdot\text{m}^{\frac{1}{2}}$. The real picture, of course, is much more complex, meaning that the ζ -phase formation is only one possible contributing factor to the observed K_{IC} evolution: in Ref. [16], we studied the fracture toughness of TiN/CrN SL films and found a pronounced dependence of K_{IC} as a function of the bilayer period. We proposed several mechanisms that could explain this behaviour. These were: coherency strains; misfit dislocation arrays at the interface; spatially oscillating elastic moduli influencing crack growth; average grain size influenced by Λ . The MoN/TaN SL system of the present study is an interesting model system as it essentially allows to study the effect of large coherency stresses on K_{IC} while having a less significant effect of pronounced ΔG of the layer materials (the difference at the peak position was calculated to be 32 GPa). For comparison, differences in other well-studied SL systems are in the order of ~ 50 to 90 GPa [16, 36, 56, 57]. The average grain size is also neglectable as our coatings possess a similar column diameter of $\sim 50 \text{ nm}$.

The resulting strains from the lattice mismatch of $\sim 5\%$ and their residual stresses can reach amounts comparably high with growth related or thermal expansion related stresses. Assuming a difference in lattice constants of $\Delta a = 0.225 \text{ \AA}$ (MoN_{0.5} and ζ -TaN), and an interface width of one unit cell (4 planes of each, nitrogen and metal, and thus 5 transitions with a change in lattice parameter) a total difference of 0.045 \AA results in a coherency strain ϵ_c of $\sim 1\%$ which gives us residual stresses of $\sim 3.3 \text{ GPa}$ both tensile and compressive surrounding every interface of MoN_{0.5} and ζ -TaN. These stresses have to be overcome during cleavage, thus they effectively enhance the measured fracture toughness.

V. CONCLUSIONS

The concept of enhanced mechanical properties due to superlattices architectures has been shown in multiple studies. Together with an increased hardness, the fracture toughness of protective coatings is of particular importance. We deposited MoN-TaN superlattice coatings, characterized them by means of density functional theory calculations, x-ray diffraction, and mechanical testing, coming to following conclusion: the constituents of the MoN-TaN superlattice system are – when deposited by physical vapour deposition – present in the MoN_{0.5} and ζ -TaN, Ta_{0.75}N, phases. The latter depends on individual layer thickness: we observe a change at a layer thickness of $\sim 2.5 \text{ nm}$ TaN. This was observed by two dif-

ferent methods: first our XRD measurements confirm this trend as the peak position of the TaN layer shifts to higher 2θ angles with increasing bilayer periods as a result of increasing Ta_{0.75}N proportion. Second, the progression of the Young's modulus follows a calculation including the Ta_{0.75}N phases after an initial grow of $\sim 2.5 \text{ nm}$ ζ -TaN instead of the calculation without it. We calculated an intrinsic higher fracture toughness for ζ -TaN compared to Ta_{0.75}N as a part of an increase in K_{IC} . Another mechanism active in this superlattice coatings is coherency stresses which have to be overcome. This increase in K_{IC} was also observed in micromechanical experiments.

ACKNOWLEDGEMENTS

The authors acknowledge the financial support by the Austrian Federal Ministry of Economy, Family and Youth and the National Foundation for Research, Technology and Development. We also thank for the financial support of Plansee Composite Materials GmbH, and Oerlikon Surface Solutions AG. The computational results were achieved using the Vienna Scientific Cluster (VSC), X-ray diffraction studies were performed at the X-ray center of TU Wien (XRC), SEM and TEM work was performed using facilities of the USTEM at TU Wien. We also thank the Institute for Mechanics of Materials and Structures of TU Wien for providing the PI85-SEM indenter. We further acknowledge the granted use of the Nanofocus Endstation of the Beamline P03 of PETRAIII at DESY, a member of the Helmholtz Association (HGF). NK acknowledges the DOC fellowship from the Austrian Academy of Sciences.

REFERENCES

- [1] P. H. Mayrhofer, C. Mitterer, L. Hultman, and H. Clemens, *Progress in Materials Science* **51**, 1032 (2006).
- [2] A. Inspektor and P. A. Salvador, *Surface and Coatings Technology* **257**, 138 (2014).
- [3] T. Glechner, P. H. Mayrhofer, D. Holec, S. Fritze, E. Lewin, V. Paneta, D. Primetzhofer, S. Kolozsvári, and H. Riedl, *Scientific Reports* **8**, 17669 (2018).
- [4] V. Moraes, C. Fuger, V. Paneta, D. Primetzhofer, P. Polcik, H. Bolvardi, M. Arndt, H. Riedl, and P. H. Mayrhofer, *Scripta Materialia* **155**, 5 (2018).
- [5] Y. X. Xu, H. Riedl, D. Holec, L. Chen, Y. Du, and P. H. Mayrhofer, *Surface and Coatings Technology* **324**, 48 (2017).
- [6] G. Dehm, B. N. Jaya, R. Raghavan, and C. Kirchlechner, *Acta Materialia* **142**, 248 (2018).
- [7] B. N. Jaya, C. Kirchlechner, and G. Dehm, *Journal of Materials Research* **30**, 686 (2015).
- [8] J. Ast, M. Ghidelli, K. Durst, M. Göken, M. Sebastiani, and A. Korsunsky, *Materials & Design* **173**, 107762 (2019).
- [9] B. Lawn, *Fracture of brittle solids* (Cambridge University Press, Cambridge, 1993).
- [10] S. Zhang, D. Sun, Y. Fu, and H. Du, *Surface and Coatings Technology* **198**, 2 (2005).
- [11] M. Bartosik, C. Rumeau, R. Hahn, Z. L. Zhang, and P. H. Mayrhofer, *Scientific Reports* (2017), 10.1038/s41598-017-16751-1.
- [12] R. Hahn, M. Bartosik, M. Arndt, P. Polcik, and P. Mayrhofer, *International Journal of Refractory Metals and Hard Materials* (2017), 10.1016/j.ijrmhm.2017.11.008.
- [13] C. Fuger, V. Moraes, R. Hahn, H. Bolvardi, P. Polcik, H. Riedl, and P. H. Mayrhofer, *MRS Communications*, 1 (2019).
- [14] M. Bartosik, R. Hahn, Z. Zhang, I. Ivanov, M. Arndt, P. Polcik, and P. Mayrhofer, *International Journal of Refractory Metals and Hard Materials* **72**, 78 (2018).
- [15] R. Daniel, M. Meindlhumer, J. Zalesak, B. Sartory, A. Zeilinger, C. Mitterer, and J. Keckes, *Materials & Design* **104**, 227 (2016).
- [16] R. Hahn, M. Bartosik, R. Soler, C. Kirchlechner, G. Dehm, and P. H. Mayrhofer, *Scripta Materialia* (2016), 10.1016/j.scriptamat.2016.06.030.
- [17] D. G. Sangiovanni, V. Chirita, and L. Hultman, *Physical Review B* **81**, 104107 (2010).
- [18] N. Koutná, P. Řehák, Z. Chen, M. Bartosik, M. Fallmann, M. Černý, Z. Zhang, M. Friák, M. Šob, P. H. Mayrhofer, and D. Holec, *Scripta Materialia* **165**, 159 (2019).
- [19] N. Koutná, D. Holec, O. Svoboda, F. F. Klimashin, and P. H. Mayrhofer, *Journal of Physics D: Applied Physics* **49**, 375303 (2016).
- [20] U. Helmersson, S. Todorova, S. A. Barnett, J. Sundgren, L. C. Markert, and J. E. Greene, *Journal of Applied Physics* **62**, 481 (1987).
- [21] X. Chen, Y. Du, and Y.-W. Chung, *Thin Solid Films* (2019), 10.1016/J.TSF.2019.04.040.
- [22] G. Kresse and J. Furthmüller, *Computational Materials Science* (1996), 10.1016/0927-0256(96)00008-0, arXiv:0927-0256(96)00008 [10.1016].
- [23] G. Kresse and D. Joubert, *Physical Review B* **59**, 1758 (1999).
- [24] W. Kohn and L. Sham, *Physical Review* **385** (1965), 10.1103/PhysRev.140.A1133, arXiv:PhysRev.140.A1133 [10.1103].
- [25] J. P. Perdew, K. Burke, and M. Ernzerhof, *Physical Review Letters* **77**, 3865 (1996).
- [26] S.-H. Wei, L. G. Ferreira, J. E. Bernard, and A. Zunger, *Physical Review B* **42**, 9622 (1990).
- [27] F. Birch, *Physical Review* **71**, 809 (1947).
- [28] Y. Le Page and P. Saxe, *Physical Review B* **65**, 1 (2002).
- [29] Y. Le Page and P. Saxe, *Physical Review B - Condensed Matter and Materials Physics* **63**, 1 (2001).
- [30] R. Yu, J. Zhu, and H. Q. Ye, *Computer Physics Communications* **181**, 671 (2010).
- [31] M. Moakher and A. N. Norris, *Journal of Elasticity* **85**, 215 (2006).
- [32] A. Reuss, *ZAMM - Zeitschrift für Angewandte Mathematik und Mechanik* **9**, 49 (1929).
- [33] W. Voigt, *Lehrbuch der Kristallphysik*, edited by B. Teubner and J. Edwards (Vieweg+Teubner Verlag, Leipzig Berlin, Ann Arbor, Mich., 1928) p. 979.
- [34] J. F. Nye, *Physical properties of crystals : their representation by tensors and matrices* (Oxford University Press, 1985) p. 329.
- [35] M. Grimsditch and F. Nizzoli, *Physical Review B* **33**, 1 (1986).
- [36] J. Buchinger, N. Koutná, Z. Chen, Z. Zhang, P. H. Mayrhofer, D. Holec, and M. Bartosik, *Acta Materialia* **172**, 18 (2019).
- [37] P. Lazar, J. Redinger, and R. Podloucky, *Physical Review B* **76**, 174112 (2007).
- [38] P. Řehák, M. Černý, and D. Holec, *Surface and Coatings Technology* **325**, 410 (2017).
- [39] L. Giannuzzi and F. Stevie, *Micron* **30**, 197 (1999).
- [40] J. Keckes, M. Bartosik, R. Daniel, C. Mitterer, G. Maier, W. Ecker, J. Vila-Comamala, C. David, S. Schoeder, and M. Burghammer, *Scripta Materialia* **67**, 748 (2012).
- [41] A. C. Fischer-Cripps, *Nanoindentation*, 3rd ed., Mechanical Engineering Series (Springer New York, New York, NY, 2011) p. 282.
- [42] W. C. Oliver and G. M. Pharr, *Journal of Materials Research* **7**, 1564 (1992), arXiv:arXiv:1303.2632v1.
- [43] J. Menčík, D. Munz, E. Quandt, E. R. Weppelmann, and M. V. Swain, *Journal of Materials Research* **12**, 2475 (1997).
- [44] S. Brinckmann, K. Matoy, C. Kirchlechner, and G. Dehm, *Acta Materialia* **136**, 281 (2017).
- [45] K. Matoy, H. Schönherr, T. Detzel, T. Schöberl, R. Pippan, C. Motz, and G. Dehm, *Thin Solid Films* **518**, 247 (2009).
- [46] S. Pugh, *The London, Edinburgh, and Dublin Philosophical Magazine and Journal of Science* **45**, 823 (1954).
- [47] I. Frantsevich, F. Voronov, and S. Bokuta, *Elastic Constants and Elastic Moduli of Metals and Insulators Handbook* (Naukova Dumka, Kiev, 1983) pp. 60–120.
- [48] H. Niu, X.-Q. Chen, P. Liu, W. Xing, X. Cheng, D. Li,

- and Y. Li, *Scientific Reports* **2**, 718 (2012).
- [49] J. Hilliard, *Metal Progress* **85**, 99 (1964).
- [50] C. Gammer, C. Mangler, C. Rentenberger, and H. Karnthaler, *Scripta Materialia* **63**, 312 (2010).
- [51] F. F. Klimashin, N. Koutná, H. Euchner, D. Holec, and P. H. Mayrhofer, *Journal of Applied Physics* (2016), 10.1063/1.4966664.
- [52] X. Chu and S. A. Barnett, *Journal of Applied Physics* **77**, 4403 (1995).
- [53] X. Chen, Y. Du, and Y. W. Chung, *Thin Solid Films*, 0 (2019).
- [54] N. Koutná, P. Řehák, Z. Chen, M. Bartosik, M. Fallmann, M. Černý, Z. Zhang, M. Friák, M. Šob, P. H. Mayrhofer, and D. Holec, *Scripta Materialia* **165**, 159 (2019).
- [55] M. Bielawski and K. Chen, *Journal of Engineering for Gas Turbines and Power* **133**, 042102 (2010).
- [56] P. E. Hovsepian, A. Ehiasarian, Y. Purandare, P. Mayr, K. Abstoss, M. Mosquera Feijoo, W. Schulz, A. Kranzmann, M. Lasanta, and J. Trujillo, *Journal of Alloys and Compounds* **746**, 583 (2018).
- [57] M. Schlögl, C. Kirchlechner, J. Paulitsch, J. Keckes, and P. H. Mayrhofer, *Scripta Materialia* (2013), 10.1016/j.scriptamat.2013.01.039.

APPENDIX

Tab. A-I. Theoretical and experimental determined elastic constants of several transition metal nitrides, carbides, oxides, and borides found in literature. Here the nitrides, the carbides, and the oxides have a cubic structure (space group 225) if differently the space group is written in brackets next to the composition. Diboride structures are written before the composition, α and ω for space group 191 and 194 respectively.

Composition	Ref.	c ₁₁	c ₁₂	c ₁₃	c ₃₃	c ₄₄	c ₆₆
Nitrides							
NbN	[1]	739	161	-	-	76	-
NbN	[1]	608	134	-	-	117	-
NbN	[2]	649	136	-	-	80	-
NbN	[3]	692	141	-	-	143	-
NbN	[4]	685	121	-	-	79	-
NbN	[5]	722	108	-	-	88	-
TiMoN	[6]	573	191	-	-	145	-
CeN	[7]	329	70	-	-	61	-
CeN	[7]	310	83	-	-	73	-
TiWN	[6]	574	155	-	-	132	-
Zr ₃ N ₄	[8]	454	165	-	-	146	-
Zr ₃ N ₄	[8]	374	141	-	-	139	-
ZrN	[3]	462	141	-	-	143	-
ZrN	[2]	523	111	-	-	116	-
ZrN	[5]	563	101	-	-	122	-
ZrN	[4]	521	114	-	-	110	-
AlN	[9]	328	139	-	-	133	-
AlN	[9]	346	146	-	-	167	-
AlN	[2]	418	169	-	-	308	-
Hf ₃ N ₄	[8]	493	167	-	-	152	-
Hf ₃ N ₄	[8]	399	143	-	-	145	-
HfN	[2]	588	113	-	-	120	-
HfN	[4]	580	116	-	-	114	-
HfN	[10]	705	112	-	-	131	-
TiN	[11]	625	165	-	-	163	-
TiN	[6]	713	133	-	-	166	-
TiN	[11]	680	130	-	-	171	-
TiN	[12]	596	125	-	-	155	-
TiN	[11]	688	124	-	-	171	-
TiN	[6]	671	106	-	-	166	-
TiN	[2]	575	130	-	-	163	-
TiN	[13]	561	122	-	-	160	-
TiN	[4]	585	122	-	-	163	-
HfN	[11]	679	119	-	-	150	-
TiCrN	[6]	649	124	-	-	160	-
TiVN	[6]	575	124	-	-	159	-
TiAlN	[6]	504	143	-	-	174	-
TiNbN	[6]	592	103	-	-	147	-
ScN	[14]	397	131	-	-	170	-
ScN	[2]	388	106	-	-	166	-
TiZrN	[6]	594	85	-	-	147	-
YN	[15]	310	81	-	-	124	-
YN	[2]	318	81	-	-	124	-
YN	[5]	319	84	-	-	122	-
Si ₃ N ₄	[11]	504	177	-	-	317	-
Si ₃ N ₄	[11]	529	169	-	-	334	-

Composition	Ref.	c ₁₁	c ₁₂	c ₁₃	c ₃₃	c ₄₄	c ₆₆
c-BN	[11]	825	193	-	-	475	-
c-BN	[11]	820	190	-	-	480	-
c-BN	[11]	783	172	-	-	444	-
VN	[2]	660	144	-	-	120	-
VN	[4]	581	183	-	-	123	-
CrN	[16]	524	113	-	-	118	-
CrN	[4]	572	209	-	-	6	-
CrN	[17]	580	210	-	-	8	-
GaN (186)	[18]	344	134	-	-	90	-
RhN	[3]	462	198	-	-	56	-
PdN	[3]	345	178	-	-	50	-
AgN	[3]	231	120	-	-	30	-
LaN	[2]	198	86	-	-	71	-
TaN	[2]	715	138	-	-	60	-
TaN	[4]	750	122	-	-	62	-
TaN	[13]	901	109	-	-	60	-
TaN	[10]	827	156	-	-	73	-
WN ₂ (123)	[19]	853	122	-	-	203	-
PtN	[3]	285	223	-	-	45	-
Carbides							
NbC	[20]	620	200	-	-	150	-
NbC	[20]	640	180	-	-	140	-
NbC	[21]	604	146	-	-	179	-
NbC _{0.9}	[22]	413	111	-	-	206	-
NbC _{0.865}	[22]	566	117	-	-	153	-
TaC	[23]	505	73	-	-	79	-
TaC	[24]	641	146	-	-	156	-
TaC	[24]	621	155	-	-	167	-
VC	[25]	578	147	-	-	176	-
VC	[26]	783	131	-	-	196	-
VC _{0.83}	[22]	366	110	-	-	192	-
TiC	[27]	610	124	-	-	173	-
TiC	[27]	527	112	-	-	159	-
TiC	[23]	500	113	-	-	175	-
TiC	[27]	513	106	-	-	178	-
TiC	[27]	470	97	-	-	167	-
TiC	[28]	472	99	-	-	159	-
TiC	[22]	418	89	-	-	217	-
TiC	[29]	507	121	-	-	172	-
TiMoC	[27]	596	113	-	-	176	-
TiTaC	[27]	574	119	-	-	180	-
TiNbC	[27]	560	116	-	-	176	-
TiZrC	[27]	508	103	-	-	157	-
TiVC	[27]	549	115	-	-	177	-
TiHfC	[27]	517	103	-	-	165	-
ZrC	[30]	470	100	-	-	160	-
ZrC	[30]	472	99	-	-	159	-
ZrC	[23]	472	99	-	-	159	-
ZrC	[30]	499	93	-	-	170	-
ZrC	[30]	504	90	-	-	173	-
ZrC	[31]	441	60	-	-	151	-
ZrC	[29]	452	107	-	-	155	-
ZrC	[32]	462	102	-	-	154	-
TiCrC	[27]	443	98	-	-	161	-
SiC	[31]	352	140	-	-	233	-
MoC	[33]	625	181	-	-	118	-
HfC	[29]	527	107	-	-	160	-

Composition	Ref.	c ₁₁	c ₁₂	c ₁₃	c ₃₃	c ₄₄	c ₆₆
Oxides							
Y ₂ O ₃	[11]	214	113	-	-	72.6	-
Y ₂ O ₃	[11]	241.9	128	-	-	85	-
Y ₂ O ₃	[11]	224	112	-	-	75	-
Y ₂ O ₃	[31]	227	138	-	-	69	-
Y ₂ O ₃ (206)	[34]	243	126	-	-	85	-
Sc ₂ O ₃	[31]	290	151	-	-	89	-
ScO	[35]	249	138	-	-	138	-
ZrO ₂	[36]	499	111	-	-	63	-
ZrO ₂	[36]	417	82	-	-	47	-
ZrO ₂	[36]	455	64	-	-	63	-
ZrO ₂	[37]	520	93	-	-	61	-
ZrO ₂ (215)	[38]	515	101	-	-	65	-
MgO	[31]	294	93	-	-	155	-
MgO	[23]	297	95	-	-	156	-
MgO	[11]	291	92	-	-	156	-
MgO	[11]	276	86	-	-	149	-
TiO ₂ (62)	[39]	619	218	-	-	52	-
VO	[35]	273	210	-	-	210	-
CrO	[35]	269	188	-	-	188	-
MnO	[35]	227	116	-	-	78	-
CoO	[35]	260	145	-	-	82	-
NiO	[35]	225	95	-	-	110	-
Cu ₂ O	[22]	121	105	-	-	12	-
ReO ₃ (62)	[22]	479	-7	-	-	61	-
Borides							
α-CoB ₂	[40]	515	210	131	286	61	153
α-CrB ₂	[40]	563	135	57	366	163	214
ω-CrB ₂	[40]	572	115	84	591	230	229
α-FeB ₂	[40]	441	201	158	136	101	120
ω-FeB ₂	[40]	486	139	129	306	173	174
α-HfB ₂	[40]	591	50	88	412	261	271
ω-HfB ₂	[40]	405	102	81	449	120	152
α-MnB ₂	[40]	457	233	211	182	155	112
ω-MnB ₂	[40]	475	154	155	470	209	160
α-MoB ₂	[40]	599	123	167	410	138	238
ω-MoB ₂	[40]	567	117	127	620	221	225
α-NbB ₂	[40]	570	97	158	370	217	236
ω-NbB ₂	[40]	544	117	97	581	239	213
ω-NiB ₂	[40]	396	152	111	260	68	122
α-ScB ₂	[40]	492	35	41	342	185	228
ω-ScB ₂	[40]	344	43	82	0	38	150
α-TaB ₂	[40]	578	125	169	385	209	226
ω-TaB ₂	[40]	558	115	95	586	247	221
α-TcB ₂	[40]	570	179	118	460	52	195
ω-TcB ₂	[40]	526	136	139	548	135	195
α-TiB ₂	[40]	638	59	75	392	256	289
ω-TiB ₂	[40]	491	138	87	527	156	176
α-VB ₂	[40]	662	109	94	426	223	277
ω-VB ₂	[40]	538	89	92	514	236	225
α-WB ₂	[40]	596	143	194	365	121	226
ω-WB ₂	[40]	651	170	190	680	252	240
α-YB ₂	[40]	353	49	52	312	157	152
α-ZnB ₂	[40]	358	157	40	229	1	100
α-ZrB ₂	[40]	548	43	89	384	246	252
ω-ZrB ₂	[40]	359	100	81	414	84	129

REFERENCES – TABLE A-I

- [1] X.-J. Chen, V. V. Struzhkin, Z. Wu, M. Somayazulu, J. Qian, S. Kung, A. N. Christensen, Y. Zhao, R. E. Cohen, H.-k. Mao, and R. J. Hemley, *Proc. Natl. Acad. Sci. U. S. A.* **102**, 3198 (2005).
- [2] D. Holec, M. Friák, J. Neugebauer, and P. H. Mayrhofer, *Phys. Rev. B* **85**, 064101 (2012).
- [3] W. Chen and J. Jiang, *J. Alloys Compd.* **499**, 243 (2010).
- [4] Z.-G. Mei, S. Bhattacharya, and A. M. Yacout, *Surf. Coatings Technol.* **357**, 903 (2019).
- [5] E. Zhao, J. Wang, J. Meng, and Z. Wu, *Comput. Mater. Sci.* **47**, 1064 (2010).
- [6] K. Chen, L. R. Zhao, J. Rodgers, and J. S. Tse, *J. Phys. D. Appl. Phys.* **36**, 2725 (2003).
- [7] V. Kanchana, G. Vaitheeswaran, X. Zhang, Y. Ma, A. Svane, and O. Eriksson, *Phys. Rev. B* **84**, 205135 (2011).
- [8] M. Mattesini, R. Ahuja, and B. Johansson, *Phys. Rev. B* **68**, 184108 (2003).
- [9] R. Marmalyuk, K. Akchurin, and V. A. Gorbylev, *Inorg. Mater.* **34**, 691 (1998).
- [10] S. Patil, N. Mangale, S. Khare, and S. Marsillac, *Thin Solid Films* **517**, 824 (2008).
- [11] H. Yao, L. Ouyang, and W.-Y. Ching, *J. Am. Ceram. Soc.* **90**, 3194 (2007).
- [12] V. Podgursky, *J. Phys. D. Appl. Phys.* **40**, 4021 (2007).
- [13] P. Djemia, M. Benhamida, K. Bouamama, L. Belliard, D. Faurie, and G. Abadias, *Surf. Coatings Technol.* **215**, 199 (2013).
- [14] M. Mattesini, M. Magnuson, F. Tasnádi, C. Höglund, I. A. Abrikosov, and L. Hultman, *Phys. Rev. B* **79**, 125122 (2009).
- [15] A. Hao, X. Yang, X. Wang, R. Yu, X. Liu, W. Xin, and R. Liu, *Comput. Mater. Sci.* **48**, 59 (2010).
- [16] L. Zhou, D. Holec, and P. H. Mayrhofer, *J. Appl. Phys.* **113**, 043511 (2013).
- [17] L. Zhou, F. Körmann, D. Holec, M. Bartosik, B. Grabowski, J. Neugebauer, and P. H. Mayrhofer, *Phys. Rev. B* **90**, 184102 (2014).
- [18] S. Zhang, D. Holec, W. Y. Fu, C. J. Humphreys, and M. A. Moram, *J. Appl. Phys.* **114**, 133510 (2013).
- [19] X. P. Du, Y. X. Wang, and V. Lo, *Phys. Lett. A* **374**, 2569 (2010).
- [20] J. Chen, L. L. Boyer, H. Krakauer, and M. J. Mehl, *Phys. Rev. B* **37**, 3295 (1988).
- [21] L. Wu, Y. Wang, Z. Yan, J. Zhang, F. Xiao, and B. Liao, *J. Alloys Compd.* **561**, 220 (2013).
- [22] D. F. Nelson, ed., *Second and Higher Order Elastic Constants*, Landolt-Börnstein - Group III Condensed Matter, Vol. 29a (Springer-Verlag, Berlin/Heidelberg, 1992).
- [23] J. R. Rumble, D. R. Lide, and T. J. Bruno, *CRC handbook of chemistry and physics : a ready-reference book of chemical and physical data*.
- [24] F. Peng, L. Han, H. Fu, and X. Cheng, *Phys. status solidi* **246**, 1590 (2009).
- [25] H. Liu, J. Zhu, Y. Liu, and Z. Lai, *Mater. Lett.* **62**, 3084 (2008).
- [26] W. Wolf, R. Podloucky, T. Antretter, and F. D. Fischer, *Philos. Mag. B* **79**, 839 (1999).
- [27] K. Chen and L. Zhao, *J. Phys. Chem. Solids* **68**, 1805 (2007).
- [28] R. Chang and L. J. Graham, *J. Appl. Phys.* **37**, 3778 (1966).
- [29] H. Li, L. Zhang, Q. Zeng, K. Guan, K. Li, H. Ren, S. Liu, and L. Cheng, *Solid State Commun.* **151**, 602 (2011).
- [30] H. Fu, W. Peng, and T. Gao, *Mater. Chem. Phys.* **115**, 789 (2009).
- [31] A. G. Every, D. F. Nelson, K.-H. Hellwege, H. Landolt, R. Börnstein, and O. Madelung, *Landolt-Börnstein Zahlenwerte und Funktionen aus Naturwissenschaften und Technik: Neue Serie* (Springer, 1992).
- [32] A. Hao, T. Zhou, Y. Zhu, X. Zhang, and R. Liu, *Mater. Chem. Phys.* **129**, 99 (2011).
- [33] Y. Liu, Y. Jiang, J. Feng, and R. Zhou, *Phys. B Condens. Matter* **419**, 45 (2013).
- [34] X. Zhang, W. Gui, and Q. Zeng, *Ceram. Int.* **43**, 3346 (2017).
- [35] G. V. Lewis and C. R. A. Catlow, *J. Phys. C Solid State Phys.* **18**, 1149 (1985).
- [36] J. E. Lowther, *Phys. Rev. B* **73**, 134110 (2006).
- [37] Y. Zhang, H.-X. Chen, L. Duan, J.-B. Fan, L. Ni, and V. Ji, *J. Alloys Compd.* **749**, 283 (2018).
- [38] G. Cousland, X. Cui, A. Smith, A. Stampfl, and C. Stampfl, *J. Phys. Chem. Solids* **122**, 51 (2018).
- [39] M. A. Caravaca, J. C. Miño, V. J. Pérez, R. A. Casali, and C. A. Ponce, *J. Phys. Condens. Matter* **21**, 015501 (2009).
- [40] V. Moraes, H. Riedl, C. Fuger, P. Polcik, H. Bolvardi, D. Holec, and P. H. Mayrhofer, *Sci. Rep.* (2018), 10.1038/s41598-018-27426-w.

Publication VI



Fracture toughness and structural evolution in the TiAlN system upon annealing

M. Bartosik, C. Rumeau, R. Hahn, Z. L. Zhang, and P. H. Mayrhofer

SCIENTIFIC REPORTS

OPEN

Fracture toughness and structural evolution in the TiAlN system upon annealing

M. Bartosik¹, C. Rumeau¹, R. Hahn¹, Z. L. Zhang² & P. H. Mayrhofer¹

Received: 7 July 2017

Accepted: 16 November 2017

Published online: 28 November 2017

Hard coatings used to protect engineering components from external loads and harsh environments should ideally be strong and tough. Here we study the fracture toughness, K_{IC} , of $Ti_{1-x}Al_xN$ upon annealing by employing micro-fracture experiments on freestanding films. We found that K_{IC} increases by about 11% when annealing the samples at 900 °C, because the decomposition of the supersaturated matrix leads to the formation of nanometer-sized domains, precipitation of hexagonal-structured B4 AlN (with their significantly larger specific volume), formation of stacking faults, and nano-twins. In contrast, for TiN, where no decomposition processes and formation of nanometer-sized domains can be initiated by an annealing treatment, the fracture toughness K_{IC} remains roughly constant when annealed above the film deposition temperature. As the increase in K_{IC} found for $Ti_{1-x}Al_xN$ upon annealing is within statistical errors, we carried out complementary cube corner nanoindentation experiments, which clearly show reduced (or even impeded) crack formation for annealed $Ti_{1-x}Al_xN$ as compared with their as-deposited counterpart. The ability of $Ti_{1-x}Al_xN$ to maintain and even increase the fracture toughness up to high temperatures in combination with the concomitant age hardening effects and excellent oxidation resistance contributes to the success of this type of coatings.

Hard coatings are applied to protect tool and component surfaces as well as entire devices in harsh environments and/or demanding application conditions. The coatings are usually ceramic materials, which are known for their beneficial properties such as high hardness and wear resistance, high melting temperatures, high-temperature strength, chemical inertness and oxidation resistance. However, these materials often possess a relatively low (fracture) toughness. A certain degree of toughness, however, is crucial for the reliability and safe operation of critical components. Various strategies have been applied to enhance the fracture toughness of bulk materials¹ and hard coatings^{2,3}.

Since the pioneer works in the nineteen eighties^{4,5}, $Ti_{1-x}Al_xN$ has evolved to one of the most widely used and industrial relevant hard coating systems⁶. Age hardening effects are (besides enhanced oxidation resistance⁷ and resistance against wear^{4,5} compared to TiN) considered to be the major basis for its industrial success. At temperatures typical for cutting tools operation, supersaturated face-centered cubic $Ti_{1-x}Al_xN$ isostructurally decomposes into nanometer-sized AlN-rich and TiN-rich domains. This is due to spinodal decomposition causing self-hardening effects^{8–11}. Nonetheless, the influence of its characteristic thermally activated decomposition and the resulting self-organized nanostructure on the fracture toughness is yet to be studied.

The present work revolves around the hypothesis that (besides the well-known self-hardening effects⁹) also the fracture toughness of $Ti_{1-x}Al_xN$ coatings increases at elevated temperatures. Potential fracture toughness enhancing mechanisms in the self-organized nanostructure of B1 AlN-rich and TiN-rich domains^{8–11} are based on: coherency strains, spatially fluctuating elastic properties, and stress-induced phase transformation toughening from cubic to hexagonal AlN phases under volume expansion at the tip of a propagating crack similar to Yttrium-stabilized zirconia bulk ceramics¹² or Zr-Al-N based nanoscale multilayers¹³. We will also see that the B4 AlN phase formation can play a key role for the fracture toughness evolution of $Ti_{1-x}Al_xN$. By using high-resolution transmission electron microscopy (HRTEM), we observed severely distorted B4 AlN with multiple stacking faults and indications of nano-twins. Twinning represents a mechanism capable of simultaneously enhancing strength and ductility in materials¹⁴.

¹Institute of Materials Science and Technology, TU Wien, A-1060, Vienna, Austria. ²Erich Schmid Institute of Materials Science, Austrian Academy of Sciences, A-8700, Leoben, Austria. Correspondence and requests for materials should be addressed to M.B. (email: matthias.bartosik@tuwien.ac.at)

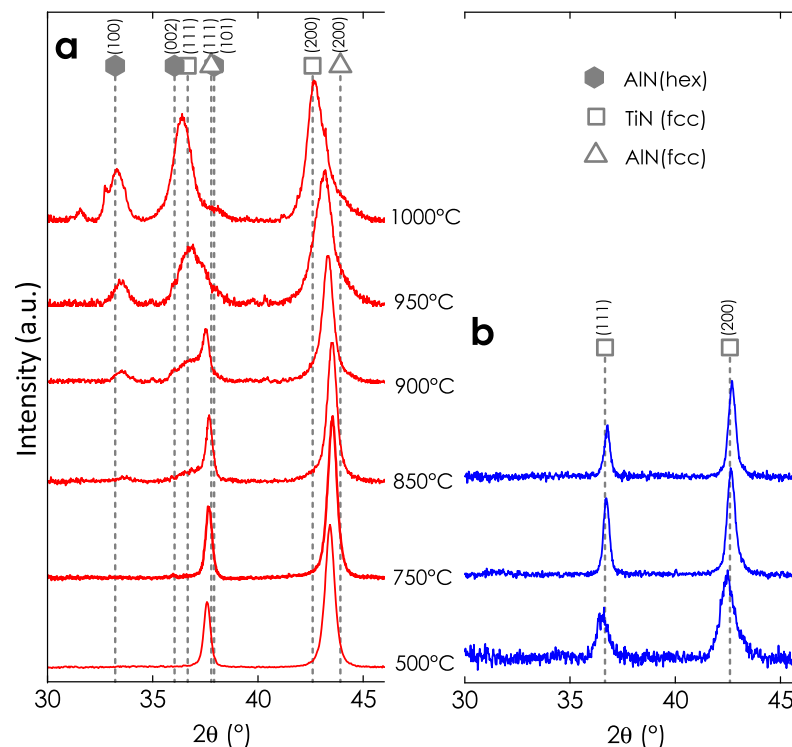


Figure 1. XRD patterns of as-deposited and vacuum annealed (a) $\text{Ti}_{0.40}\text{Al}_{0.60}\text{N}$ and (b) TiN films on Al_2O_3 ($1\bar{1}02$) substrates. (JCPDF files: 38–1420 TiN, 25–1495 fcc AlN, 25–1133 hex. AlN). The graphs show the thermally activated decomposition sequence of cubic TiAlN into iso-structural TiN-rich and cubic AlN-rich domains followed by the formation of wurtzite AlN. Annealing of TiN is characterized by recovery of built-in growth defects.

We carried out cantilever deflection (and cube corner nanoindentation experiments) to study the evolution of the fracture toughness of up to 1000 °C *ex-situ* vacuum annealed $\text{Ti}_{1-x}\text{Al}_x\text{N}$ free-standing films and correlated them with the film structural evolution and the mechanical properties, hardness (H) and Young's modulus (E), obtained from independent experiments. The mechanical properties were corroborated with HRTEM investigations to give atomic scale insights into the thermally decomposed $\text{Ti}_{1-x}\text{Al}_x\text{N}$ structure. TiN coatings are used as a benchmark, as no decomposition processes are active that would lead to the formation of new nm-sized domains.

Results

Structural evolution. Energy dispersive X-ray spectroscopy (EDXS) analysis rendered a chemical composition of $\text{Ti}_{0.40}\text{Al}_{0.60}\text{N}$. Due to the specific sputter condition of the $\text{Ti}_{0.5}\text{Al}_{0.5}$ compound target, the coatings prepared are slightly richer in Al than the target for the deposition parameters used¹⁵. The oxygen content within the coatings is below 1 at.%, as obtained by elastic recoil detection analysis of coatings prepared under comparable conditions¹⁵. Figure 1a shows the X-ray diffraction patterns of our $\text{Ti}_{0.40}\text{Al}_{0.60}\text{N}$ films grown onto Al_2O_3 ($1\bar{1}02$) substrates after vacuum annealing at different annealing temperatures, T_a , for 10 min. Up to 750 °C, $\text{Ti}_{0.40}\text{Al}_{0.60}\text{N}$ maintains its single phase face-centered cubic (rock-salt-type, B1) structure. The slight peak shift to higher 2θ angles and decrease in peak broadening indicate recovery of built-in structural point and line defects, which results in a lattice parameter decrease in the films. The peak shift to higher 2θ angles also suggests B1 AlN formation (its lattice parameter is smaller as compared to $\text{Ti}_{0.40}\text{Al}_{0.60}\text{N}$ ¹⁶, hence the diffraction peaks occur at higher 2θ angles). Between 850 and 1000 °C, an asymmetric peak broadening is observed, which indicates isostructural formation of cubic AlN- and TiN-rich domains. Especially, the right shoulder in vicinity of the cubic (200) peak – indicative for cubic AlN formation – is clearly visible and becomes more pronounced with increasing temperature. Hexagonal (wurtzite-type, B4 structured) AlN first emerges at 850 °C and its phase fraction increases with increasing temperature. The shift of the XRD reflections from the major cubic structured $\text{Ti}_{1-x}\text{Al}_x\text{N}$ matrix phase to lower 2θ angles is a result of decreasing Al content (hence, the XRD peaks shift towards the lower 2θ position of TiN). On the other hand, compressive stresses, e.g., induced by the B1 to B4 phase transformation of AlN¹⁷ under volume expansion of ~26%¹⁶ or by thermal stresses, contribute to the peak shift to lower 2θ angles (for the thermal expansion coefficients, α , holds as $\alpha_{\text{B1-(Ti,Al)N}} > \alpha_{\text{Al}_2\text{O}_3} > \alpha_{\text{B4-AlN}}$, see refs^{18–20}).

The structural evolution of single phase cubic structured TiN, Fig. 1b, is dominated by recovery of built-in structural point and line defects and results in smaller lattice parameters. Accordingly, the peaks are shifted to larger 2θ angles and become sharper with increasing temperature. Both, $\text{Ti}_{0.40}\text{Al}_{0.60}\text{N}$ and TiN crystallized in a

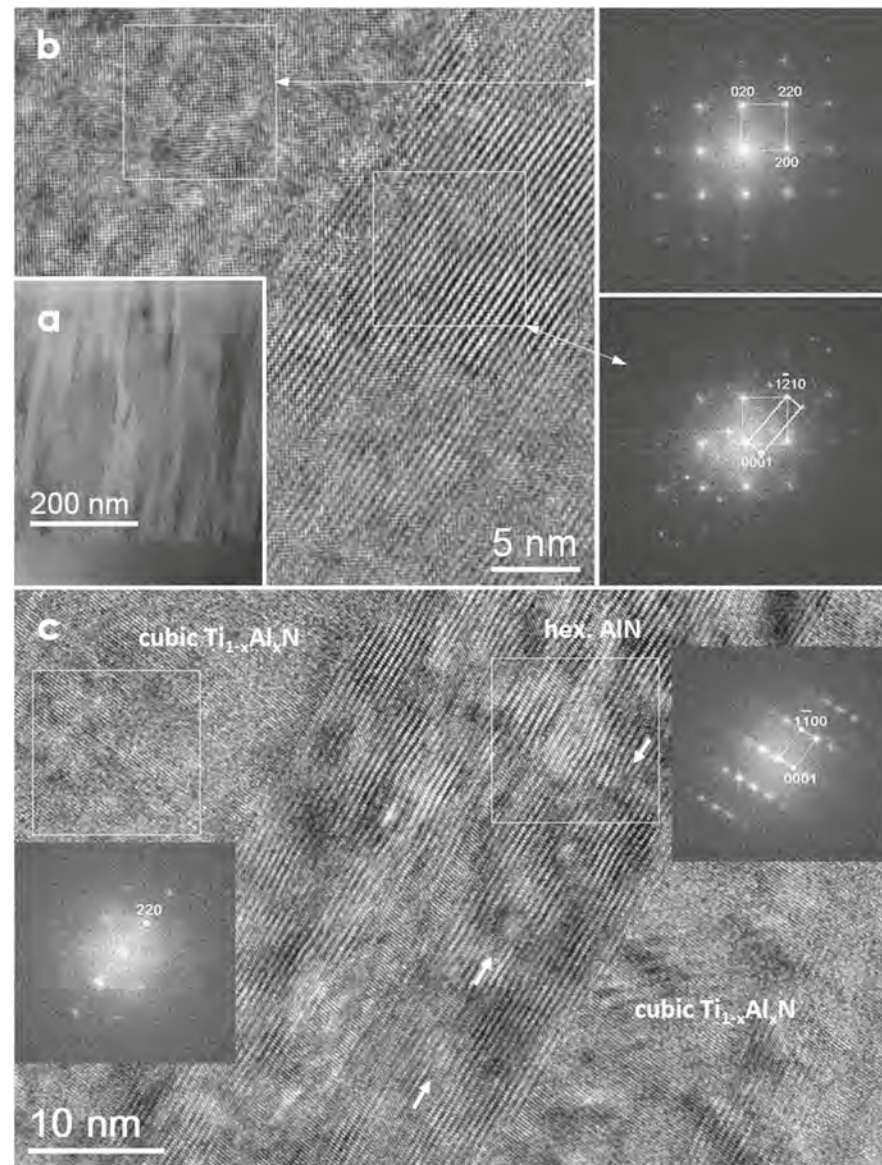


Figure 2. (a) Low magnification TEM image showing the columnar morphology of $\text{Ti}_{1-x}\text{Al}_x\text{N}$; (b) HRTEM image covering one cubic $\text{Ti}_{1-x}\text{Al}_x\text{N}$ grain along the $[001]$ zone axis and hexagonal AlN grains along the $[21\bar{1}0]$ direction, the corresponding FFTs are attached; (c) HRTEM image showing one hexagonal AlN grain that grows in between two cubic $\text{Ti}_{1-x}\text{Al}_x\text{N}$ grains, viewing direction of AlN is close to hexagonal $[11\bar{2}0]$. Multiple stacking faults and nano-twins in the hexagonal AlN phase are visible. One stacking fault is exemplarily marked with white arrows (pointing to the locations of partial dislocations). Note that all FFTs are obtained from the square regions.

polycrystalline structure. (For a thorough analysis of the crystallographic texture further investigations would be necessary, e.g., pole figure measurements based on X-ray diffraction).

TEM/HRTEM study. TEM studies were performed on the sample annealed at 900°C using cross-section samples. A low-magnified image presents an overview of the coating morphology (Fig. 2a), where columnar grains are clearly visible. At this annealing temperature, AlN based hexagonal phases emerge. An atomic resolution TEM image of one portion of grain interfaces are shown in Fig. 2b, the corresponding fast Fourier transforms (FFTs) are seen on the right-hand side. Analysis indicates that a cubic structured $\text{Ti}_{1-x}\text{Al}_x\text{N}$ grain is oriented along the $[001]$ direction while the adjacent hexagonal AlN grain is close to $[21\bar{1}0]$ direction, with an orientation relationship of $\text{Ti}_{1-x}\text{Al}_x\text{N}(2\bar{2}0)//\text{AlN}(0001)$. This implies that hexagonal AlN (0001) grows on $\text{Ti}_{1-x}\text{Al}_x\text{N}(2\bar{2}0)$ planes

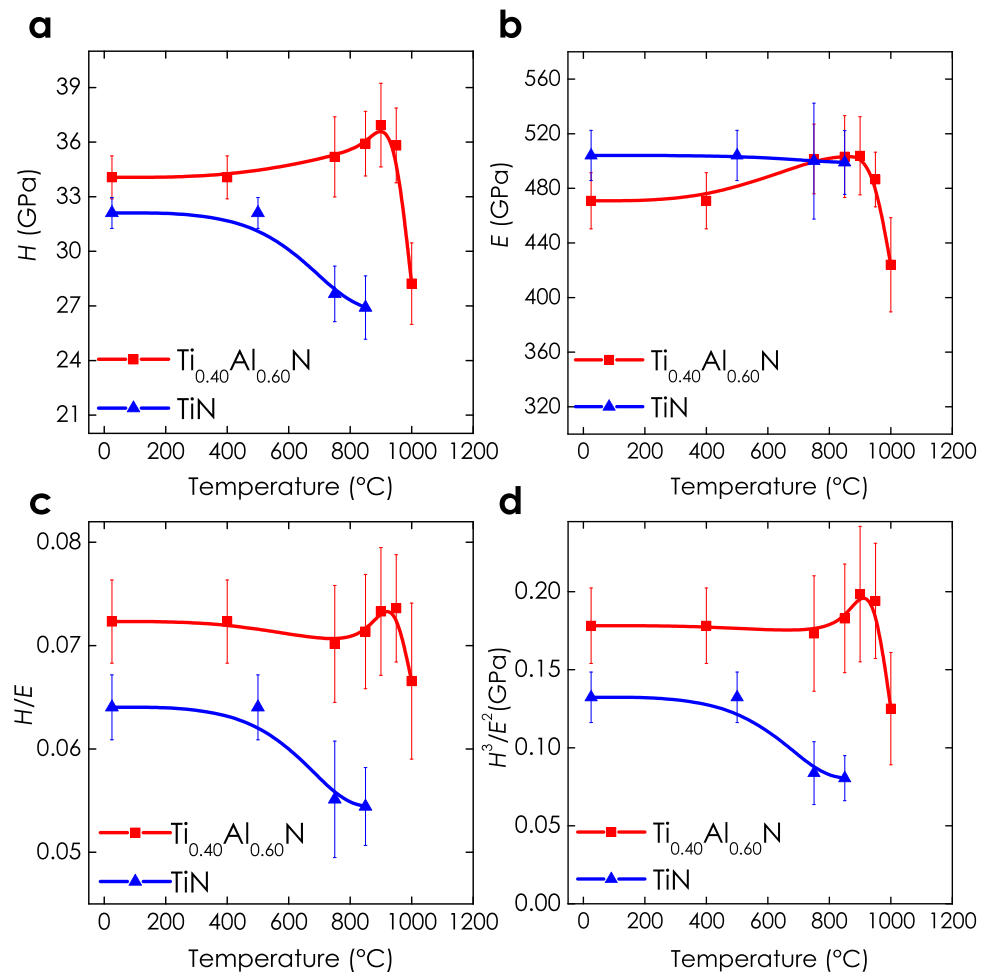


Figure 3. Hardness (H), indentation modulus (E), (H/E), and (H^2/E^2) ratios of $\text{Ti}_{0.40}\text{Al}_{0.60}\text{N}$ as a function of annealing temperature (annealing time = 10 min). Age-hardening effects and implications on the toughness criteria are clearly visible.

with a small misfit of $\delta = \frac{d_{220}^{\text{TiAlN}} - d_{1210}^{\text{AlN}}}{d_{220}^{\text{TiAlN}}} \approx 5.7\%$ along this direction. The corresponding FFTs clearly signify the plane relationship between these two phases. This has also been proved by tilting the grains to another orientation. Figure 2c shows one hexagonal AlN grain, grown in between two cubic $\text{Ti}_{1-x}\text{Al}_x\text{N}$ grains, viewed along the $[11\bar{2}0]$ direction while $\text{Ti}_{1-x}\text{Al}_x\text{N}$ is off $[001]$ zone axis, as illustrated in the corresponding FFTs (inserted). Here, only a series of planes appear. The orientation relation is $\text{Ti}_{1-x}\text{Al}_x\text{N} (220) // \text{AlN} (1\bar{1}00)$ for this case. It is further noted that the planes in hexagonal AlN are severely distorted or inclined which means that internal stress is strongly involved during the phase transformation. There are numerous defects present in the hexagonal AlN regions, for instance stacking faults and nano-twins marked exemplarily with white arrows in Fig. 2c. In some cases, the AlN phase seems to form in the $\text{Ti}_{1-x}\text{Al}_x\text{N}$ matrix, *i.e.* Fig. 2b, since the FFT from AlN contains $\text{Ti}_{1-x}\text{Al}_x\text{N}$ spots. However, hexagonal AlN frequently forms at the grain boundary as demonstrated in Fig. 2c, in which the hexagonal AlN and $\text{Ti}_{1-x}\text{Al}_x\text{N}$ phases are separated and formed in between two $\text{Ti}_{1-x}\text{Al}_x\text{N}$ grains. Consequently, the AlN phase transformation (from cubic to hexagonal) can take place in the matrix and also at the grain boundaries, in agreement with earlier studies²¹.

Nanoindentation. The mechanical properties as a function of annealing temperature are presented in Fig. 3 and are in line with previous studies reported in literature⁹. The indentation hardness (H), Fig. 3a, increases for $\text{Ti}_{0.40}\text{Al}_{0.60}\text{N}$ (red curves) by $\sim 9\%$ from 34 ± 1 GPa in the as-deposited state to 37 ± 2 GPa at 900°C , before it decreases again down to 28 ± 2 GPa at 1000°C . The Young's modulus (E), Fig. 3b, shows a similar trend. Contrarily, the hardness of TiN (blue curves) steadily decreases with increasing T_a , from 32 ± 1 GPa at room temperature to 27 ± 1 GPa at 850°C , (Fig. 3a), while the Young's modulus marginally decreases (Fig. 3b). The chosen deposition conditions used in the present study resulted in coatings with excellent mechanical properties

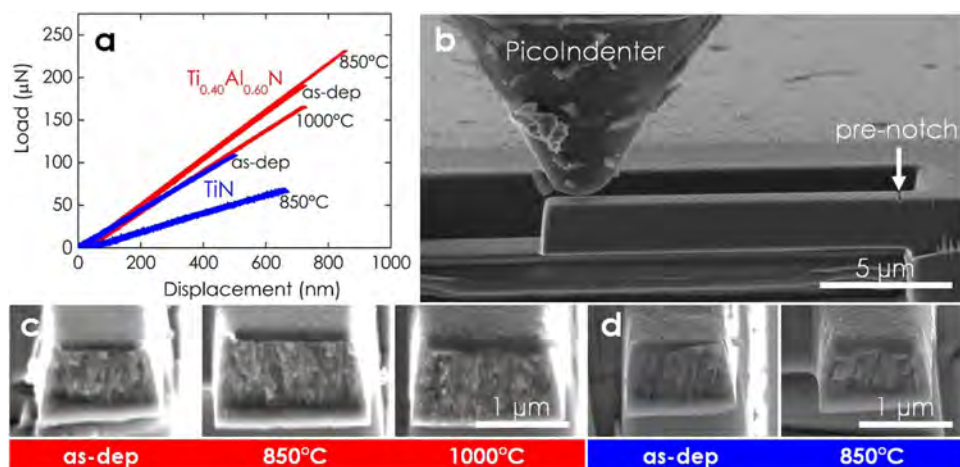


Figure 4. (a) Representative force–deflection curve of free-standing (*ex-situ*) annealed TiAlN cantilevers recorded during testing inside the scanning electron microscope. (b) The small dimension of the coating requires dedicated miniaturized micromechanical testing techniques. The image shows a scanning electron microscope image of the PicoIndenter tip approaching the pre-notched free-standing film cantilever. The cantilever is loaded until fracture. From simultaneous recorded load–deflection curves, the actual cantilever and pre-notch dimensions, and by applying fracture mechanics theory, the fracture toughness can be determined. (c) and (d) show the post-mortem fracture cross-sections (45° inclined view) of as-deposited and annealed TiAlN and TiN samples, respectively.

in the as-deposited state. In general, age hardening effects are more pronounced for softer coatings, *e.g.*, a relative increase of ~25% was observed for Ti_{1-x}Al_xN with an as-deposited hardness of ‘only’ ~26 GPa²¹.

The elastic strain to failure^{22–26}, (H/E), which is often used to qualitatively rate materials for their failure resistance, suggests superior properties of Ti_{0.40}Al_{0.60}N in comparison with TiN, Fig. 3c. While (H/E) values for Ti_{0.40}Al_{0.60}N are maintained up to high temperatures and even increase, the (H/E) ratio of TiN is below that of Ti_{0.40}Al_{0.60}N in the as-deposited state and shows a steady decrease upon annealing above the deposition temperature. A similar trend can be observed for the plastic deformation resistance factor^{22,25,26}, (H^3/E^2), shown in Fig. 3d, indicating superior wear resistance of Ti_{0.40}Al_{0.60}N in comparison with TiN.

Micromechanical Testing. Representative recorded force–deflection curves, given in Fig. 4a, show that Ti_{0.40}Al_{0.60}N and TiN deform in a linear manner, elastically during loading by a PicoIndenter until failure. No indications of plastic deformation are seen. (Please note that the actual cantilever dimensions, lever arms, and pre-notch depths differ from sample to sample. Hence, Fig. 4a, does not allow direct ranking of the samples with respect to their stiffness and fracture toughness). Figure 4b shows a typical free-standing cantilever. The substrate material had been removed by focused ion beam milling to avoid the influence of residual stresses and substrate interference. Scanning electron micrographs of the post-mortem fracture cross-sections, Fig. 4c,d, do not show discernible changes of the film morphology upon annealing. However, the structure of TiN (Fig. 4d) appears more columnar-grained in comparison with Ti_{0.40}Al_{0.60}N (Fig. 4c). The K_{IC} values, as calculated from the maximum load at failure, the actual pre-notch depth, and cantilever dimensions using a linear elastic fracture mechanics approach²⁷, are presented in Fig. 5. The data suggest an increase in K_{IC} from 2.7 ± 0.3 MPa·√m in the as-deposited state to 3.0 ± 0.01 MPa·√m at 900 °C followed by a decrease to 2.8 ± 0.4 MPa·√m at 1000 °C (red curve). The relative increase of ~11% in fracture toughness of Ti_{0.40}Al_{0.60}N is similar to the relative increase in hardness of ~9%. Please note, however, that strictly speaking the increase in fracture toughness is within statistical error. Interestingly, the pronounced decrease in hardness at 1000 °C due to wurtzite AlN formation is not observed for K_{IC} , which—in agreement with the H/E criterion—only slightly decreases. Lower K_{IC} values of ~1.9 MPa·√m are found for as-deposited and annealed TiN (blue curve).

To qualitatively prove that K_{IC} increases upon annealing, we carried out independent cube corner nanoindentation experiments on coated Al₂O₃ (1 $\bar{1}02$) substrates. Scanning electron microscopy images of the indents show aggravated (or even impeded) crack formation for annealed Ti_{1-x}Al_xN samples as compared to the as-deposited counterpart, see Fig. 6. Please note that in the cube corner experiment, residual stresses (*e.g.*, massive compressive residual stresses forming due to the cubic to wurtzite AlN phase transformation under volumes expansion) and the underlying substrate can influence the formation of cracks.

Discussion

The structural evolution of supersaturated cubic Ti_{1-x}Al_xN upon annealing has been experimentally proven in the literature by atom probe tomography^{11,28}, small angle X-ray scattering²⁹, transmission electron microscopy³⁰, and described by phase field simulations³⁰: During the early stage, very few nanometer-sized B1 AlN- and TiN-rich domains form in a coherent manner (that is, the crystallographic orientation of the domains correspond to that

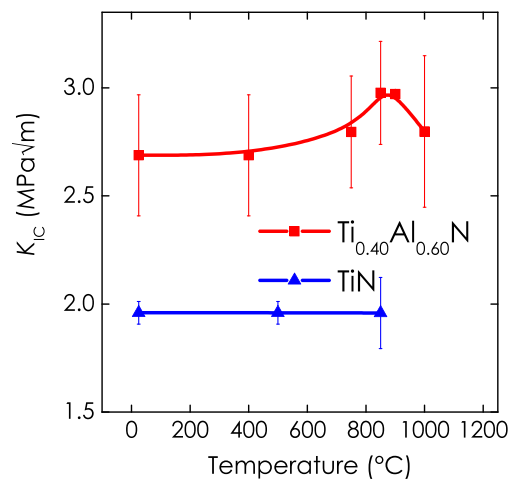


Figure 5. An increase in fracture toughness, K_{IC} , is observed after 10 min vacuum annealing of the coatings at 850 and 900 °C (red curve). Such temperatures are typically reached in the application due to the friction between the coated cutting tool and the workpiece. In the case of TiN, where (spinodal) decomposition is absent, K_{IC} remains roughly constant when heated above the film deposition temperature.

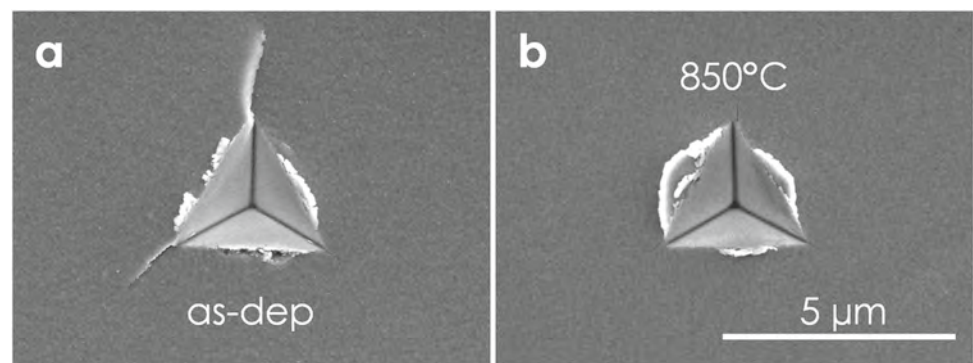


Figure 6. Cube corner nanoindentation experiments reveal aggravated (or even impeded) crack formation for annealed (b) as compared with as-deposited (a) $Ti_{1-x}Al_xN$ coatings on sapphire substrates.

of the $Ti_{1-x}Al_xN$ parent grain). With progressive annealing time, the domains gain in size and the compositional variations become more pronounced, so that the modulation amplitudes (Ti- and Al-rich) become larger. If the annealing is continued for too long or performed at higher temperatures, coherency strains are relieved by misfit dislocations. Eventually, cubic structured AlN-rich domains transform into the softer but thermodynamically stable (first (semi) coherent then incoherent) hexagonal AlN. The cubic to hexagonal AlN phase transformation is associated with a large volume expansion of ~26%¹⁶.

Thermally-induced hardening effects in the TiAlN system have been attributed to coherency strains⁹. *Coherency strains* hinder the movement of dislocations³¹, as it is more difficult for dislocations to pass through a strained than a homogenous lattice. In addition, the coherent domains differ in their elastic properties due to the strong composition dependent elastic anisotropy of $Ti_{1-x}Al_xN$ ³², which also hinders the dislocation motion and contributes to the hardness enhancement³².

The structural evolution observed in the present study is in line with the literature reports mentioned above. Additionally, we have evidenced severely distorted or inclined lattice planes and numerous defects (including stacking faults) in the hexagonal AlN phase by HRTEM investigations (Fig. 2). This could explain why the measured hardness at 900 °C is relatively high despite the presence of the “soft” hexagonal AlN phase, which is usually reported to deteriorate the hardness.

We have been able to show that besides age hardening effects, the fracture toughness increases upon annealing. Both properties show a similar relative increase of around 10% as compared to the as-deposited state and peak at the same temperature of 900 °C. This suggests that similar microstructural characteristics are responsible for the enhancement of the mechanical properties. We could demonstrate in an earlier study³ that a coherent nanostructure composed of alternating materials has the potential to enhance the fracture toughness for a certain

bilayer period of a few nanometers. In the superlattice films, also *coherency strains*^{33,34} and *variations in the elastic properties* are present. It should be mentioned, however, that in contrast to the hardness, the fracture toughness is not primarily governed by the hindrance of dislocation motion: the load-displacement data collected during the cantilever deflection experiments (Fig. 4a) suggest a linear elastic behavior until failure with no indications of plastic deformation.

In agreement with literature reports²¹, we found that cubic AlN forms preferentially at high diffusivity paths such as grain boundaries. If grain boundaries represent the weakest link where cracks preferentially propagate³⁵, *grain boundary reinforcement*³⁶ has the potential to effectively hinder the crack propagation.

Another important mechanism for increased fracture toughness is *phase transformation toughening*, which is omnipresent in partially stabilized zirconia bulk ceramics¹², for example. For $\text{Ti}_{1-x}\text{Al}_x\text{N}$ coatings, the spinodally formed cubic structured AlN-rich domains represent the phase with the ability of a martensitic-like phase transformation from the metastable cubic structure to the stable wurtzite-type (w) variant. The associated volume expansion of ~26%¹⁶ slows down or closes advancing cracks, leading to a significant K_{IC} increase. Therefore, the evolution of K_{IC} with T_a of our $\text{Ti}_{0.40}\text{Al}_{0.60}\text{N}$ coatings is not proportional to that of H with T_a , especially at temperatures above 850 °C. The hardness significantly decreases for an increase of T_a from 950 to 1000 °C, as also the w-AlN formation significantly increases (please compare Figs. 1 and 3a), but at the same time, the fracture toughness K_{IC} only slightly decreases. The K_{IC} value of $2.8 \pm 0.4 \text{ MPa}\cdot\sqrt{\text{m}}$ after annealing at 1000 °C, is still above that of the as deposited state (with $K_{IC} = 2.7 \pm 0.3 \text{ MPa}\cdot\sqrt{\text{m}}$), whereas the hardness with $H = 28 \pm 2 \text{ GPa}$ after annealing at 1000 °C is significantly below the as deposited value of $34 \pm 1 \text{ GPa}$. Hence, effective other mechanisms are present in this type of material, especially when decomposition of the supersaturated matrix phase occurs and w-AlN based phases are able to form.

Note that in the chosen free-standing cantilever setup macro-stresses are relieved and thus do not contribute to the observed toughness enhancement. However, due to the extensive difference in the molar volume between cubic and wurtzite AlN, the thermally-induced formation of hexagonal AlN results in pronounced compressive stresses^{17,37} in the application where the coatings are firmly attached to a substrate/engineering component. Compressive stresses result in *apparent toughening* of $\text{Ti}_{1-x}\text{Al}_x\text{N}$, as the coating can withstand higher tensile stresses before cracks are initiated (the compressive stresses have to be overcome first before crack formation). The effect of compressive stresses on the fracture toughness is supposed to be much more pronounced than its influence on the hardness. This is why, in real application, the K_{IC} increase upon annealing is expected to be significantly larger than the K_{IC} enhancement found from free-standing micro-cantilever bending tests. This is reflected in the aggravated crack formation observed in the cube corner experiments, see Fig. 6.

As the 'inherent' fracture toughness enhancing effects are strongly connected with the spinodal decomposition, we anticipate that alloying³⁸⁻⁴¹ and other concepts to modify the spinodal decomposition characteristics (formation of coherent cubic AlN domains at lower temperatures but delayed formation of the thermodynamically stable phase wurtzite AlN, different shape and size of cubic AlN domains) are applicable to optimize the self-toughening behavior. In general, alloying has the potential to enhance the inherent toughness by modifying the electronic structure and bonding characteristics^{42,43}.

The peak in hardness and fracture toughness at 900 °C corresponds to spinodally decomposed TiAlN with fractions of hexagonal AlN as indicated by XRD (Fig. 1) and TEM (Fig. 2). The severely distorted hexagonal AlN with multiple stacking faults suggests that also nano-twinning might become a relevant mechanism. The presence of twins impedes dislocation motion and induces strengthening, but multiple twinning systems can also enhance ductility by acting as a carrier of plasticity¹⁴.

Based on our results we propose that the additional functionality of $\text{Ti}_{1-x}\text{Al}_x\text{N}$, *i.e.* the self-toughening ability at temperatures typical for many various applications, contributes to the outstanding performance of $\text{Ti}_{1-x}\text{Al}_x\text{N}$ coatings in *e.g.*, dry or high speed cutting.

Methods

Sample preparation. $\text{Ti}_{0.40}\text{Al}_{0.60}\text{N}$ films were deposited in a lab-scale magnetron sputter system (a modified Leybold Heraeus Z400) equipped with a 3 inch powder-metallurgical processed $\text{Ti}_{0.50}\text{Al}_{0.50}$ compound target. Polished single crystalline Al_2O_3 (1 $\bar{1}02$) platelets ($10 \times 10 \times 0.53 \text{ mm}^3$) were chosen as substrate materials due to their high thermal stability, inertness and to avoid interdiffusion between film and substrate materials upon annealing up to 1000 °C. Before the deposition, the substrates (ultrasonically pre-cleaned in acetone and ethanol) were heated within the deposition chamber to 500 °C, thermally cleaned for 20 min and sputter cleaned with Ar ions for 10 min. The deposition was performed at the same temperature in a mixed N_2/Ar atmosphere with a gas flow ratio of 4 sccm/6 sccm and a constant total pressure of 0.35 Pa by setting the target current to 1 A (DC) while applying a DC bias voltage of -50 V to the substrates. The films were grown to a thickness of about 1.8 μm with an average deposition rate of about 75 nm/min. The base pressure was below $5 \cdot 10^{-6}$ mbar. TiN coatings of about 1.2 μm were synthesized by powering a 3 inch Ti cathode with 500 W within an N_2/Ar gas mixture (flow ratio of 3 sccm/7 sccm, constant total pressure of 0.4 Pa) and applying a bias voltage of -60 V to the substrates. The deposition rate was about 13 nm/min.

Energy dispersive X-ray spectroscopy (EDXS) measurements of the films were performed with an EDAX Sapphire EDS detector inside a Philips XL-30 scanning electron microscope. Thin film standards characterized by elastic recoil detection analyses were used to calibrate the EDX measurements.

The films on Al_2O_3 were annealed in a vacuum furnace (Centorr LF22-2000, base pressure $< 3 \cdot 10^{-3}$ Pa) at different maximum temperatures (T_a) between 750 and 1000 °C using a heating rate of $20 \text{ }^\circ\text{C min}^{-1}$ and passive cooling. At T_a , the temperature was kept constant for 10 min.

Structural investigations of coated Al_2O_3 substrates were performed by X-ray diffraction in symmetric Bragg-Brentano geometry using a PANalytical X'Pert Pro MPD diffractometer (Cu-K_α radiation).

Cross-sectional TEM specimens were prepared using a standard TEM sample preparation approach including cutting, gluing, grinding and dimpling. Finally, Ar ion milling was carried out. A JEOL 2100 F field emission microscope (200 kV) equipped with an image-side C_s -corrector with a resolution of 1.2 Å at 200 kV was used. The aberration coefficients were set to be sufficiently small, *i.e.* $C_s \sim 10.0 \mu\text{m}$. The HRTEM images were taken under a slight over-focus. The HRTEM images were carefully analysed using Digital Micrograph software.

Micromechanical testing. The mechanical properties, hardness and indentation modulus, were measured using a UMIS nanoindenter equipped with a Berkovich tip. At least 30 indents per sample, with increasing loads from 3 to 45 mN were performed. The recorded data were evaluated using the Oliver and Pharr method⁴⁴. To minimize substrate interference, only indents with indentation depths below 10% of the coating thickness were taken into account. The cube corner experiments were carried with the UMIS nanoindenter using a peak indentation load of 150 mN. The high load needed to create cracks resulted in indentation depths of about 1.3 μm in the cube corner experiment.

The fracture toughness was determined from micromechanical cantilever bending tests of free-standing film material. As-deposited and annealed coated Al_2O_3 samples were broken and their cross-sections carefully polished. The substrate material was removed by Focused Ion Beam (FIB) milling perpendicular to the film growth direction using a FEI Quanta 200 3D DBFIB work station. Then the sample holder was tilted 90° and cantilevers were milled perpendicular to the film surface. The cantilever dimensions of $\sim t \times t \times 6t \mu\text{m}^3$, with t denoting the film thickness, were chosen based on guidelines reported in Brinckmann *et al.*⁴⁵ For the final milling step, the ion beam current was reduced to 500 pA, the initial notch was milled with 50 pA. To circumvent the problem of a finite root radii on the fracture toughness measurements, bridged notches according to Matoy *et al.*²⁷ were used (the notch length was chosen to be $\sim 0.75t$).

The micromechanical experiments were performed inside a scanning electron microscope (FEI Quanta 200 FEGSEM) using a PicoIndenter (Hysitron PI85) equipped with a spherical diamond tip with a nominal tip radius of 1 μm . The micro-cantilever beams were loaded displacement-controlled with 5 nm/s with the loading axis perpendicular to the film surface. Per annealing temperature at least 3 tests were conducted. The fracture toughness, K_{IC} , was determined using linear elastic fracture mechanics according to the formula given in ref.²⁷:

$$K_{IC} = \frac{F_{max}L}{BW^{3/2}}f\left(\frac{a}{w}\right) \quad (1)$$

with $f\left(\frac{a}{w}\right) = 1.46 + 24.36 \cdot \left(\frac{a}{w}\right) - 47.21 \cdot \left(\frac{a}{w}\right)^2 + 75.18 \cdot \left(\frac{a}{w}\right)^3$. In the equation, F_{max} denotes the maximum load applied, L the lever arm (distance between the notch and the position of loading), B the width of the cantilever, W the thickness of the cantilever, and a the initial crack length (measured from the post mortem fracture cross-sections).

References

- Ritchie, R. O. The conflicts between strength and toughness. *Nat. Mater.* **10**, 817 (2011).
- Zhang, S., Sun, D., Fu, Y. & Du, H. Toughening of hard nanostructural thin films: a critical review. *Surf. Coat. Tech.* **198**, 2 (2005).
- Hahn, R. *et al.* Superlattice effect for enhanced fracture toughness of hard coatings. *Scripta Mater.* **124**, 67 (2016).
- Knotek, O., Böhmer, M. & Leyendecker, T. On structure and properties of sputtered Ti and Al based hard compound films. *J. Vac. Sci. Technol.* **A4**, 2695 (1986).
- Münz, W.-D. Titanium aluminum nitride films: A new alternative to TiN coatings. *J. Vac. Sci. Technol.* **A4**, 2717 (1986).
- PalDey, S. & Deevi, S. C. Single layer and multilayer wear resistant coatings of (Ti,Al)N: a review. *Mater. Sci. Eng.* **A342**, 58 (2003).
- McIntyre, D., Greene, J. E., Håkansson, G., Sundgren, J. -E. & Münz, W. -D. Oxidation of metastable single-phase polycrystalline Ti_{0.5}Al_{0.5}N films: Kinetics and mechanisms. *J. Appl. Phys.* **67**, 1542 (1990).
- Hörling, A., Hultman, L., Odén, M., Sjöln, J. & Karlsson, L. Thermal stability of arc evaporated high aluminum-content Ti_{1-x}Al_xN thin films. *J. Vac. Sci. Technol.* **A20**, 1815 (2002).
- Mayrhofer, P. H. *et al.* Self-organized nanostructures in the Ti–Al–N system. *Appl. Phys. Lett.* **83**, 2049 (2003).
- Alling, B. *et al.* Mixing and decomposition thermodynamics of c-Ti_{1-x}Al_xN from first-principles calculations. *Phys. Rev. B* **75**, 045123 (2007).
- Rachbauer, R., Stergar, E., Massl, S., Moser, M. & Mayrhofer, P. H. Three-dimensional atom probe investigations of Ti–Al–N thin films. *Scripta Mater.* **61**, 725 (2009).
- Kelly, P. M. & Rose, L. R. F. The martensitic transformation in ceramics – its role in transformation toughening. *Prog. Mater. Sci.* **47**, 463 (2002).
- Yalamanchili, K. *et al.* Tuning hardness and fracture resistance of ZrN/Zr_{0.63}Al_{0.37}N nanoscale multilayers by stress-induced transformation toughening. *Acta Mater.* **89**, 22 (2015).
- Zhang, Z. *et al.* Dislocation mechanisms and 3D twin architectures generate exceptional strength-ductility-toughness combination in CrCoNi medium-entropy alloy. *Nat. Commun.* **8**, 14390 (2017).
- Riedl, H. *et al.* Influence of oxygen impurities on growth morphology, structure and mechanical properties of Ti–Al–N thin films. *Thin Solid Films* **603**, 39 (2016).
- Mayrhofer, P. H., Music, D. & Schneider, J. M. Influence of the Al distribution on the structure, elastic properties, and phase stability of supersaturated Ti_{1-x}Al_xN. *J. Appl. Phys.* **100**, 094906 (2006).
- Bartosik, M. *et al.* Lateral gradients of phases, residual stress and hardness in a laser heated Ti_{0.52}Al_{0.48}N coating on hard metal. *Surf. Coat. Tech.* **206**, 4502 (2012).
- Bartosik, M. *et al.* Thermal expansion of rock-salt cubic AlN. *Appl. Phys. Lett.* **107**, 071602 (2016).
- Freund, L. B., Suresh, S. *Thin Film Materials: Stress, Defect Formation, and Surface Evolution*. Cambridge University Press, Cambridge, United Kingdom (2003).
- Bartosik, M. *et al.* Thermal expansion of Ti–Al–N and Cr–Al–N coatings. *Scripta Mater.* **127**, 182 (2017).
- Rachbauer, R. *et al.* Decomposition pathways in age hardening of Ti–Al–N films. *J. Appl. Phys.* **110**, 023515 (2011).
- Musil, J. *Advanced Hard Coatings with Enhanced Toughness and Resistance to Cracking*, in: Zhang, S. (Ed.), *Thin Films and Coatings: Toughening and Toughness Characterization*, CRC Press (Taylor & Francis Group), Boca Raton, 377–464.
- Leyland, A. & Matthews, A. On the significance of the H/E ratio in wear control: a nanocomposite coating approach to optimised tribological behaviour. *Wear* **246**, 1 (2000).

24. Leyland, A. & Matthews, A. Design criteria for wear-resistant nanostructured and glassy-metal coatings. *Surf. Coat. Tech.* **177**, 317 (2004).
25. Musil, J. & Jirout, M. Toughness of hard nanostructured ceramic thin films. *Surf. Coat. Tech.* **201**, 5148 (2007).
26. Matthews, A. & Leyland, A. Materials Related Aspects of Nanostructured Tribological Coatings, SVC Bulletin, Spring 40 (2009).
27. Matoy, K. *et al.* A comparative micro-cantilever study of the mechanical behavior of silicon based passivation films. *Thin Solid Films* **518**, 247 (2009).
28. Johnson, L. J. S., Thuvander, M., Stiller, K., Odén, M. & Hultman, L. Spinodal decomposition of Ti_{0.33}Al_{0.67}N thin films studied by atom probe tomography. *Thin Solid Films* **520**, 4362 (2012).
29. Odén, M. *et al.* *In situ* small-angle x-ray scattering study of nanostructure evolution during decomposition of arc evaporated TiAlN coatings. *Appl. Phys. Lett.* **94**, 053114 (2009).
30. Knutsson, A. *et al.* Microstructure evolution during the isostructural decomposition of TiAlN—A combined *in-situ* small angle x-ray scattering and phase field study. *J. Appl. Phys.* **113**, 213518 (2013).
31. Cahn, J. W. Hardening by spinodal decomposition. *Acta Metall.* **11**, 1275 (1963).
32. Tasnádi, F. *et al.* Significant elastic anisotropy in Ti_{1-x}Al_xN alloys. *Appl. Phys. Lett.* **97**, 231902 (2010).
33. Zhang, Z. *et al.* Superlattice-induced oscillations of interplanar distances and strain effects in the CrN/AlN system. *Phys. Rev. B* **95**, 155305 (2017).
34. Gu, X., Zhang, Z., Bartosik, M., Mayrhofer, P. H. & Duan, H. P. Dislocation densities and alternating strain fields in CrN/AlN nanolayers. *Thin Solid Films* **638**, 189 (2017).
35. Watanabe, T. Grain boundary design for the control of intergranular fracture. *Mater. Sci. Forum* **46**, 25 (1989).
36. Li, Z. *et al.* Designing superhard, self-toughening CrAlN coatings through grain boundary engineering. *Acta Mater.* **60**, 5735 (2012).
37. Rogström, L. *et al.* Strain evolution during spinodal decomposition of TiAlN thin films. *Thin Solid Films* **520**, 5542 (2012).
38. Mayrhofer, P. H., Rachbauer, R., Holec, D., Rovere, F. & Schneider, J. M. Protective Transition Metal Nitride Coatings, in: S Hashmi (Ed.), *Comprehensive Materials Processing*, Elsevier, 2014, 355–388.
39. Chen, L., Holec, D., Du, Y. & Mayrhofer, P. H. Influence of Zr on structure, mechanical and thermal properties of Ti–Al–N. *Thin Solid Films* **519**, 5503 (2011).
40. Rachbauer, R., Holec, D. & Mayrhofer, P. H. Increased thermal stability of Ti–Al–N thin films by Ta alloying. *Surf. Coat. Tech.* **211**, 98 (2012).
41. Rachbauer, R., Blutmager, A., Holec, D. & Mayrhofer, P. H. Effect of Hf on structure and age hardening of Ti–Al–N thin films. *Surf. Coat. Tech.* **206**, 2667 (2012).
42. Sangiovanni, D. G., Chirita, V. & Hultman, L. Toughness enhancement in TiAlN-based quaternary alloys. *Thin Solid Films* **520**, 4080 (2012).
43. Sangiovanni, D. G., Hultman, L., Chirita, V., Petrov, I. & Greene, J. E. Effects of phase stability, lattice ordering, and electron density on plastic deformation in cubic TiWN pseudobinary transition-metal nitride alloys. *Acta Mater.* **103**, 823 (2016).
44. Oliver, W. C. & Pharr, G. M. An improved technique for determining hardness and elastic modulus using load and displacement sensing indentation experiments. *J. Mater. Res.* **7**, 1564 (1992).
45. Brinckmann, S., Kirchlechner, C. & Dehm, G. Stress intensity factor dependence on anisotropy and geometry during micro-fracture experiments. *Scripta Mater.* **127**, 76 (2017).

Acknowledgements

The financial support by the START Program (Y371) of the Austrian Science Fund (FWF) is highly acknowledged. The micromechanical experiments and XRD investigations were carried out at the facilities USTEM and XRC of TU Wien, Austria. We thank the Institute for Mechanics of Materials and Structures (TU Wien) for providing the PicoIndenter PI85.

Author Contributions

M.B. has designed the research, contributed to all experiments, and prepared the manuscript. C.R. primarily carried out the film synthesis & characterization, and FIB cantilever preparation. R.H. assisted in the micromechanical experiments. Z.L.Z. performed the HRTEM investigations and wrote the TEM part. P.H.M. was involved in all discussions and contributed to the text formulations.

Additional Information

Competing Interests: The authors declare that they have no competing interests.

Publisher's note: Springer Nature remains neutral with regard to jurisdictional claims in published maps and institutional affiliations.



Open Access This article is licensed under a Creative Commons Attribution 4.0 International License, which permits use, sharing, adaptation, distribution and reproduction in any medium or format, as long as you give appropriate credit to the original author(s) and the source, provide a link to the Creative Commons license, and indicate if changes were made. The images or other third party material in this article are included in the article's Creative Commons license, unless indicated otherwise in a credit line to the material. If material is not included in the article's Creative Commons license and your intended use is not permitted by statutory regulation or exceeds the permitted use, you will need to obtain permission directly from the copyright holder. To view a copy of this license, visit <http://creativecommons.org/licenses/by/4.0/>.

© The Author(s) 2017

Publication VII



Fracture toughness of Ti-Si-N thin films

M. Bartosik, R. Hahn, Z. L. Zhang, I. Ivanov, M. Arndt, P. Polcik, and P. H. Mayrhofer

Publication VIII



Influence of Tantalum on phase stability and mechanical properties of WB_2

Ch. Fuger, V. Moraes, R. Hahn, H. Bolvardi, P. Polcik, H. Riedl, and P. H. Mayrhofer

Publication IX



Deformation and Cracking Mechanism in CrN/TiN Multilayer Coatings

A. Azizpour, R. Hahn, F. F. Klimashin, T. Wójcik, E. Poursaeidi, and P. H. Mayrhofer

Concluding remarks

The assessment of inherent fracture toughness values is – despite a permanent development of new methods and growing interest by academia and industry – still a relatively unexplored field of materials science. Here the small length scale, the experimental accessibility to quantify the fracture toughness, and the time factor during FIB-preparation of microcantilever are the main challenges impeding a faster development in this area. The fracture properties of a material system are however of great interest in innovative industrial applications such as protective coatings for turbine blades in jet engines, gas turbine compressors, and steam turbine blades. The consequences of failure in these components may endanger human life or – in case of cutting tools – lead to economic disadvantages, therefore prior to application a sufficient damage tolerance has to be ensured.

To advance the field of hard coatings and widen their scope of applications, the main objective of this thesis was to reflect available hardness-enhancing mechanisms as well as assumed toughening mechanisms and to experimentally confirm their effectiveness. Within the main research conducted in this thesis this was realized as:

- Toughening by nanolayered structures, *i.e.* superlattices (publications I and II)
- Enhancing the elastic strain to failure by alloying high entropy nitride coatings with silicon (publication III)
- Toughening by increasing the ductility of transition metal nitrides (publication V)

Furthermore, a new material system was described by combing *ab initio* calculations and experimental research (publication IV).

In addition, a minor toughening effect was found for the Ti-Al-N system, however – when applied on a substrate – a significant enhancement of the apparent fracture toughness was qualitatively determined as a consequence of residual stresses (publication VI). In publication

VII an improvement in K_{IC} of more than 50% is reported by depositing nanostructured coatings. Finally, in publication VIII the influence of ductility on K_{IC} was validated and publication IX demonstrates a crack-deflecting characteristic of superlattice coatings.

Based on these results, we can conclude that a clear promotion of the field was achieved within the main published research as well as further conducted research.

Resume

Rainer Hahn, MSc.

Institute of Materials Science and Technology, Technische Universität Wien,
E-Mail: rainer.hahn@tuwien.ac.at, Phone: +43 1 58801 308104



Personal Data

Date and Place of Birth: [REDACTED]
Address: [REDACTED]
Citizenship: [REDACTED]
Phone: [REDACTED]

Education

- Since July 2016: PhD-Student in the Institute of Materials Science and Technology, Technische Universität Wien, Getreidemarkt 9/E308, 1060 Vienna, Austria
Thesis: "Fracture toughness enhancement of hard coatings"
Advisor: Prof. Paul Heinz Mayrhofer
- June 2016 Master of Science ("Diplom-Ingenieur") in Materials Science, Montanuniversität Leoben, Franz-Josef-Straße 18, 8700 Leoben, Austria
Thesis: "Superlattice Effect for Enhanced Fracture Toughness of Hard Coatings"
Advisor: Prof. Paul Heinz Mayrhofer

Relevant Work Experience

- Since July 2016: Project Assistant at the Institute of Materials Science and Technology, Technische Universität Wien, Austria
Christian Doppler Laboratory for application-oriented coating development
- January 2013 – June 2016: Student Assistant at the Institute of Materials Science and Technology, Technische Universität Wien, Austria
TEM sample preparation including FIB lift-out, X-ray diffraction, and Nanoindentation
- July - August 2013 & April 2014: Internship at MEE GmbH, Germany
Characterization of build-up welded and plasma nitrided plasticizing screws, and development of a manufacturing method for bimetal cylinders
- May 2012 – December 2012: Student Assistant at the Department of Physical Metallurgy and Materials Testing, Montanuniversität Leoben, Austria
TEM sample preparation, Annealing Treatments of thin films
- July 2011: Internship at OMV Group, Exploration and Production – Corrosion Laboratory, Austria
Corrosion experiments on steels for drill pipes and tubing materials